Ph.D. Thesis

OPTICAL FREQUENCY COMBS FROM MICRO RING RESONATORS

UNIVERSITY OF COPENHAGEN

This thesis has been submitted to the PhD school of the Faculty of Science, University of Copenhagen

by

Asbjørn Arvad Jørgensen

OPTICAL FREQUENCY COMBS FROM MICRO RING RESONATORS

Author	Asbjørn Arvad Jørgensen
Supervisor	Jan W. Thomsen
Supervisor	Jörg Helge Müller

Quantum Metrology group
The Niels Bohr Institute

January 14, 2022

Abstract

Optical frequency combs have since their first appearances spread widely across many different fields of research and are today used in everything from precise frequency metrology, to light detection and ranging, and astronomical spectrograph calibration. The generation of broadband optical frequency combs typically relies on the interaction between a nonlinear material and light. Using chip scale integrated waveguides can massively increase the nonlinear interaction strength as the large refractive index contrast creates small mode areas with high intensities, while simultaneously having the potential for small footprint and low cost devices. Silicon nitride is commonly used for integrated photonics in the telecommunication community due to its overlapping transparency with silica based fibres, and its large nonlinearity. This has allowed the development of silicon nitride integrated waveguide structures such as micro ring resonators, which have exploited the strong Kerr effect to generate dissipative soliton pulse based optical frequency combs.

In this work we investigate the dark dissipative Kerr soliton which in contrast to the more widespread bright solitons have larger conversion efficiencies and higher output powers. We study how the mode interactions between different optical modes allow for generation of dark solitons in a device with normal dispersion, and how the integrated micro-heater element can be used to control the mode interactions. This requires very precise measurements of the dispersion which we achieve by using a novel dispersion-free optical reference.

We present a scheme for automatically generating and stabilizing the dark pulse Kerr combs based on the measured optical comb power. We show that long term operation is possible, and utilize the setup in a multi-day full scale transmission experiment. Here the generated comb is used as a light source to transmit data through a 37 core multicore fibre and we achieve a total data transmission rate of 1.8 Pbit/s. We also present several issues the stability of the combs when using the heater based stabilization scheme.

In an effort to further stabilize the generated frequency comb we here show a compact acetylene based frequency reference which can be used as an absolute reference. The acetylene reference is based on noise immune cavity enhanced optical heterodyne molecular spectroscopy on the ro-vibrational $\mathrm{P}(16)\nu_1 + \nu_3$ transition in the carbon-13 acetylene molecule. We show that this spectroscopy technique yields superior performance over conventional absorption spectroscopy and we find a stability of 25 Hz at 0.2 s integration time.

Resume

Optiske frekvenskamme har siden deres opfindelse vundet indpas i mange forskellige forskningsområder, og bliver i dag brugt i alt fra højpræcisions frekvensmetrologi til optisk detektion og afstandsbedømmelse, og kalibrering af astronomiske spektrografer. Generationen af spektralt brede optiske frekvenskamme er typisk baseret på interaktionen imellem et ikke lineært materiale og lys. Ved at bruge chip størrelse integrerede bølgeledere kan man forøge den ikkelineære interaktionsstyrke massivt, fordi den store refraktive indeks kontrast skaber meget små optiske tilstandsområder. Det leder til høje intensiteter og giver samtidig potentiale for meget små og billige enheder. Siliciumnitrid bliver ofte brugt i integreret fotonik til telekommunikationsfeltet da det har en meget høj ikkelinearitet og et transparansvindue der overlapper med silica baserede fibre. Det har ført til udviklingen af siliciumnitrid baserede integrerede bølgelederstrukturer så som mikro ring resonatorer der udnytter den stærke ikkelineære Kerr effekt til at generere dissipative solitonpulsbaseret optiske frekvenskamme.

I denne afhandling undersøger vi mørke dissipative Kerr solitoner, der i kontrast til deres mere almenkendte lyse solitoner, har større konverteringseffektivitet og højere optisk udgangseffekt. Vi undersøger hvordan tilstandsinteraktioner imellem forskellige optiske tilstande tillader generationen af mørke solitoner i enheder der har normal dispersion. Vi ser samtidig på hvordan det integrerede varmelegeme kan bruges til at kontrollere tilstandsinteraktionerne. Det kræver en meget præcis måling af dispersionen som vi opnår ved at bruge en ny type dispersionsfri optisk reference.

Vi præsenterer en plan for automatisk generering og stabilisering af disse mørk puls Kerr kamme, der er baseret op den målte optiske effekt. Vi viser at operation er muligt over længere tid, og udnytter vores opstilling i et stort flerdages transmissionseksperiment. Her bliver den generede kam brugt som en lyskilde til at transmittere data gennem en 37-kerne multikerne optisk fiber, og vi opnår en total datatransmission på 1.8 Pbit/s. Vi fremlægger også flere problemer med stabiliteten af kammen når man bruger et varmelegeme baseret stabiliseringssystem.

For at stabilisere den generede frekvenskam yderligere præsenterer vi her en kompakt acetylenbaseret frekvensreference, som kan bruges som en absolut reference. Acetylenreferencen er baseret på en støjimmun og kavitetsforstærket optisk heterodyn molekylær spektroskopiteknik på den rotationsvibrationelle $P(16)\nu_1 + \nu_3$ overgang i karbon-13 acetylenmolekylet. Vi viser hvordan denne teknik yder bedre resultater end konventionel absorptionsspektroskopi, og vi opnår en stabilitet på 25 Hz ved 0.2 s integrationstid.

Acknowledgement

The work presented here has been performed over the last four years, and is without a doubt the biggest project I have ever taken on. I would not have been able to complete it without the help and support from a great number of people.

First of all I want to thank Jan W. Thomsen and Leif K. Oxenløwe for giving me the opportunity to work on this project, and later Jörg Helge Müller for stepping in and taking over a large part of the supervision duties. I first joined Jan's group as a bachelor student and was immediately taken in by his good-natured heart and strong focus on experimental work. Jan became head of the Niels Bohr Institute a few weeks after I started my Ph.D., and I am incredibly grateful for all the time he has dedicated to me from his very tight calendar. A big thanks goes to Jörg who always gave me his undivided attention whenever I needed to discuss a problem, often far longer than scheduled for.

I also want to thank my other NBI group colleagues for always being available for lively discussions and moral support. A big thanks goes to Stefan Schäffer who's experimental and managerial abilities I greatly admire. Martin Romme Henriksen was also always a source of motivation, and I enjoyed many late nights collaborating on the acetylene project with him. Together we delved into the wonders of optical telecommunication and quickly found ourselves in a sea of abbreviations. Bjarke Takashi Røjle Christensen came back to the group for a short while, but managed to leave a large impact on my perception of supervising. I also want to thank Mikkel Tang for his support especially in the early days of my Ph.D., where both Jan, Stefan and Martin where otherwise occupied. I am also grateful for having had the opportunity to work alongside Sofus Laguna Kristensen, Eliot Bohr, Julian Robinson, Valentin Cambier, among a few. Without the help of everybody at NBI I would not have been able to keep a foot in the atomic physics community.

The people at the SPOC centre taught me everything there is to know about optical communication, and Leif especially showed me the joy of working in the interface between engineering and fundamental research. A special note goes to Deming Kong for guiding me through the full data transmission setup and dedicating several consecutive days of his life for a very tiresome experimental run which became a cornerstone of my thesis.

I want to thank the people in Victor Torres-Company's group at Chalmers, especially Zhichao Ye and Òscar Helgason, who taught me everything about handling the silicon nitride chips and afterwards continued to allow me to pepper them with questions. Without their help we would never have gotten the frequency comb project off the ground at NBI.

Finally my writing process has been long and arduous, and I am not sure I would have gotten through it if it had not been for all the people supporting me. I believe I have learned as much about my self in this process as I have learned about physics. A big thanks must go to Christoffer Østfeldt and Freja Thilde Østfeldt for telling me the things I needed to hear, especially at times when I didn't want to hear them. To Esben Bork Hansen for always giving me perspective and insigt, and to Jophiel Wiis for always picking up the phone.

A special thanks goes to Freja Thilde Østfeldt, Sofie Holm-Janas, Valentin Cambier and Julian Robinson for proof reading sections of my thesis. I also have to thank Jörg for helping me through the writing process displaying a level of patience and understanding that I will never forget.

I want to thank my parents, who have been understanding and unwavering in their support during these past four years. Whether it was a shoulder to lean on or a listening ear, they have always been there for me. Their continuous encouragement and belief in my abilities have always driven me forward even when the path forward looked cloudy and uncertain.

Finally I would like to thank my partner Hattaya Rungruengsaowapak. Without her continuous support I would not have completed this and I am forever grateful that I could borrow her spine in the moments where my own seemed to malfunction. She has without any complaints put most of our life on hold for the past year so I could finalize this project. Her determination to never to shy away from the uncomfortable talks is the main reason for why this thesis exists.

Asbjørn Arvad Jørgensen

Copenhagen
January, 2022

Table of Contents

List Of Abbreviations

AOM acousto optical modulator. 96, 97, 104, 106

ASE amplified spontaneous emission. 46, 47, 48, 77, 110

BER bit error rate. 82

BIPM International Bureau of Weights and Measurements (Bureau international des poids et mesures). 24, 88, 113

BPF band pass filter. 46, 47, 48, 62, 77, 81, 110, 112

CUT channel under test. 78, 80, 81

DAC digital to analog converter. 51

DPK dark pulse kerr. 41, 43, 46, 47, 50, 58, 59, 110

DSP digital signal processing. 75, 77, 82, 85, 87, 106

DTU Technical University of Denmark. 72, 75, 82

ECL extended cavity laser. 70

EDFA erbium doped fibre amplifier. 46, 48, 54, 70, 71, 75, 77, 82, 83, 110, 113

EO electro optical. 45, 72

EOM electro optical modulator. 23, 89, 95, 96, 97, 99, 100, 101, 114

ESA electronic spectrum analyzer. 60, 111

FEC forward error correction. 79, 82, 83

FM frequency modulation. 92, 93, 114

FPGA field programmable gate array. 49

FSR free spectral range. 12, 18, 21, 22, 23, 26, 27, 33, 38, 40, 58, 63, 64, 68, 75, 76, 77, 89, 92, 96, 105, 109, 112

FWHM full width half maximum. 24

FWM four wave mixing. 6, 11, 12, 13, 17, 31, 36, 37, 38, 52, 54, 105, 108

LDPC low density parity check. 79, 82

LIDAR light detection and ranging. 3

LLE Lugiato-Lefever equation. 37

MLL mode locked laser. 3, 4

MRR micoring resonator. 5, 6, 7, 8, 12, 17, 19, 21, 22, 23, 24, 26, 37, 38, 39, 41, 45, 46, 62, 72, 73, 75, 76, 85, 105, 108, 109, 110

MZM Mach-Zehnder modulator. 63, 64, 77, 112

NBI the Niels Bohr Institute. 75

NICEOHMS noise immune cavity enhanced optical heterodyne molecular spectroscopy. 88, 93, 94, 96, 97, 98, 99, 100, 101, 102, 104, 106, 114

OFC optical frequency comb. 1, 2, 3

OSA optical spectrum analyzer. 60, 63, 112

OSNR optical signal to noise ratio. 72, 73, 74, 75, 77, 78, 113

PBS polarizing beam splitter. 77, 78

PC polarization controller. 23, 77, 109

PD photo diode. 23, 96, 109

PDH pound drever hall. 45, 89, 91, 92, 93, 96, 106, 114

PDM polarization division multiplexing. 70

PI Proportional and Integral. 51, 52, 53, 54, 61, 111

PID Proportional-Integral-Derivative. 49, 52, 54, 96, 111

PMD polarization mode dispersion. 77

PyRPL Python RedPitaya Lockbox. 49

QAM quadrature amplitude modulation. 69, 70, 79, 80, 82, 83, 113

RAM residual amplitude modulation. 94, 95, 96, 99, 100, 101, 102, 107, 114

RF radio frequency. 58, 59, 60, 63, 64, 69, 111, 112

S_3N_4 silicon nitride. 7, 8, 29, 41, 45, 76, 105

SDM space division multiplexing. 70, 72, 74, 75, 85, 106

SNR signal to noise ratio. 70, 71, 72, 79, 80, 84, 85, 113

SPF short pass filter. 46, 68, 77

VCO voltage controlled oscillator. 97

WDM wavelength division multiplexing. 3, 70, 71, 72, 75, 77, 106

WSS wavelength selective switch. 80

Preface

This thesis is a presentation of some of the work I have done as a Ph.D. fellow in the Quantum Metrology group at the Niels Bohr Institute (UCPH[1]). The project has been a joint collaboration between the Niels Bohr Institute and the Institute of Photonics at DTU[2]. More specifically I have worked in close collaboration with people from the SPOC[3] centre of excellence, where I have been an integrated part of Flagship D ”Silicon chip frequency comb and light sources”.

The work presented here focusses on integrated microring resonator devices fabricated in silicon nitride by the Ultrafast Photonics Laboratory at Chalmers Technical University. I am very grateful to have had to opportunity to visit and also borrow some of their devices for my research.

This is the first project in the Quantum Metrology group at NBI focussed on operating Kerr frequency combs and it has been a pleasure and a challenge to build a solid foundation for future projects.

The thesis is structured into four chapters: Prologue, Microring resonator Kerr frequency combs, Kerr combs for telecommunication, and The acetylene frequency reference.

Chapter one will give a brief introduction to frequency combs and the historical development. It will introduce the silicon nitride devices used in this thesis and a brief explanation on their setup. Finally it will lay the theoretical groundwork for understanding the processes involved in generating frequency combs from the Kerr nonlinearities.

Chapter two will focus on the investigation of the microring resonators. We will present measurements of the dispersion and how to use the data to simulate the generation of frequency combs. We will then introduce our generation and stabilization scheme and investigate the performance this.

Chapter three will describe a large collaborative telecommunication experiment where the stabilized frequency comb from chapter two was utilized. A brief introduction to frequency combs in the context of optical data communication will be presented followed by a detailed description of the transmission experiment.

Chapter four will showcase our acetylene based frequency references which would potentially be used to absolutely reference the Kerr frequency combs presented in the previous chapters. Here we will detail the setup and analyse the performance of our reference.

Publications

- Y. Zheng, M. Pu, A. Yi, B. Chang, T. You, K. Huang, A. N. Kamel, M. R. Henriksen, **A. A. Jørgensen**, X. Ou, and H. Ou, *High-quality factor, high-confinement microring resonators in 4H-silicon carbide-on-insulator.* Optics Express 27, 13053 (2019)

[1] University of Copenhagen
[2] Technical University of Denmark
[3] Silicon Photonics for Optical Communications

- S. A. Schäffer, M. Tang, M. R. Henriksen, **A. A. Jørgensen**, B. T. R. Christensen, and J. W. Thomsen, *Lasing on a narrow transition in a cold thermal strontium ensemble.* Phys. Rev. A 101, 013819 (2020).

- M. Tang, S. A. Schäffer, **A. A. Jørgensen**, M. R. Henriksen, B. T. R. Christensen, J. H. Müller, and J. W. Thomsen, *Cavity-immune spectral features in the pulsed superradiant crossover regime.* Phys. Rev. Research 3, 033258 (2021).

In Press

- **A. A. Jørgensen**, D. Kong, M. R. Henriksen, F. Klejs, Z. Ye, Ò. B. Helgason, H. E. Hansen, H. Hu, M. Yankov, S. Forchhammer, P. Andrekson, A. Larsson, M. Karlsson, J. Schröder, Y. Sasaki, K. Aikawa, J.W. Thomsen, T. Morioka, M. Galili, V. Torres-Company, and L. K. Oxenløwe, *Petabit-per-second data transmission using a chip-scale microcomb ring resonator source* Nature Photonics

Conference contributions

- Y. Zheng, M. Pu, A. Yi, A. N. Kamel, M. R. Henriksen **A. A. Jørgensen**, X. Ou, H. Ou. *Fabrication of High-Q, High-Confinement 4H-SiC Microring Resonators by Surface Roughness Reduction.* in Conference on Lasers and Electro-Optics (CLEO 2019) SM2O.7.

- D. Kong, **A. A. Jørgensen**, M. R. Henriksen, F. Klejs, Z. Ye, Ò. B. Helgason, H. E. Hansen, H. Hu, M. Yankov, S. Forchhammer, P. Andrekson, A. Larsson, M. Karlsson, J. Schröder, Y. Sasaki, K. Aikawa, J.W. Thomsen, T. Morioka, M. Galili, V. Torres-Company, and L. K. Oxenløwe, *Single Dark-Pulse Kerr Comb Supporting 1.84 Pbit/s Transmission over 37-Core Fiber.* in Conference on Lasers and Electro-Optics (CLEO 2020), JTh4A.7. Post Deadline paper

Chapter 1

Prologue

An optical frequency comb (OFC) is a spectral structure named after its resemblance to the more commonly known household item (see Figure 1.1). But

Figure 1.1: ***Left*** *Ordinary comb.* ***Right*** *Spectrum of a frequency comb.*

compared to its mundane cousin, the OFC has had a major impact in the field of precision measurements, to a point where it has even received half a nobel prize.

One of the most important properties of an OFC is that the frequency of the n'th tooth can be completely represented by only two parameters; the repetition rate f_r, and the frequency offset from zero f_0:

$$f_n = nf_r + f_0, \tag{1.0.1}$$

In the time domain picture, a frequency comb is an electrical field oscillating at some optical frequency modified by a slowly varying, periodic envelope. This creates a train of pulses with a pulse spacing of $T_r = \frac{1}{f_r}$. If the pulse spacing is not an exact integer of oscillation periods of the electrical field, there will be a small and varying phase offset between the peak of the pulse envelope, and the electrical field. This phase offset will vary in time and gives rise to the frequency offset:

$$f_{ceo} = \frac{1}{2\pi} \cdot \frac{\mathrm{d}}{\mathrm{d}t}\phi_{CEO} \tag{1.0.2}$$

Figure 1.2 illustrates a OFC in both the time and frequency domain. The shape of the OFC in the frequency domain depends entirely on the shape of a single pulse, while the repetition rate is determined by the pulse spacing.

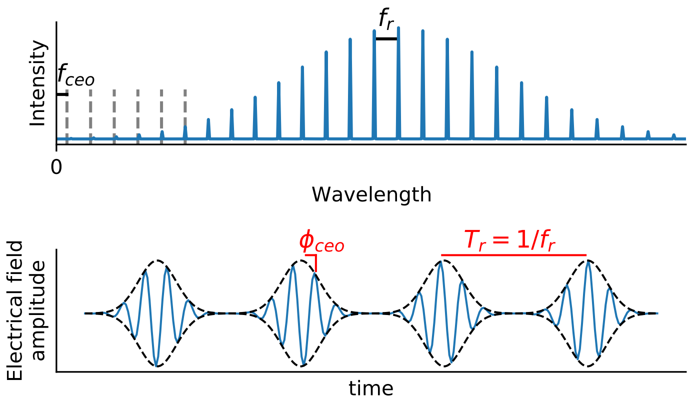

Figure 1.2: ***Top*** *Frequency domain picture of a frequency comb.* ***Bottom*** *Equivalent time domain picture, as a pulse train, with f_r and ϕ_{ceo} represented.*

1.1 Applications of frequency combs

Because methods have been found to detect and lock f_r and f_{ceo} in the RF domain, combs have advanced several different fields, while fundamentally all relying on the same fact, that OFCs produce a well defined equidistant grid of frequencies over a very broad wavelength range.

In the field of precision metrology, and optical atomic clocks, OFCs were immediately used to compare optical transitions different atomic species, and even measure the absolute frequency of optical atomic transitions. Because the repetition rate of many frequency combs is in the MHz range, it has been possible to do an absolute measurement of the atomic clock frequency referenced directly to the 9.192 631 770 GHz transition in Caesium-133 defining the second[1]. To put this into perspective, an absolute frequency measurement of the $^1S_0 \leftrightarrow {}^3P_0$ intercombination line of Calcium-40 was done at PTB in 1996[2]. This involved 19 oscillators including quartz oscillators, masers and lasers and had a final uncertainty of 430 Hz. In 2001 NIST[3] measured it again with an uncertainty of 26 Hz, using an OFC link with only 4 transfer oscillators between the optical Ca signal and the microwave Cs standard.

In 2007 OFCs were proposed as a way of calibration astronomical spectrographs in order to increase the sensitivity[4], and has since been tested and installed in several telescopes around the world[5]–[9].

1. BIPM, *Le Système International d'unités (SI)* (2019)
2. Schnatz et al., "Phase Coherent Frequency Measurement of Visible Radiation" (1996)
3. Udem et al., "Absolute Frequency Measurements of the Hg+ and Ca Optical Clock Transitions with a Femtosecond Laser" (2001)
4. Murphy et al., "High-Precision Wavelength Calibration of Astronomical Spectrographs with Laser Frequency Combs" (2007)
5. Wilken et al., "High-Precision Calibration of Spectrographs" (2010)
6. Li et al., "Astro-Comb Calibration of an Echelle Spectrograph" (2010)
7. Ycas et al., "Demonstration of On-Sky Calibration of Astronomical Spectra Using a 25 GHz near-IR Laser Frequency Comb" (2012)
8. Glenday et al., "Operation of a Broadband Visible-Wavelength Astro-Comb with a High-Resolution Astrophysical Spectrograph" (2015)
9. McCracken et al., "Wavelength Calibration of a High Resolution Spectrograph with a Partially Stabilized 15-GHz Astrocomb from 550 to 890 Nm" (2017)

OFCs can also be used in broadband spectroscopy, where using two combs simultaneously with slightly different repetition rates can convert the optical absorption features to a RF signal, which is easily detectable by ordinary electronics[10]–[12].

A related concept was proven in 2000[13] where two combs are used for rangefinding in what is known as light detection and ranging (LIDAR). Since then the field has progressed rapidly [14], with the main disadvantage being the relatively large size of frequency combs. However this was recently overcome by demonstrating LIDAR with soliton microcombs [15].

While it is common to lock both f_r and f_{ceo} of an OFC, one can let f_r be free and instead lock a comb line to some other optical reference, for example a ultrastable cavity. This then transfers the stability of the cavity to the repetition rate, and is a way of generating ultra stable microwave signals, based on the repetition rate[16].

Finally combs can also be used in telecommunication as highly efficient wavelength division multiplexing (WDM) sources. In WDM transmissions, multiple light sources at different wavelengths are each datamodulated with individual data and interleaved before being transmitted in the same spatial fibre mode. Light sources typically consist of arrays of lasers, but the spectral properties of OFCs lend themselves naturally to this[17]–[19]. This particular application does in fact not need the full stability of locking neither the repetition rate or the carrier envelope offset, and can therefore utilize combs that are less than an octave wide. Telecommunication can also take advantage of the coherent nature of the OFC lines to achieve super-Nyquist transmission rates [20].

The size and power consumption of OFCs are not an issue for the applications mentioned here, with the exception of LIDAR and telecommunication. Here power, and especially heat generation, and size are important factors in order to keep the cost down if they are to be incorporated into industry. There has therefore been a substantial push towards OFCs generated by integrated photonics using highly nonlinear materials and nanofabrication.

Generation of frequency combs

Generating an OFC was historically done using mode locked lasers (MLLs), which essentially produce narrow pulses by through superposition of multiple cavity modes with a fixed phase relation between them. This was experi-

10. Schiller, "Spectrometry with Frequency Combs" (2002)
11. Keilmann et al., "Time-Domain Mid-Infrared Frequency-Comb Spectrometer" (2004)
12. Coddington et al., "Dual-Comb Spectroscopy" (2016)
13. Minoshima et al., "High-Accuracy Measurement of 240-m Distance in an Optical Tunnel by Use of a Compact Femtosecond Laser" (2000)
14. Lee et al., "Time-of-Flight Measurement with Femtosecond Light Pulses" (2010)
15. Riemensberger et al., "Massively Parallel Coherent Laser Ranging Using a Soliton Microcomb" (2020)
16. Fortier et al., "Generation of Ultrastable Microwaves via Optical Frequency Division" (2011)
17. Rademacher et al., "10.66 Peta-Bit/s Transmission over a 38-Core-Three-Mode Fiber" (2020)
18. Marin-Palomo et al., "Microresonator-Based Solitons for Massively Parallel Coherent Optical Communications" (2017)
19. Hu et al., "Single-Source Chip-Based Frequency Comb Enabling Extreme Parallel Data Transmission" (2018)
20. Mazur et al., "Joint Superchannel Digital Signal Processing for Effective Inter-Channel Interference Cancellation" (2020)

mentally achieved in the late nineties [21],[22], where MLLs based on Titanium:Sapphire crystals placed in free space cavities were used to achieved sub-6-fs pulses. Here they hit a hard limit, as such a short pulse only allowed for 2.3 electrical field oscillations in each pulse. The carrier envelope offset could not be directly detected and stabilized as it is fundamentally a phase shift on an optical carrier wave, and even today we are far from being able to electrically directly detect optical frequencies, much less phases. Without a stable carrier envelope offset, the intensity in each pulse would fluctuate and severely limit any further nonlinear effects which relied on intensity.

The problem of detecting the carrier envelope offset was solved in 1999[23] where several solutions were proposed; one of them being *f-2f* locking which stated that f_{ceo} could be measured by frequency doubling part of the comb spectrum and beating it against itself. This would create a downconverted beat note which only relied on f_{ceo}. Using Equation 1.0.1 this can easily be shown:

$$f_2 - 2f_1 = 2(n_1 f_r + fceo) - n_2 f_r + f_{ceo} \tag{1.1.1}$$
$$= (n_2 - 2n_1) f_r + f_{ceo}, \tag{1.1.2}$$

where $n_2 = 2n_1$. This does require an octave spanning comb, and at the time, MLLs were a few hundred nm short of being wide enough for this technique.

The solution to this came in the form of highly nonlinear fibres. These fibres could achieve large intensities and long interaction lengths due to the small and well confined mode areas. Furthermore the dispersion could be designed to allow wider generation. It was first demonstrated in 1999 where 100 fs pulses were launched into a photonic crystal fibres and spectrally broadened to cover more than 1000 nm[24]. This was demonstrated again half a year later in standard telecom fibre that had been tapered down[25].

This recipe for frequency comb generation; a pulsed source and a nonlinear material to broaden the spectrum, has been implemented in various different ways. Sometimes combining the pulsed source and the nonlinear material such as octave spanning MLLs [26], and microresonator based combs[27]. Or full fibre solutions based on fibre lasers [28], or electro optical combs created by EO modulating continuous wave sources[29].

Microresonator frequency combs

Microresonator frequency combs, or micro-combs, combine the source and the nonlinear material by creating a travelling wave resonator out of a highly nonlinear material. The aim is to create compact, low power devices, which can

21. Cho et al., “Sub-Two-Cycle Pulses from a Kerr-lens Mode-Locked Ti : Sapphire Laser”(1999)
22. Sutter et al., “Semiconductor Saturable-Absorber Mirror–Assisted Kerr-lens Mode-Locked Ti:Sapphire Laser Producing Pulses in the Two-Cycle Regime”(1999)
23. Telle et al., “Carrier-Envelope Offset Phase Control: A Novel Concept for Absolute Optical Frequency Measurement and Ultrashort Pulse Generation”(1999)
24. Ranka et al., “Visible Continuum Generation in Air–Silica Microstructure Optical Fibers with Anomalous Dispersion at 800 Nm”(2000)
25. Birks et al., “Supercontinuum Generation in Tapered Fibers”(2000)
26. Fortier et al., “Octave-Spanning Ti:Sapphire Laser with a Repetition Rate >1 GHz for Optical Frequency Measurements and Comparisons”(2006)
27. Del’Haye et al., “Optical Frequency Comb Generation from a Monolithic Microresonator”(2007)
28. Leopardi et al., “Single-Branch Er:Fiber Frequency Comb for Precision Optical Metrology with 10-18 Fractional Instability”(2017)
29. Beha et al., “Electronic Synthesis of Light”(2017)

potentially be integrated into photonic circuits. Through the nonlinearity of the material, power can be transferred between the pumped mode and the nearby resonator modes, thus creating new frequency components. The amount of power transferred is proportional to the nonlinearity and the length of the material, and because microresonator sizes are typically on the order of hundreds of µm to several mm, the optical path length of a single round trip is very small. However, by creating resonators with low loss, the light will propagate several round trips, thus effectively increasing the nonlinear path length. Simultaneously the low losses will allow for a large build up of power, effectively enhancing the nonlinear processes.

The first class of microresonators were based on whispering gallery mode resonances, and guided light on the inside edge of a large surface. These would typically take the form of toroids, spheres, or discs, as shown on Figure 1.3. While they would have extremely high finesse with Q-values in the tens or hundreds of millions [27],[30], and were the first devices to show frequency comb generation, they all relied on evanescent coupling through tapered fibres. This offers a high degree of control over the coupling but also makes it unfeasible for large scale manufacturing. The micoring resonator (MRR) is a slightly different device, as it is not a whispering gallery mode resonator but rather a guided mode resonator, similar to a fibre loop cavity. It is etched directly into the chip, which allows simultaneous fabrication of nearby straight waveguides which can be used to couple light into the resonator. Due to fabrication imperfections, and especially side wall roughness, they have lower Q-values ($10^5 - 10^7$), however their larger nonlinearity still allow frequency comb generation[31],[32].

Over time the fabrication process has continuously improved, now allowing for Q-values as high as 400×10^6[33].

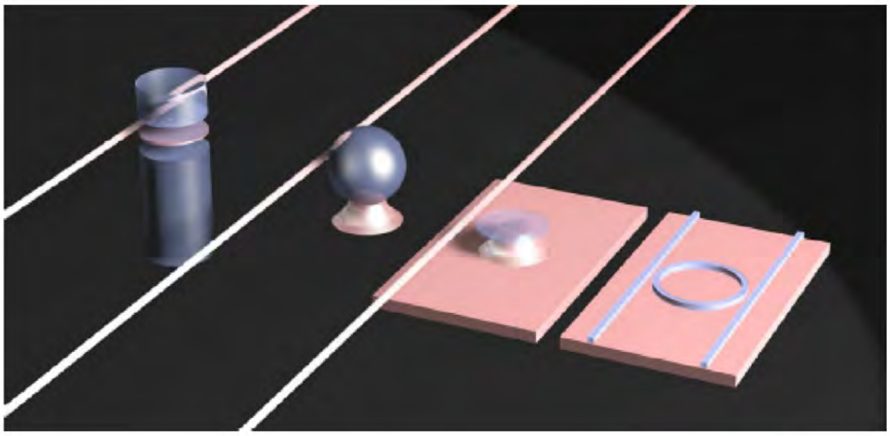

Figure 1.3: *Different types of microresonators. From left: Monolithic toroid, Microsphere, Microdisc, Microring. Adapted from [34]*

27. Del'Haye et al., "Optical Frequency Comb Generation from a Monolithic Microresonator" (2007)
30. Armani et al., "Ultra-High-Q Toroid Microcavity on a Chip" (2003)
31. Levy et al., "CMOS-compatible Multiple-Wavelength Oscillator for on-Chip Optical Interconnects" (2010)
32. Razzari et al., "CMOS-compatible Integrated Optical Hyper-Parametric Oscillator" (2010)
33. Puckett et al., "422 Million Intrinsic Quality Factor Planar Integrated All-Waveguide Resonator with Sub-MHz Linewidth" (2021)

Soliton combs

While micro resonator devices can produce multiple coherent comb lines through four wave mixing (FWM), it does not necessarily equate to ultra short pulses in the time domain. This is only achieved if the frequency components have a fixed phase relation to each other. Normally a travelling pulse would broaden or narrow during propagation due to the dispersion causing the high frequency components to propagate faster or slower than the low frequency components. However this effect can be counterbalanced by the nonlinear Kerr effect which creates a intensity dependent refractive index. For certain pulse shapes, the intensity gradient due to the pulse will cause the nonlinear Kerr effect to counteract the dispersion effect, effectively leading to a pulse which does not change during propagation. Such pulses are known as temporal solitons, and can be generated in micro resonators under certain parameter conditions.

An example of such a soliton is shown in the left plot of Figure 1.4 (Adapted from [35]). The frequency spectrum has the expected sech^2 shape and the time domain, shown in the inset, reveals a sharp pulse. This type of soliton can only exist in devices with anomalous dispersion, however normal dispersion devices can support their own types of solitons known as dark solitons, or dark pulses. The frequency spectrum and time domain plot of a dark soliton is shown on the right plot of Figure 1.4. It resembles an inverted pulse, which also changes the sign of the nonlinear Kerr effect, thus allowing soliton generation in normal dispersion materials. While dark solitons in microring resonators have been studied [36]–[41], they have largely been ignored in favour of their brighter cousins [42]–[46].

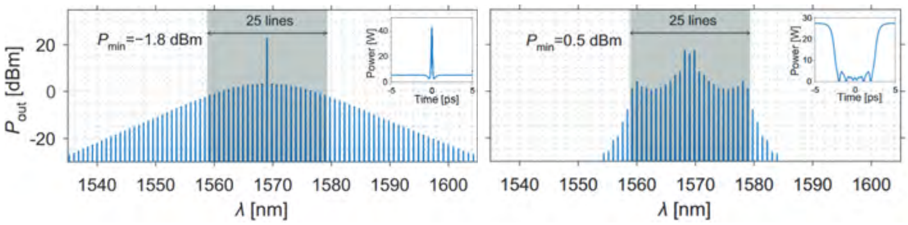

Figure 1.4: *Simulated frequency spectra of a bright soliton(left) and a dark pulse(right) in a MRR. The inset in each plot shows the time domain view of the pulse. Adapted from [35]*

35. Helgason et al., "Superchannel Engineering of Microcombs for Optical Communications" (2019)
36. Matsko et al., "Normal Group-Velocity Dispersion Kerr Frequency Comb" (2012)
37. Liang et al., "Generation of a Coherent Near-Infrared Kerr Frequency Comb in a Monolithic Microresonator with Normal GVD" (2014)
38. Liu et al., "Investigation of Mode Interaction in Optical Microresonators for Kerr Frequency Comb Generation" (2014)
39. Parra-Rivas et al., "Origin and Stability of Dark Pulse Kerr Combs in Normal Dispersion Resonators" (2016)
40. Nazemosadat et al., "Switching Dynamics of Dark-Pulse Kerr Frequency Comb States in Optical Microresonators" (2021)
41. Helgason et al., "Dissipative Solitons in Photonic Molecules" (2021)
42. Herr et al., "Temporal Solitons in Optical Microresonators" (2014)
43. Yi et al., "Active Capture and Stabilization of Temporal Solitons in Microresonators" (2016)
44. Guo et al., "Universal Dynamics and Deterministic Switching of Dissipative Kerr Solitons in Optical Microresonators" (2017)
45. Shen et al., "Integrated Turnkey Soliton Microcombs" (2020)
46. Wan et al., "Frequency Stabilization and Tuning of Breathing Soliton in SiN Microresonators" (2020)

1.2 Silicon nitride microring resonators

Since its breakthrough as an optical waveguide in 1968[47], silicon (Si) has become a key technology in today's photonic integrated circuits[48]. Partially also due to the fact that silicon is heavily used in electric integrated circuits, and thus can share much of the existing manufacturing infrastructure. One of the most promising candidates for the next step in integrated nonlinear photonics is silicon nitride (S_3N_4). It has a very strong nonlinearity, ultra low optical losses, and a much wider transparency bandwidth window compared to Si[49]. The Ultrafast Photonics Laboratory at Chalmers University of Technology have designed and fabricated several S_3N_4 MRRs. We have borrowed a chip designed and fabricated with normal dispersion for dark pulse Kerr comb generation.

The chip has multiple devices (resonators) which all are designed as all-pass devices, where a single waveguide is laid out near a ring resonator. A photograph of such a device can be seen in Figure 1.5(a). The ring resonator waveguides are 1850 nm wide and 600 nm tall[50], with all the devices having intrinsic Q-values on the order of 10^7. They are fabricated in S_3N_4 on Si, with a cladding of silicon oxide (SiO_2), as shown on the composite sketch Figure 1.5(b). The devices have integrated micro-heaters connected to the

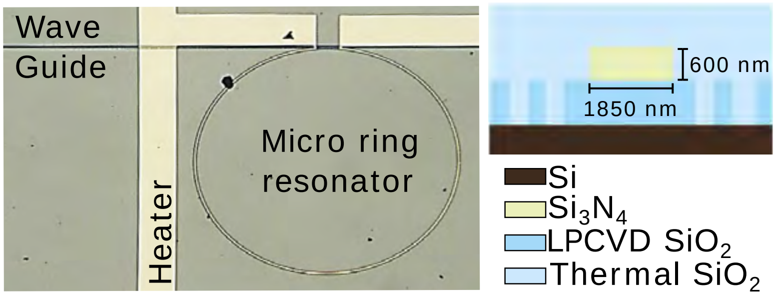

(a) (b)

Figure 1.5: ***a)*** *Camera image of one of the devices.* ***b)*** *Sketch of the device composition. The Platinum micro-heater is not included here. Borrowed and adapted from [50].*

resonators device. The heaters are made of platinum with a width of 4000 nm and a height of 200 nm. It is visible as a thin white strip underneath the ring resonator in Figure 1.5(a). The thick white stripes are part of the heater and act as connection pads for the electrical contacts. The resistance in the heater is 320 Ω and has been tested up to 20 V (1.5 W) without any degradation.

The data presented in this thesis will come from three different devices:

- Gap 2. This was the first device we used, and also the device utilized in the data transmission experiment described in Chapter 3. Shortly after the chip got damaged and this device became unusable.

47. Soref et al., "All-Silicon Active and Passive Guided-Wave Components for Lambda = 1.3 and 1.6 Um" (1986)
48. Thomson et al., "Roadmap on Silicon Photonics" (2016)
49. Liu et al., "High-Yield, Wafer-Scale Fabrication of Ultralow-Loss, Dispersion-Engineered Silicon Nitride Photonic Circuits" (2021)
50. Ye et al., "High-Q Si 3 N 4 Microresonators Based on a Subtractive Processing for Kerr Nonlinear Optics" (2019)

- Gap 1. This device was used after Gap 2 broke. It was missing one of the dispersion features we saw in Gap 2, and was used to confirm many of the measurements done on the Gap 2 device, including the stability measurements.
- Gap 3. This device was used because Gap 1 did not display the same dispersion features as Gap 2.

All devices feature coupling losses around 2 dB to 4 dB per facet and they all perform very similar in terms of comb generation and stability.

The integrated heater element

The integrated micro heaters allow us to shift the resonances of the MRR through the thermo-optic effect. S_3N_4 has a positive thermo-optic coefficient, which means the refractive index changes as[51]:

$$\frac{\mathrm{d}n}{\mathrm{d}T} = 2.45 \times 10^{-5}/°\mathrm{C}. \tag{1.2.1}$$

When the temperature is increased, both the refractive index and the physical path length of the resonator will increase. While these two effects work against each other in influencing the optical path length, the physical change due to thermal expansion is much smaller than the refractive index change. This causes the resonances to shift down in frequency as the temperature is increased.

There are three ways we can influence the temperature of the MRR. Firstly we can control the power of the heater element. This is the most efficient way and will be our main source of thermal control. Secondly we can control the temperature of the chip holder which will also change the temperature of the chip. This also changes the temperature of the chip, and we will refer to is as the *base temperature*. This is controlled by a Peltier element, and is orders of magnitude slower due to the much larger thermal mass. The main goal of the base temperature control is to compensate for fluctuating air temperatures in the laboratory. Lastly the optical power inside the MRR will change the temperature through scattering and losses. As more power is coupled into the ring, the temperature will increase due to absorption. One advantage of thermally controlling the chip becomes obvious when using pump lasers that do not have a built in frequency tuning method. The heater can then be used to control the detuning of the pump, and generate solitons while the pump laser stays at a fixed frequency. This is especially useful if the pump laser is locked to some reference, either a cavity for narrowing the linewidth, or a gas to act as an absolute reference.

Chip setup

The chips are placed on a copper base which is temperature controlled through a Peltier element. This allows for changes in the chip base temperature while localized heating is done through the DC probes which connect to the on-chip

51. Arbabi et al., "Measurements of the Refractive Indices and Thermo-Optic Coefficients of Si_3N_4 and SiO_x Using Microring Resonances."(2013)

heater. We use lensed fibres on each side of the chip to couple light into and out of the straight bus waveguide. The lensed fibres have a focussed spot size of 2.5 µm and a working distance of 14 µm. They are single mode and AR-coated, but not polarization maintaining, as this would require an additional rotational element around the chip. The lensed fibres are securely mounted in v-shaped groves in steel holders, which are in turn attached to Piezo controlled 3D translation stages.

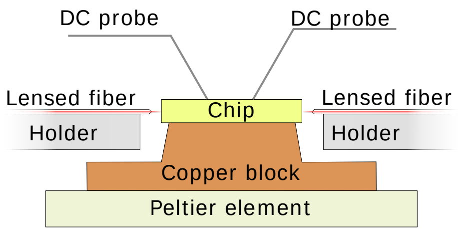

Figure 1.6: *Chip holder setup. The peltier element keeps the chip base at a constant temperature. Localized heating of the chip is done through the DC probes connecting to the on chip micro-heater element. The lensed fibres are mounted in a v groove in the fibre holders. The holders are connected to piezocontrolled 3D tranlation stages.*

1.3 Introduction to nonlinear optics

In this section we will describe the nonlinear processes important for understanding the formation of solitons in microring resonators. This will be split into two different parts, one focusing on four-wave mixing, which is responsible for turning the CW pump into a train of pulses, and then the self phase modulation and dispersion, which govern the propagation of the pulses and determines the conditions for soliton states.

Four wave mixing

As always we start with Maxwell's equations in a medium:

$$\nabla \cdot \mathbf{E} = \rho \tag{1.3.1}$$

$$\nabla \times \mathbf{E} = -\frac{\partial \mathbf{B}}{\partial t} \tag{1.3.2}$$

$$\nabla \cdot \mathbf{H} = 0 \tag{1.3.3}$$

$$\nabla \times \mathbf{H} = \frac{\partial \mathbf{D}}{\partial t} + \mathbf{J} \tag{1.3.4}$$

We will assume that the mediums we work with will have no free charges,and thus no free currents either, such that that $\rho = \mathbf{J} = 0$.

In a dielectric medium is it convenient to consider the displacement field $\mathbf{D}$, which is the sum of the electric field, and the field generated by the polarization induced by the bound electrons being affected by the aforementioned field. $\mathbf{D}$ is defined as:

$$\mathbf{D} = \epsilon_0 \mathbf{E} + \mathbf{P}, \tag{1.3.5}$$

To account for nonlinearities in the medium, we will allow the polarization $\mathbf{P}$ to be nonlinearly dependent on the electrical field:

$$\mathbf{P} = \epsilon_0 \chi^{(1)} \mathbf{E} + \epsilon_0 \chi^{(2)} \mathbf{E}\mathbf{E} \ + \epsilon_0 \chi^{(3)} \mathbf{E}\mathbf{E}\mathbf{E} \ldots, \tag{1.3.6}$$

where we have expanded in a power series following Boyd [52].

We can now take the curl of Maxwell's equation and perform the usual vector calculus:

$$\nabla \times \nabla \times \mathbf{E} = -\frac{\partial \nabla \times \mathbf{B}}{\partial t} \tag{1.3.7}$$

$$\nabla(\nabla \cdot \mathbf{E}) - \nabla^2 \mathbf{E} = -\frac{\partial \mu_0 \frac{\partial \mathbf{D}}{\partial t}}{\partial t} \tag{1.3.8}$$

$$\nabla^2 \mathbf{E} - \mu_0 \epsilon_0 \frac{\partial^2 \mathbf{E}}{\partial t^2} = \mu_0 \frac{\partial^2 \mathbf{P}}{\partial t^2} \tag{1.3.9}$$

It is common to separate out the first term of the polarization, as this is linear in the electrical field, and can gathered with the second term on the left hand side:

$$\nabla^2 \mathbf{E} - \frac{\epsilon_r}{c^2} \frac{\partial^2 \mathbf{E}}{\partial t^2} = \mu_0 \frac{\partial^2 \mathbf{P}^{NL}}{\partial t^2}, \tag{1.3.10}$$

where $\epsilon_r = 1 + \chi^{(1)}$. This is the general wave equation from which we will derive the propagation of electrical fields in nonlinear materials.

We will only be considering propagation in waveguides such as ridge waveguides on microchips or fibres, and we will assume that they only support a single optical mode. This means we can write the total electrical field as a sum of monochromatic plane waves, with the radial extension being the effective mode area A_{eff} of the waveguide, which is assumed identical for all frequencies

$$E(z,t) = \sum_n \tilde{E}_n = \sum_n E_n e^{i(\beta_n z + \omega_n t)} + c.c. \tag{1.3.11}$$

Where we assume the fields propagate in the z direction with only one polarization. Here ω_n is the angular frequency, β_n is the propagation constant, and E_n is the amplitude of the electrical field.

The nonlinear polarization can now be written as:

$$P^{NL}(z,t) = \epsilon_0 \chi^{(3)} E(z,t)^3 = \epsilon_0 \chi^{(3)} \sum_{klm} \tilde{E}_k \tilde{E}_l \tilde{E}_m, \tag{1.3.12}$$

If we imagine an electrical field composed of three frequencies:

$$E(z,t) = E_1 e^{i(\beta_1 z + \omega_1 t)} + E_2 e^{i(\beta_2 z + \omega_2 t)} + E_3 e^{i(\beta_3 z + \omega_3 t)} + c.c. \tag{1.3.13}$$

then the nonlinear polarization will take the form:

$$\begin{aligned} P^{NL}(z,t) = \epsilon_0 \chi^{(3)} \Big(& E_1^3 e^{i(3\beta_1 z + 3\omega_1 t)} + E_2^3 e^{i(3\beta_2 z + 3\omega_2 t)} + E_3^3 e^{i(3\beta_3 z + 3\omega_3 t)} \\ & + (3|E_1|^2 + 6|E_2|^2 + 6|E_3|^2) E_1 e^{i(\beta_1 z + \omega_1 t)} \\ & + 6 E_1 E_2 E_3^* e^{i((\beta_1 + \beta_2 - \beta_3) z + (\omega_1 + \omega_2 - \omega_3) t)} \\ & + 3 E_1^2 E_2 e^{i((2\beta_1 + \beta_2) z + (2\omega_1 + \omega_2) t)} \\ & + \cdots \Big) \end{aligned} \tag{1.3.14}$$

52. Boyd, *Nonlinear Optics - Third Edition* (2008)

where only a few of the terms are shown to illustrate that electrical fields at some frequencies will affect the polarization at the sum/difference frequencies. This is what gives rise to FWM, and processes such as third harmonic generation, which are represented by the first three terms in the equation above. To simplify things we realize that we can write the nonlinear polarization as a sum of single frequency terms:

$$P^{NL}(z,t) = \sum_n \tilde{P}_n^{NL} = \sum_n \epsilon_0 \chi_n^{(3)} E \cdot E \cdot E \Big|_{\omega_n = \pm\omega_1 \pm\omega_2 \pm\omega_3} \tag{1.3.15}$$

We can then write a wave equation which holds for each frequency component independently:

$$\nabla^2 \tilde{E}_n - \frac{\epsilon_r}{c^2}\frac{\partial^2 \tilde{E}_n}{\partial t^2} = \mu_0 \frac{\partial^2 \tilde{P}_n^{NL}}{\partial t^2}, \tag{1.3.16}$$

This will allow us to understand how the different fields evolve while propagating through nonlinear materials, with the nonlinear polarization allowing fields different frequencies to combine and add to the dynamics of $\tilde{E}_n$. This is also what is known as the frequency matching condition, and only holds true if we restrict ourselves to parametric processes, where there will be no energy transfer between the electrical fields and the medium.

The total electrical field might consist of more than 3 different frequencies, but as only three can interact in the nonlinear polarization (four if you count the resulting field) we can without loss of generality treat them three fields at a time.

If we then assume that the amplitude of each electrical field might vary slowly as they propagate through the nonlinear medium we can write the field as:

$$\tilde{E}_n = E_n(x,y,z)e^{i(\beta_n z + \omega_n t)} + c.c. \tag{1.3.17}$$

where we include the radial part of the electrical field by assuming all fields propagate in the same mode with the same effective mode area A_{eff}. Note that we now neglect any time dependence on E_n and only assume it varies with propagation length z.

We can then write 4 coupled differential equations as done in [53]:

$$\frac{dE_1}{dz} = i\gamma\left(\left(|E_1|^2 + |E_2|^2 + |E_3|^2\right)E_1 + 2E_2^* E_3 E_4 e^{i\Delta\beta z}\right) \tag{1.3.18}$$

$$\frac{dE_2}{dz} = i\gamma\left(\left(|E_1|^2 + |E_2|^2 + |E_3|^2\right)E_2 + 2E_1^* E_3 E_4 e^{i\Delta\beta z}\right) \tag{1.3.19}$$

$$\frac{dE_3}{dz} = i\gamma\left(\left(|E_1|^2 + |E_2|^2 + |E_3|^2\right)E_3 + 2E_1 E_2 E_4^* e^{-i\Delta\beta z}\right) \tag{1.3.20}$$

$$\frac{dE_4}{dz} = i\gamma\left(\left(|E_1|^2 + |E_2|^2 + |E_3|^2\right)E_4 + 2E_1 E_2 E_3^* e^{-i\Delta\beta z}\right) \tag{1.3.21}$$

where

$$\Delta\beta = \beta_3 + \beta_4 - \beta_1 - \beta_2$$

and

$$\gamma = \frac{n_2\omega}{cA_{eff}}$$

53. Agrawal, *Nonlinear Fiber Optics*(2001)

which is the nonlinear parameter. here n_2 is the nonlinear index coefficient and represents the nonlinear polarization as an intensity dependent refractive index. If we now assume that E_1 and E_2 are much stronger than E_3 and E_4, and also the same frequency such that they represent a very strong pump field. One can then follow the derivation from [53] and arrive at an equation for the gain of the $E_{3,4}$ fields:

$$g = \sqrt{(\gamma 2\sqrt{P_1 P_2})^2 - (\Delta\beta/2 + \gamma/2(P_1 + P_2))^2} \tag{1.3.22}$$

which simplifies if we assume the two pump fields are degenerate in frequency, with a combined power of $P_1 + P_2 = 2P_0$:

$$g = \sqrt{(\gamma 2P_0)^2 - (\Delta\beta/2 + \gamma P_0)^2} \tag{1.3.23}$$

The first term in the gain equations represents the self-phase modulation and the last term represents the phase mismatch between the pump and the $E_{3,4}$ fields, together with the cross phase modulation on the $E_{3,4}$ fields from the pump fields. If $E_{1,2}$ are the pump fields, then the photon energy conservation requirement will require that:

$$\omega_1 + \omega_2 = 2\omega_0 = \omega_3 + \omega_4 \tag{1.3.24}$$

$$2\omega_0 = (\omega_0 + \Delta\omega) + (\omega_0 - \Delta\omega) \tag{1.3.25}$$

which indicates that the FWM process will create two sidebands at $\pm\Delta\omega$ around the pump frequency. This is also visually illustrated on Figure 1.7 as degenerate FWM.

If now one of the pump fields is instead one of the newly generated fields, then this can also participate in a FWM process which will result in asymmetrically placed sidebands due to the pump fields not being equal in frequency, as shown on Figure 1.7. When a FWM process contains frequencies that were already generated through FWM it is called a cascaded FWM process.

From the gain equations we see that there will be a gain of the two sideband frequencies as long as $0 > \Delta\beta > -4\gamma P_0$.

FWM inside a microring resonator

The MRR structure adds some additional boundary conditions because while the FWM process can create a continuum of frequencies, as long as there is gain, only those frequencies which match with the modes of the ring resonator will be supported. Ultimately this leads to only generating frequencies which are located an integer number of free spectral range (FSR) away from the pump, thereby creating a frequency comb instead of a broad continuum.

The differential equations so far have been made in the CW approximation, assuming the propagating electrical field to be CW, and while this is a good description initially, it breaks down as more and more frequency components are created from the FWM process. As the cascaded FWM process continues, the time domain will also change from CW to a pulse, with the pump frequency as the carrier frequency, but with a spatially varying envelope. This is illustrated

53. Agrawal, *Nonlinear Fiber Optics*(2001)

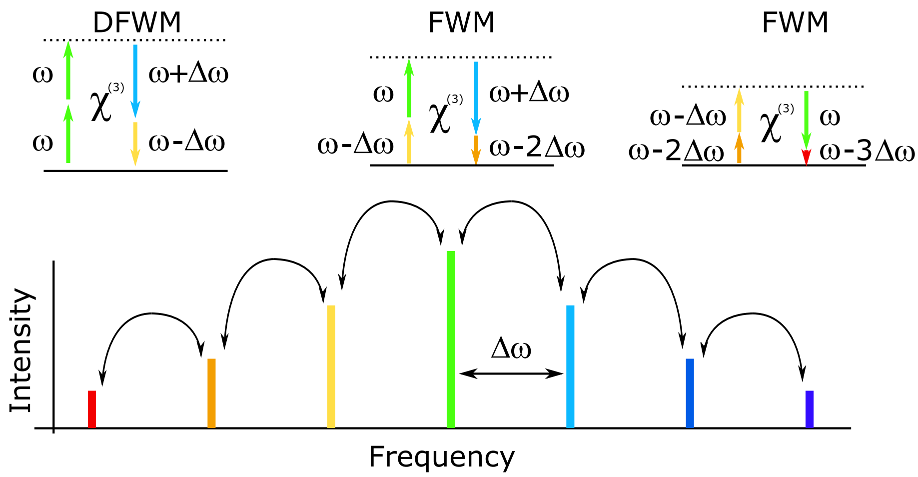

Figure 1.7: *Illustration of the FWM process. The top images illustrate the frequency matching condition, with the leftmost being degenerate FWM (DFWM). The bottom illustrates the idea behind cascaded FWM.*

in Figure 1.8, where the sum of 7 different electrical fields centered around a central frequency ω_0 creates a pulse which can be described by:

$$E(z,t) = A(z,t)e^{i(\beta_0 z - \omega_0 t)} + c.c. \tag{1.3.26}$$

where A is a slowly varying envelope and β_0 and ω_0 are the propagation constant[4] and frequency of the pumping field.

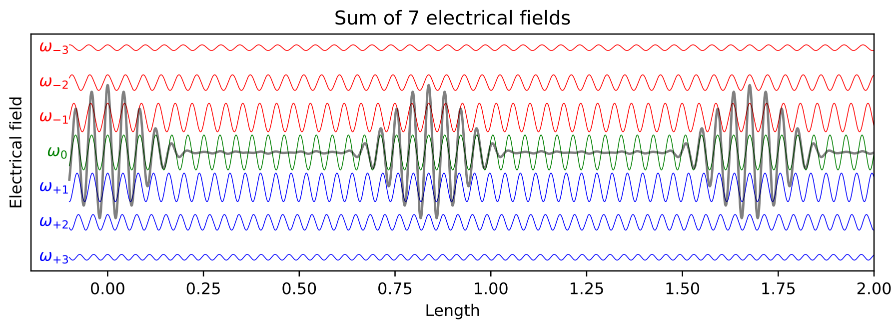

Figure 1.8: *Sum of 7 electrical fields (black) centered around ω_0 (green). The amplitudes of the 7 pulses are Gaussian distributed around the centre frequency.*

If such a pulse circulates inside a resonator it will couple out some of the light every time the pulse has completed a roundtrip. This leads to the formation of a pulse train with the spectral profile of a frequency comb.

Pulse propagation

A consequence of the CW approximation failing is that the differential equations we used to describe the evolution of the field are also no longer valid, as

[4] In other fields this is also known as the wavenumber, and typically uses the symbol k.

the electrical field amplitude E_i can no longer be assumed to only depend on propagation length z but also varies over time.

If we again start from the wave equation Equation 1.3.16, and now follow the derivation for pulse propagation in [53] and [52]. We also drop the n subscript on the fields as we assume the total field of a pulse is described by Equation 1.3.26 with a single frequency and a spatially and temporally varying amplitude envelope. We can then rewrite the nonlinear polarization as:

$$\mu_0 P^{NL}(z,t) = \mu_0 \epsilon_0 \frac{3}{4} \chi^{(3)} |E|^2 E \tag{1.3.27}$$

$$\mu_0 P^{NL}(z,t) = \frac{3}{4c^2} \chi^{(3)} |E|^2 E = \frac{1}{c^2} \epsilon_{NL} E, \tag{1.3.28}$$

where we have assumed that $\chi^{(3)}|E|^2$ varies much more slowly than the envelope. We then insert it into the wave equation and gather all the linear terms on the RHS:

$$\nabla^2 E(z,t) - \frac{\epsilon_r + \epsilon_{NL}}{c^2} \frac{\partial^2 E(z,t)}{\partial t^2} = 0 \tag{1.3.29}$$

We now insert Equation 1.3.26 and Fourier transform, as the time derivatives are easier to deal with in the frequency domain:

$$\nabla^2 E(z,\omega) + \frac{(\epsilon_r + \epsilon_{NL})\omega^2}{c^2} E(z,\omega) = 0 \tag{1.3.30}$$

$$\left(\frac{\partial^2}{\partial z^2} + 2i\beta_0 \frac{\partial}{\partial z} - \beta_0^2 + \beta^2 + \beta_{NL}^2 \right) A(z,\omega') e^{i\beta_0 z} = 0, \tag{1.3.31}$$

where we have used:

$$\beta^2 = \epsilon_r \frac{\omega^2}{c^2} \qquad \text{and} \qquad \beta_{NL}^2 = \epsilon_{NL} \frac{\omega^2}{c^2}, \tag{1.3.32}$$

and the Fourier transform:

$$\mathcal{F}[E(z,t)] = E(z,\omega) = A(z,\omega - \omega_0) = A(z,\omega') \tag{1.3.33}$$

We now factor out the exponential function, and use the slowly varying envelope approximation to remove the first term on the LHS:

$$2i\beta_0 \frac{\partial A(z,\omega')}{\partial z} - (\beta_0^2 - \beta^2 - \beta_{NL}^2) A(z,\omega') = 0 \tag{1.3.34}$$

β_0 is the propagation constant of the carrier electrical field. It can also be thought of as the linear, non-dispersive propagation constant. β is the dispersive propagation constant which changes with frequency, and β_{NL} is the nonlinear propagation constant.

Normally, $\beta + \beta_{NL}$ only differ slightly from β_0, so it is reasonable to approximate[52]:

$$(\beta_0^2 - \beta^2 - \beta_{NL}^2) \approx -2\beta_0(\beta + \beta_{NL} - \beta_0). \tag{1.3.35}$$

53. Agrawal, *Nonlinear Fiber Optics*(2001)
52. Boyd, *Nonlinear Optics - Third Edition*(2008)
52. Boyd, *Nonlinear Optics - Third Edition*(2008)

We can now insert this and cancel one of the β_0:

$$i\frac{\partial A(z,\omega')}{\partial z} + (\beta + \beta_{NL} - \beta_0)A(z,\omega') = 0 \tag{1.3.36}$$

The dispersive propagation constant is now Taylor expanded around ω':

$$\beta = \sum_{n=0}^{\infty} \frac{\beta_n}{n!}(\omega')^n \tag{1.3.37}$$

where the first term will cancel the last β_0 remaining:

$$i\frac{\partial A(z,\omega')}{\partial z} + \left(\sum_{n=1}^{\infty} \frac{\beta_n}{n!}(\omega')^n + \beta_{NL}\right) A(z,\omega') = 0. \tag{1.3.38}$$

We then rearrange and Fourier transform back to the time domain:

$$\frac{\partial A(z,t)}{\partial z} = i\sum_{n=1}^{\infty} i^n \frac{\beta_n}{n!}\frac{\partial^n}{\partial t^n} A(z,t) + i\beta_{NL}A(z,t) \tag{1.3.39}$$

We can now turn our attention to the nonlinear part and realize that it can be defined using the same nonlinear parameter γ we used earlier:

$$\beta_{NL} = \gamma |A|^2 \tag{1.3.40}$$

$$\frac{\partial A(z,t)}{\partial z} = i\sum_{n=1}^{\infty} i^n \frac{\beta_n}{n!}\frac{\partial^n}{\partial t^n} A(z,t) + i\gamma|A|^2 A(z,t) \tag{1.3.41}$$

It is typical to include up to the second order of the dispersion, so it takes the form:

$$\frac{\partial A(z,t)}{\partial z} = -\beta_1 \frac{\partial}{\partial t} A(z,t) - i\frac{\beta_2}{2}\frac{\partial^2}{\partial t^2} A(z,t) + i\gamma|A|^2 A(z,t). \tag{1.3.42}$$

β_1 and β_2 are related to two important physical parameters: The group velocity, i.e. the propagation velocity of the pulse envelope, and the group velocity dispersion, which describes how the pulse broadens.

It is common to change to a temporal reference frame that follows the pulse, thus moving with the group velocity:

$$\tau = t - \frac{z}{v_g} = t - \beta_1 z \tag{1.3.43}$$

$$\frac{\partial A}{\partial \tau} = \frac{\partial A}{\partial \tau}\frac{\partial \tau}{\partial \tau} + \frac{\partial A}{\partial z}\frac{\partial z}{\partial \tau} = \frac{\partial A}{\partial \tau} \tag{1.3.44}$$

$$\frac{\partial A}{\partial z} = \frac{\partial A}{\partial z}\frac{\partial z}{\partial z} + \frac{\partial A}{\partial \tau}\frac{\partial \tau}{\partial z} = \frac{\partial A}{\partial z} - \beta_1 \frac{\partial A}{\partial \tau} \tag{1.3.45}$$

Which leads to:

$$\frac{\partial A(z,\tau)}{\partial z} = i\sum_{n=2}^{\infty} i^n \frac{\beta_n}{n!}\frac{\partial^n}{\partial \tau^n} A(z,\tau) + i\gamma|A|^2 A(z,\tau) \tag{1.3.46}$$

$$\frac{\partial A(z,\tau)}{\partial z} \approx -i\frac{\beta_2}{2}\frac{\partial^2}{\partial \tau^2} A(z,t) + i\gamma|A|^2 A(z,\tau) \tag{1.3.47}$$

The difference between this equation and the differential ones we derived in the CW approximation is that this contains both spatial and temporal derivatives, which makes it more difficult to obtain analytical solutions.

The first term is the second order dispersion, which as shown above is the second order coefficient in the Taylor expansion of the propagation constant, directly proportional to the group velocity dispersion. In most common materials this is is positive, and also labelled as *normal*, however through material selection and waveguide geometry it can be engineered to be negative, or *anomalous*

This is illustrated on Figure 1.9 where a simulation of normal, none, and anomalous dispersion is shown. We see that after some time T the pulses have propagated a length in the dispersive medium, which has caused the high and low frequency components (illustrated by the blue and red electrical fields plotted offset for clarity from the combined pulse.)

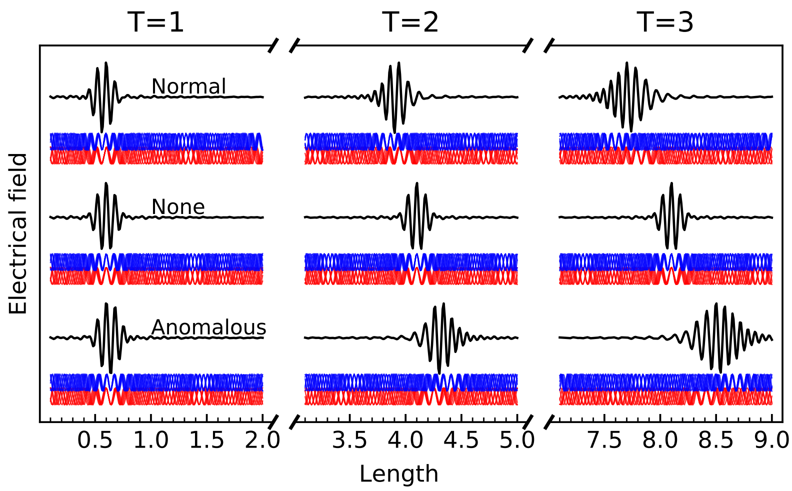

Figure 1.9: *Graphical illustration of the consequence of normal (top) none(mid) and anomalous (bottom) dispersion. The black fields are the sum of all the blue and red fields below them. The blue and red correspond to fields with higher and lower frequency than the carrier frequency and are offset for clarity. The resulting frequency chirps of the propagating pulse is due to the higher frequencies propagating with a different group velocity than the lower frequencies.*

The third and last term in the propagation equation represents the Kerr effect, or the intensity dependent refractive index. As the front and back of the pulse have two different intensity slopes, this will lead to the front of the pulse experiencing a downward shift in frequency and the back of the pulse experiencing an upshift in frequency.

In the anomalous dispersion regime these two effects can cancel each other for a specific pulse envelope shape. Such a pulse envelope is known as a bright soliton, as it will propagate indefinitely in the material without changing.

In the normal dispersion regime the only soliton solution are dark solitons where the pulse envelope can be modelled as an amplitude dip in a continuous wave. This changes the sign of the Kerr effect and thus can only exist in normal dispersion regimes.

Both types of solitons are highly interesting for us because we need to ensure that the pulse train produced by the circulating pulse does not change from round trip to round trip, thus requiring that the circulating pulse does not change when propagating.

Until now we have neglected absorption, however it can be modelled simply as a linear loss term α, and will be included in the propagation equations as:

$$\frac{\partial A(z,\tau)}{\partial z} = -\frac{\alpha}{2}A(z,\tau) + i\sum_{n=2}^{\infty} i^n \frac{\beta_n}{n!}\frac{\partial^n}{\partial \tau^n}A(z,\tau) + i\gamma|A|^2 A(z,\tau) \tag{1.3.48}$$

This means solitons, while not changing their temporal or spectral structure, will dissipate over time. They are therefore also called dissipative Kerr solitons by some authors.

In summary this means we need to fulfil two design criteria if we wish to use a MRR to generate a frequency comb from a CW input. Firstly the dispersion must be engineered to ensure phase matching and gain for the FWM processes which can compensate for the losses, and secondly the dispersion must be engineered to counteract the frequency chirp due to the intensity dependent refractive index, which will keep the pulse propagating unchanged as a soliton. This leads to a double balance which must be maintained in order to generate a dissipative Kerr soliton frequency comb neatly illustrated in Figure 1.10 (from [54])

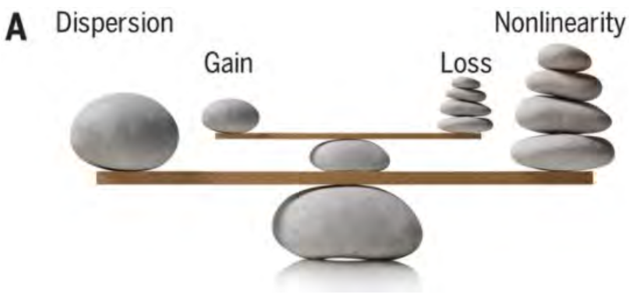

Figure 1.10: *Graphical illustration of the double balance between Dispersion and Kerr nonlinearity, and FWM gain and loss. Figure adapted from [54]*

Inside a resonator

The equations above for FWM gain and pulse propagation all assume one long continuous waveguide such as a fibre. In order to model the dynamics inside the MRR we need to include the boundary conditions related to a resonator. In a MRR that is pumped by a CW laser we assume that the pump continuously supplies power to the ring, and that the pulse must come back to its initial position after propagating one roundtrip in the MRR. This can be modelled using an infinite Ikeda map which imposes these boundary conditions on the propagation equation, and modifies it to our use case.

We will assume a MRR structure, were light circulates around a resonator with length L and reaches the input again after one roundtrip. The envelope

54. Kippenberg et al., "Dissipative Kerr Solitons in Optical Microresonators" (2018)

field after the mth roundtrip will be (from[34] but first shown by [55]):

$$A^{(m+1)}(0,\tau) = \sqrt{\theta}A_{in} + \sqrt{1-\theta}A^{(m)}(L,\tau)e^{i\beta_0 L} \tag{1.3.49}$$

where θ is the transmission coefficient and $\phi_0 = \beta_0 L$ is the accumulated phase by the intra-cavity electrical field after one roundtrip. If the accumulated phase is nonzero, it represents a small difference between the FSR, and the actual resonance spacing due to higher order dispersion effects. We will assume that the resonators have high finesse, i.e. low loss, such that $\theta \ll 1$. This also means that there will only be light in the cavity if the accumulated phase is very close to 2π. If we now assume that the input field is not necessarily on resonance with the cavity, we can define:

$$\delta_0 = 2\pi n - \phi_0 \tag{1.3.50}$$

which defines it as the phase difference from the nth cavity resonance. We can then approximate:

$$\sqrt{1-\theta} \approx 1 - \frac{\theta}{2}\dots \qquad \text{and} \qquad e^{i\delta_0} \approx 1 + i\delta_0 \dots \tag{1.3.51}$$

thus arriving at:

$$\sqrt{1-\theta}e^{i\delta_0} \approx 1 - \frac{\theta}{2} + i\delta_0, \tag{1.3.52}$$

where we have dropped the higher order terms. Using this we can rewrite the equation above:

$$A^{(m+1)}(0,\tau) = \sqrt{\theta}A_{in} + \left(1 - \frac{\theta}{2} + i\delta_0\right)A^{(m)}(L,\tau) \tag{1.3.53}$$

If we now look at the propagation equation, and try to estimate $A^{(m)}(L,\tau)$, we can do that with:

$$\left.\frac{\partial A^{(m)}(z,\tau)}{\partial z}\right|_{z=L} \approx \frac{A^{(m)}(L,\tau) - A^{(m)}(0,\tau)}{L} \tag{1.3.54}$$

$$\begin{aligned}\frac{A^{(m)}(L,\tau) - A^{(m)}(0,\tau)}{L} = &-\frac{\alpha}{2}A^{(m)}(0,\tau) \\ &+ i\sum_{n=2}^{\infty} i^n \frac{\beta_n}{n!}\frac{\partial^n}{\partial\tau^n}A(z,\tau) \\ &+ i\gamma|A^{(m)}|^2 A^{(m)}(0,\tau)\end{aligned} \tag{1.3.55}$$

We can then isolate $A^{(m)}(L,\tau)$ and insert in the equation above:

$$\begin{aligned}A^{(m+1)}(0,\tau) =& \sqrt{\theta}A_{in} - \left(\frac{\alpha L + \theta}{2} + i\delta_0\right)A^{(m)}(0,\tau) \\ &+ iL\sum_{n=2}^{\infty} i^n \frac{\beta_n}{n!}\frac{\partial^n}{\partial\tau^n}A(0,\tau) \\ &+ iL\gamma|A^{(m)}|^2 A^{(m)}(0,\tau) + A^{(m)}(0,\tau)\end{aligned} \tag{1.3.56}$$

34. Pasquazi et al., "Micro-Combs: A Novel Generation of Optical Sources"(2018)
55. Ikeda, "Multiple-Valued Stationary State and Its Instability of the Transmitted Light by a Ring Cavity System"(1979)

The last step is to again assume that the cavity buildup time will be much larger than a round trip time (t_R), and if can therefore change to a slow timescale t, which relates to the spatial variable z:

$$A^{(m)}(0,\tau) = A(mt_R,\tau) = A(t,\tau) \tag{1.3.57}$$

The derivative is then approximated as:

$$\frac{\partial A(mt_R,\tau)}{\partial t} \approx \frac{A^{(m+1)}(0,\tau) - A^{(m)}(0,\tau)}{t_R}, \tag{1.3.58}$$

and we can finally combine everything:

$$t_R \frac{\partial A}{\partial t} = \sqrt{\theta} A_{in} - \left(\frac{\alpha L + \theta}{2} + i\delta_0\right) A + iL \sum_{n=2}^{\infty} i^n \frac{\beta_n}{n!} \frac{\partial^n}{\partial \tau^n} A + iL\gamma |A|^2 A \tag{1.3.59}$$

This equation is also known as the Lugiato-Lefever[56] equation in the mean field limit, and has been investigated thoroughly for not only micro resonator but also fibre resonator applications. Later in this thesis we will look to simulate the generation of frequency combs in our devices, but we first have to characterize the MRR and extract the dispersion parameters needed for our simulation.

56. Lugiato et al., "From the Lugiato–Lefever Equation to Microresonator-Based Soliton Kerr Frequency Combs" (2018)

Chapter 2

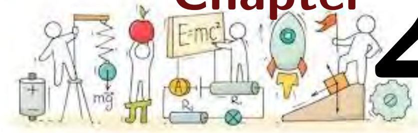

Microring resonator Kerr frequency combs

In order to accurately simulate and thus predict the behavior of a MRR we must characterize the basic properties of the device:

- Loss (α)
- Coupling coefficient (θ)
- Length (L)
- Higher order dispersion ($\sum_{n=2}^{\infty} i^n \frac{\beta_n}{n!}$)
- Nonlinear coefficient (γ)

Of which the last one is a material parameter which depends on the effective mode area of the electrical field. Based on finite element modelling we estimate it to $\gamma = 1$, and focus our attention on the remaining parameters. The remaining parameters can be extracted with a a single setup which records the transmission of the chip as the probe laser is scanned over the resonances, also referred to as modes. As mentioned earlier dispersion describes the wavelength dependent refractive index and how it causes light at different frequencies to propagate with different velocities inside a material. In a dispersion free material every resonance, or mode, would lie exactly $\frac{c}{nL}$ apart with n being the refractive index and c and L the speed of the light and the length respectively. When dispersion is taken into account, the change in refractive index makes the distance between two resonances (the FSR) wavelength dependent. We can therefore measure the dispersion by carefully mapping out the frequency spacing between each pair of resonances. This is commonly done by sweeping a widely tunable laser across the resonances and recording the transmission dips on an oscilloscope.

2.1 Characterizing the dispersion of a microring resonator

In order to accurately map out the higher order dispersion terms we must record the frequency of the resonances across several tens of nm, which most widely tunable lasers struggle to do continuously. We use a Toptica CTL (continuously tunable lase) which uses a combination of piezo scanning and micromotor adjustments in order to achieve mode-hop free tuning over a hundred nm range.

The downside is that the scanning speed is not guaranteed to stay constant throughout the scan. As we are trying to measure the frequency spacing of the MRR resonances, we need to calibrate the transmission scan to account for any variations in scan speed. This can be done by simultaneously sweeping a secondary frequency reference such as a resonator with a known frequency spacing and use it as a "frequency ruler" as illustrated on Figure 2.1. As long as the frequency spacing of the secondary resonator is small enough to assume a linear scan speed inbetween, we can convert our measured time trace to a frequency trace.

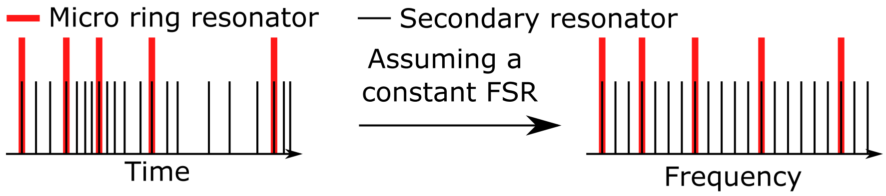

Figure 2.1: *Illustration of the calibration procedure using a secondary cavity as a frequency ruler to measure the frequency spacing of a MRR.*

The most widely used secondary resonators are fiber loop cavities, fiber interferometers, or frequency combs. With the latter being orders of magnitude more expensive and complex than the two former. The advantage of fiber based secondary resonators are that they are compact while still being long enough to have a reference point spacing on the order of hundreds of MHz which works well for MRR as their resonance spacing is typically in the 20 GHz to 200 GHz. Fiber resonators are also easy to work with and require little to no day to day alignment. They all, with exception of fiber based frequency combs, come with one large caveat; By guiding light in a material, they themselves suffer from dispersion, which changes the frequency spacing of the reference points and thus negating the idea of having a secondary resonator. One way of preventing this is to calibrate the fiber resonator, which can either be done by knowing the dispersion of the fiber beforehand, or by using another frequency comb to calibrate it.

Calibration using the free space cavity

As an alternative to a calibrated fiber cavity/interferometer, we have designed and implemented a free space cavity reference, as shown on Figure 2.2.

It is a simple Fabry-Perot etalon constructed with two 99.7% reflectivity concave mirrors with a radius of curvature R of 2 meters. While there still will be dispersion effects in the mirrors, their thickness is only a fraction of the overall cavity length, and can largely be ignored. We use a 1480 mm long aluminum profile as a cavity spacer between the two mirrors, with mirrormounts attached at an adjustable distance from the end.

The long spacer gives a FSR of ≈ 100 MHz while the large radius of curvature ensures a stable cavity geometry. The 99.7% reflectivity predicts a finesse of roughly ≈ 1000, and a linewidth of ≈ 100 kHz. As we will be scanning the laser at 10 nm/s ≈ 1.2 THz/s, this will scan over a reference cavity resonance in 83 ns. Our oscilloscope can store 20 million datapoints per channel with a

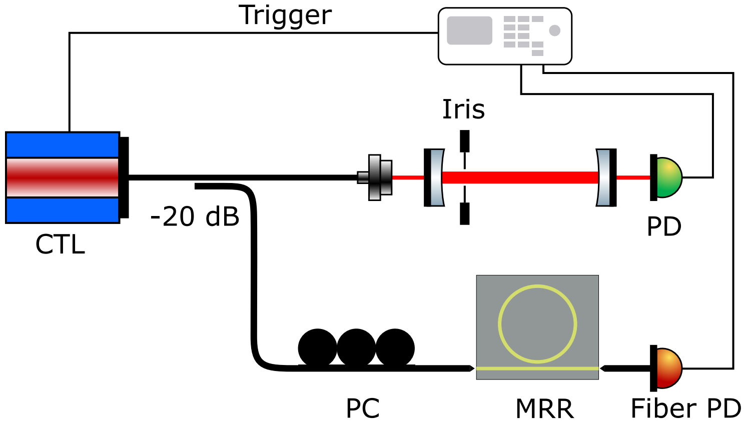

Figure 2.2: *Schematic setup of the dispersion measurement. We use a -20 dB coupler to split light between the free space cavity and the MRR. A polarization controller (PC) is used to control the polarization. Photo diodes (PDs) record the transmission of both resonators. The laser is a continuously tunable Toptica laser.*

sample rate of 1.66 MHz, or an equivalent sampling time of 600 ns. As this is about 10 times slower than desired, we will need to reduce the finesse, which can easily be done by introducing loss inside the cavity. In order to do this systematically we place an iris inside the cavity, which we can open or close to adjust the losses. Introducing losses this way also minimizes the higher order transversal modes, as they have a larger distribution of intensity off-center and thus experience a greater loss compared to the fundamental mode. This has the added benefit of reducing the alignment precision needed to get a useful signal from the cavity. In order to use the free space cavity to calibrate the dispersion measurement of the MRR, we split the scanning laser in two parts and record the transmission through both the MRR and the free space cavity simultaneously as shown on Figure 2.2. A sample of such a recording can be seen in Figure 2.3, which shows a small part of the free space cavity transmission scan. The zoomed inset shows that we are at the limit of laser scan speed, as we only have a handfull of points making out the cavity resonance. The lineshape is also not Lorentzian as one might expect, so we will simply use the location of the peak maximum as an estimate of the center of the resonace. This will add a small error which will average out over the 130000 recorded resonances found in a typical trace. The small peak next to the main feature is a higher order mode which can be removed during the data analysis.

The actual FSR of the free space cavity, determined using electro optical modulator (EOM) generated sidebands, was measured to be (96.50 ± 0.01) MHz. This is slightly less than predicted due to the mirrors being mounted a short distance away from the edges of the aluminum profile. By assuming this fixed FSR between each free space cavity resonance we can calculate the actual laser scan rate between each resonance, and thereby convert the time scan signal to a frequency scan signal. The histogram in Figure 2.3 shows the scan rate calculated between each cavity resonace. For this data the laser scan speed was set to 10 nm/s, which corresponds to 1.2 THz/s and is the center point of the histogram. It is important to measure the FSR as accurately as the linewidth

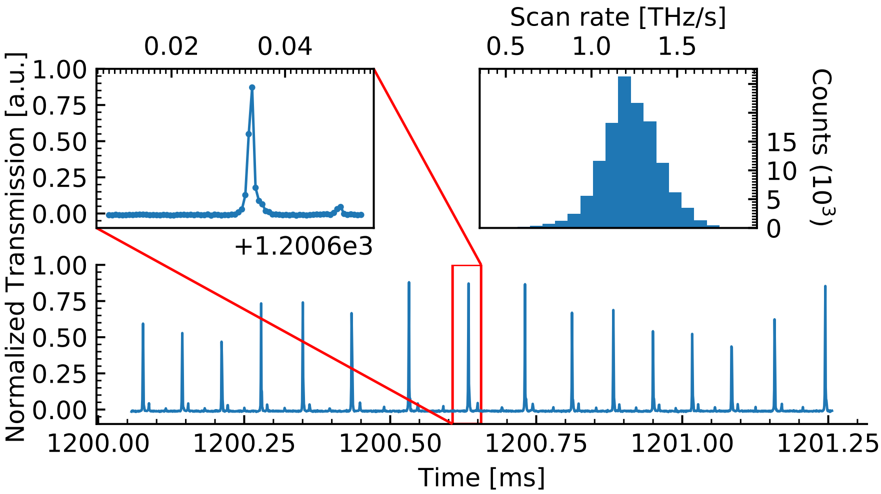

Figure 2.3: *Part of the recorded transmission through the free space reference cavity. The histogram shows the distibution of calculated laser scan speeds between each cavity resonance, assuming a FSR of* 96.7 MHz.

allows for, as this uncertainty will accumulate linearly with the number of free space cavity resonances recorded.

Our setup does not contain an absolute reference, and we instead use an electronic trigger signal emitted by the scanning laser when it passes 1525 nm and use this signal to fix the absolute value of our frequency axis. To prevent this one cound add a third element to the setup which could act as an absolute frequency reference. This is typically either a reference laser, or a gas cell where the absorption lines can be mapped and refered to the absolute definitions from International Bureau of Weights and Measurements (Bureau international des poids et mesures) (BIPM). While our method does include some uncertainty by not having such a reference, it is important to note that this uncertainty will have less influence than a nonlinear scanning speed. The former leads to an offset of the dispersion calculation while the scan speed error compounds over the entire scan time and makes it impossible to measure the dispersion.

Estimating the MRR properties

With the data from the secondary resonator we can convert the transmission trace of the MRR from time to frequency. This is shown in Figure 2.4 where we scan from 1525 nm to 1615 nm. We fit all the transmission dips with Lorentzian lineshapes in order to extract the full width half maximum (FWHM)[5].

$$T = A\frac{\left(\frac{1}{2}\Gamma\right)^2}{\left(\omega_0-\omega\right)^2+\left(\frac{1}{2}\Gamma\right)^2} + B, \tag{2.1.1}$$

[5] Sometimes called Full width half dip due to the nature of an absorption based signal

where A is the amplitude of the dip, ω_0 is the center angular frequency, γ is the FWHM, and B is the background offset level. One of the fits is shown in the top left inset of Figure 2.4.

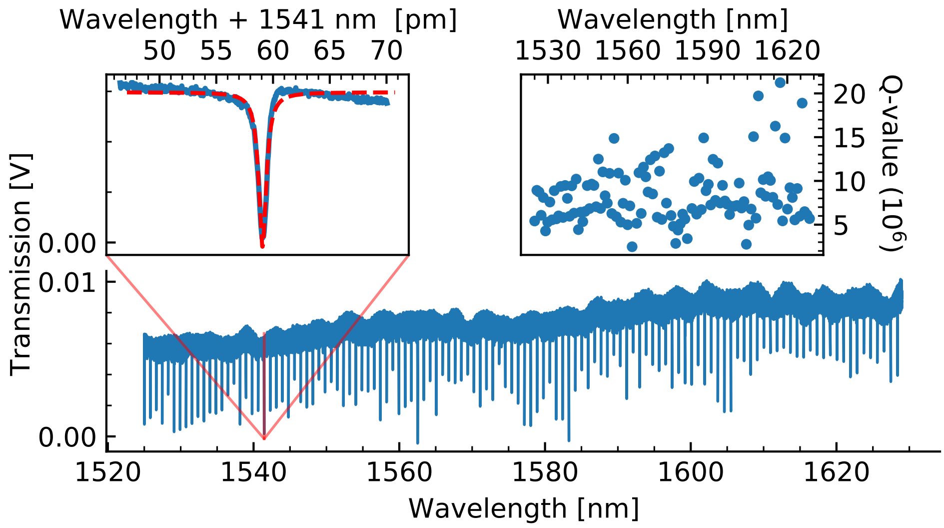

Figure 2.4: *Transmission scan of the microring resonator device. Top left inset is a zoom in of a single resonance, or mode. Dashed line is a Lorentzian fit. Top right inset shows the intrinsic Q-values calculated from the linewidts of the chip resonances.*

From the linewidth we can estimate the total Q-value:

$$Q_{tot} = \frac{\omega_0}{\gamma}, \tag{2.1.2}$$

which is related to the extrinsic and intrinsic Q, also known as coupling and resonator Q respectively:

$$\frac{1}{Q_{tot}} = \frac{1}{Q_{int}} + \frac{1}{Q_{ext}}. \tag{2.1.3}$$

The intrinsic Q relates to the internal losses of the resonator and depends on fabrication imperfections like rough sidewalls, or two photon absorption. The extrinsic Q depends on the coupling between the bus waveguide and the ring resonator. This is primarily influenced by the design of the device such as the gap distance between the ring and the waveguide. The device is over-coupled according to the manufacturers[50], which means $Q_{int} > Q_{ext}$. With this information we can calculate Q_i from the fitted fractional transmission amplitude[57]:

$$Q_{int} = \frac{2Q_{tot}}{1 - \sqrt{\tilde{A}}} \tag{2.1.4}$$

50. Ye et al., "High-Q Si 3 N 4 Microresonators Based on a Subtractive Processing for Kerr Nonlinear Optics" (2019)
57. Barclay et al., "Nonlinear Response of Silicon Photonic Crystal Micresonators Excited via an Integrated Waveguide and Fiber Taper" (2005)

where $\tilde{A}$ is the fractional transmission dip. The measured Q-values for all the resonances are shown in Figure 2.4, and show an average intrinsic Q-value of 7×10^6 in agreement with [50].

In order to estimate the length and the higher order dispersion we will start by picking a resonance, and describing the frequency position of the other resonances by a Taylor expansion:

$$\omega_\mu = \omega_0 + D_1\mu + \frac{1}{2}D_2\mu^2 + \frac{1}{6}D_3\mu^3 \dots \tag{2.1.5}$$

$$\tag{2.1.6}$$

where ω_0 is the frequency of the resonance of interest, μ the integer number of resonances away from the resonance of interest. It is positive for higher frequency resonances and negative for lower frequency resonances. These coefficients can be related to the propagaton constant β described in the previous section, which we also Taylor expanded (see Equation 1.3.37) [34]:

$$D_n \approx -\frac{1}{\beta_1} D_1^n \beta_n, \tag{2.1.7}$$

which is exact up to D_2. In a nondispersive material the frequency of the μth resonance would be perfectly described by $\omega_0 + D_1\mu$, as D_1 represents the FSR.

We now convert the measured resonances in Figure 2.4 to frequency through:

$$\omega = \frac{2\pi c}{\lambda}$$

and fit with the Taylor expansion to third order to extract the dispersion parameters. This is shown on Figure 2.5 where we have Taylor expanded around

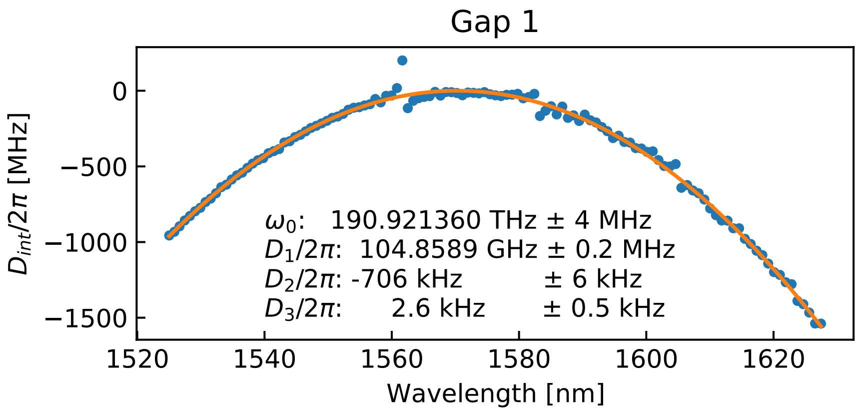

Figure 2.5: *Integrated dispersion of the MRR. Solid line is a third order polynomial fit, with the linear part subtracted. Printed values are the fit parameters in units of frequency.*

50. Ye et al., "High-Q Si 3 N 4 Microresonators Based on a Subtractive Processing for Kerr Nonlinear Optics" (2019)
34. Pasquazi et al., "Micro-Combs: A Novel Generation of Optical Sources" (2018)

the resonance at 1570 nm, and subtracted the linear part ($\omega_0 + D_1\mu$) in order to plot what is called the integrated dispersion:

$$D_{\text{int}} = \omega_\mu - \omega_0 - D_1\mu \approx \frac{1}{2}D_2\mu^2 + \frac{1}{6}D_3\mu^3, \tag{2.1.8}$$

This is done because D_1 is orders of magnitude larger than D_2 and D_3. We choose to plot it as a function of wavelength, however the data analysis is carried out after converting to angular frequency ω. This is because wavelengths are more easily understood visually, while the convention in the community is to calculate $D_{1,2,3}$ in units of frequency. The data points on Figure 2.5 represents the un-truncated higher order dispersion, while the solid line fit represent the Taylor expansion of the dispersion truncated at third order (D_2 and D_3). From the plot we see that the focus of the parabola is negative, i.e. D_2 is negative. This means the second order propagation constant β_2 is positive showing that the material has normal dispersion as explained in the previous section:

$$\beta_2 = 68.1\,\text{ps}^2/\text{km} \pm 0.6\,\text{ps}^2/\text{km} \tag{2.1.9}$$

Our measured values agree with those measured on a similar chip at Chalmers [58].

Evaluation of the free space cavity

Because the free space cavity is comparable to the arm span of an average person, it is impractical to align, and it is therefore interesting to investigate if the length of the cavity can be changed without compromizing the dispersion measurements. To do this we artificially reduce the length of the free space cavity by only including every Nth cavity resonance (mode) in the data analysis, as illustrated in Figure 2.6.

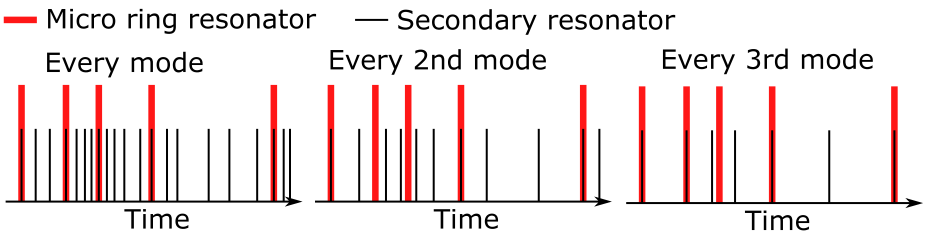

Figure 2.6: *Illustration of only using every 2nd or 3rd secondary resonator mode for the calibration procedure. This mimics the effect of having a smaller free space cavity with a larger FSR.*

This puts a larger requirement on the linearity of the laser scan but reduces the required length of the cavity by a factor of N. Figure 2.7 shows the result of using all, every 10th, every 50th and every 150th resonance. The fitted parameters $D_{1,2,3}$ are summarized in Table 2.1 where we can see that D_1 is hardly affected by using fewer modes, whereas D_2 and D_3 stay consistent up to using as few as every 50th mode. This means we could have obtained the same results for the higher order dispersion with a cavity that was just under

58. Yu et al., "Tuning Kerr-Soliton Frequency Combs to Atomic Resonances" (2019)

3 cm long. This does however rely on the linearity of the scanning laser, which means a longer cavity can make up for a laser with a less linear scan. The biggest advantage of using a long cavity is that it increases our ability to see the effect of the mode interactions, which for our purpose is important.

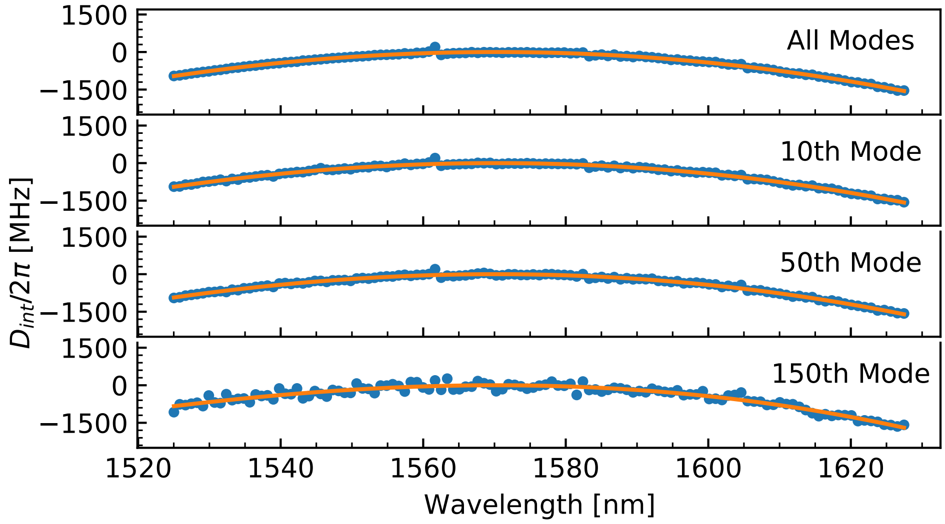

Figure 2.7: *The resulting integrated dispersion if fewer modes of the free space cavity are used. The datapoints are the integrated dispersion similar to Figure 2.5.*

	$D1/2\pi$ GHz	$\sigma_{D1}/2\pi$ MHz	$D2/2\pi$ kHz	$\sigma_{D2}/2\pi$ kHz	$D3/2\pi$ kHz	$\sigma_{D3}/2\pi$ kHz	β_2 ps^2/km	σ_{β_2} ps^2/km
All	104.86	0.21	-706	6	2.6	0.5	68.1	0.6
10th	104.86	0.26	-704	8	3.0	0.7	68.0	0.7
50th	104.86	0.28	-704	8	3.6	0.7	68.0	0.8
150th	104.85	0.8	-689	24	6.5	2.1	66.6	2.3

Table 2.1: *Table of the extrated dispersion related parameters from the data in Figure 2.7.*

In conclusion, the free space cavity is able to act as a state of the art, dispersion free frequency reference for dispersion measurements. It is inexpensive and easy to setup, and requires little to no alignment in day to day use. Because it is dispersion free by design, it does not rely on either expensive frequency comb calibrations, or trust in manufacturer dispersion specifications. Furthermore, the cavity reference has shown potential for improvement by including higher order modes. This was shown by [59], where the first 4 higher order transversal modes were allowed to propagate in the cavity by opening the iris inside the cavity. In this way the number of frequency markers can be increased by at least a factor of 4, without increasing the length of the cavity. The free space

59. Nielsen, "Behaviour of Picosecond and Femtosecond Pulses in SiO 2 / Si 3 N 4 Microring Resonator Filters" (2020)

cavity design has been used succesfully to measure both our S_3N_4 devices, but also high confinement microring resonators in 4H-silicon carbide[60].

60. Zheng et al., "Fabrication of High-Q, High-Confinement 4H-SiC Microring Resonators by Surface Roughness Reduction"(2019)

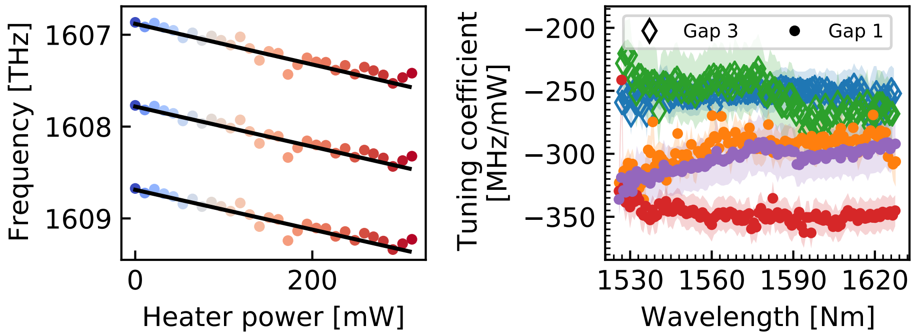

Figure 2.8: *Example of linear fit to the mode shifts as a function of heating power (left). Fitted slopes for each resonance, for two different devices (Gap1 and Gap3) measured several times across different days (right). Shaded area indicates 1σ confidence interval of the linear fits.*

2.2 Thermal tuning of the dispersion

On Figure 2.5 we see three wavelenth areas (1560 nm, 1580 nm, and 1610 nm) where the dispersion differs significantly from the fit. These deviations are due to interactions between the fundamental resonance, and another higher order resonance, which occurs when the frequencies of the two resonances coincide. These interactions strongly shifts the dispersion locally and are important for the generation of dissipative Kerr frequency combs. While a normal dispersion can support the propagation of dark pulses, we also need FWM gain, or optical parametric oscillation, in order to excite them and convert our CW pump laser to a pulse. Here the mode interactions change the dispersion enough to provide the necessary phase shift to fulfill the phase matching condition[38],[61],[62]. As explained in the supplementary material of [63], the Kerr nonlinearity causes the optical power to shift the resonances due to crossphase modulation. On the integrated dispersion plot this is represented by the resonances shifting downwards. As the curvature of the integrated dispersion plot is negative for normal dispersion, these two effects work in the same direction and prevent phase matching of FWM. If a mode interaction now moves the resonances upwards, then this can compensate for the Kerr nonlinearity and allow FWM at those resonances.

By sweeping the probe laser over 100 nm while recording the transmission, at different applied heating powers, we can investigate how the dispersion is affected by thermal effects. As expected, all the resonances shift linearly as shown from Figure 2.8 where we have plotted the frequencies of three of the resonances, for 30 different heater powers. The black line in a linear fit we can use to extract the thermal tuning coefficient for our microheater. If we do this for all resonances and 5 different devices, we get the plot on the right of Figure 2.8, which shows that the thermal tuning coefficient varies between

38. Liu et al., "Investigation of Mode Interaction in Optical Microresonators for Kerr Frequency Comb Generation" (2014)
61. Savchenkov et al., "Kerr Frequency Comb Generation in Overmoded Resonators" (2012)
62. Xue et al., "Mode-Locked Dark Pulse Kerr Combs in Normal-Dispersion Microresonators" (2015)
63. Yu et al., "A Continuum of Bright and Dark-Pulse States in a Photonic-Crystal Resonator" (2022)

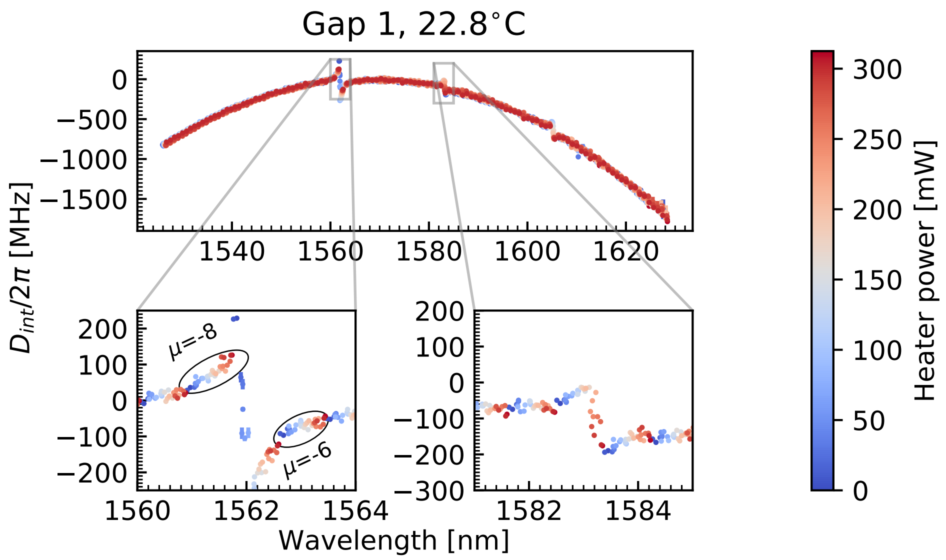

Figure 2.9: *Integrated dispersion for Gap 1 for different heater powers. The chip base temperature is set to 22.8 °C. One group of points, from blue to red, illustrate the frequency shift a mode makes, as the heater power is increased. Modes μ =-8 and μ =-6 are circled in the lower left plot.*

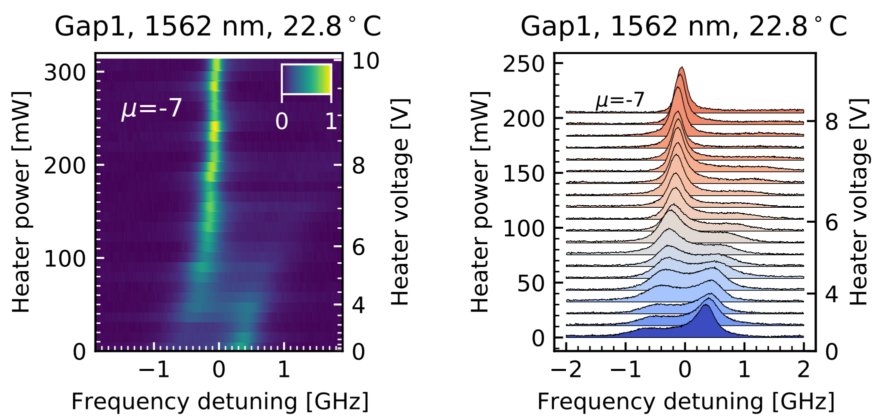

Figure 2.10: *Normalized and inverted transmission from the $\mu = -7$ mode with a chip base temperature of 22.8 °C. Right plot is a stacked spectrum, and left plot is a false colour plot of the same data.*

−300 MHz/mW and −250 MHz/mW. The shaded area indicates 1σ confidence interval of the linear fit and while this is large, this method does give a good indication of the order of magnitude of the thermal tuning coefficient.

Because all resonances shift linearly, we do not expect the dispersion to change when heating power is applied. However, if we measure and calculate the integrated dispersion at several different applied heating powers we see that it strongly influences the avoided mode crossings. This is shown on Figure 2.9, where the base temperature was set to 22.8 °C. The vertical lines are errorbars that correspond to the standard deviation of 5 measurements.

The insets show the points of interest around the avoided mode crossings. Each group of points (blue to red) show the frequency shift of one particular resonance, as highlighted by the two circles in the lower right zoom in. The total shift over 300 mW of heating power is just a little smaller than the resonance spacing (≈ 105 GHz). As the heating power is increased, the modes around the modecrossing get displaced many orders of magnitude more than the modes further away from the interaction point. Remembering that the integrated dispersion represents the deviation from a perfectly equidistant frequency spacing, this indicates that the stronly interacting modes (μ =-8) changes from shifting towards μ =-7 at lower powers, to shifting towards μ =-9 at higher powers. While the shift is very visible on the integrated dispersion plot, it is still only on the orders of hundres of MHz, or less than 1 % of the FSR. The behavior can additionally be tuned by adjusting the base temperature, as this will simply offset the temperature tuning.

The avoided mode crossings appear when the fundamental TE mode can interact with other modes. This typically happens due to fabrication imperfections in the waveguide, which allows scattering from the guided mode, to other modes. If the fundamental mode is frequency degenerate with the other modes it interacts with, they will create an avoided mode crossing. In this area, the two modes are no longer a good basis for describing the mode state of the waveguide. Instead we have to go to a coupled mode bases, which consists of two orthogonal modes, each superpositions of the two original modes. These are also sometimes called *supermodes* or *dressed states* in other types of systems. The two supermodes will be symmetrically split around the frequency of the original mode, with a splitting which depends on the strength of the interaction, and the detuning between the two modes.

We can tune the detuning between the two modes because they have two different thermal tuning characteristics. Both modes will shift with temperature, but not by the same amount, thus changing the relative detuning between them. This is evident if we look closely at the resonace involved in the avoided mode crossing around 1561 nm shown on Figure 2.10.

The plots show the transmission dip that has been inverted and normalized to for clarity. The left plot is a false colour plot of the transmission and the right plot is a stacked spectrum plot displaying the same data. For each heating power, the overall thermal shift has been removed, in order to better observe the effect of the avoided mode crossing. Looking at the lower part of the right plot we see the fundamental TE resonance around 0.5 GHz, with the other, higher order mode around −0.8 GHz. As the heating power is increased to 50 mW the detuning between the two modes is decreased. This increases the mode interaction and creates a doublet, i.e. a double peak structure. When the heating power is further increased the detuning starts to increase again

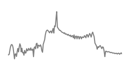

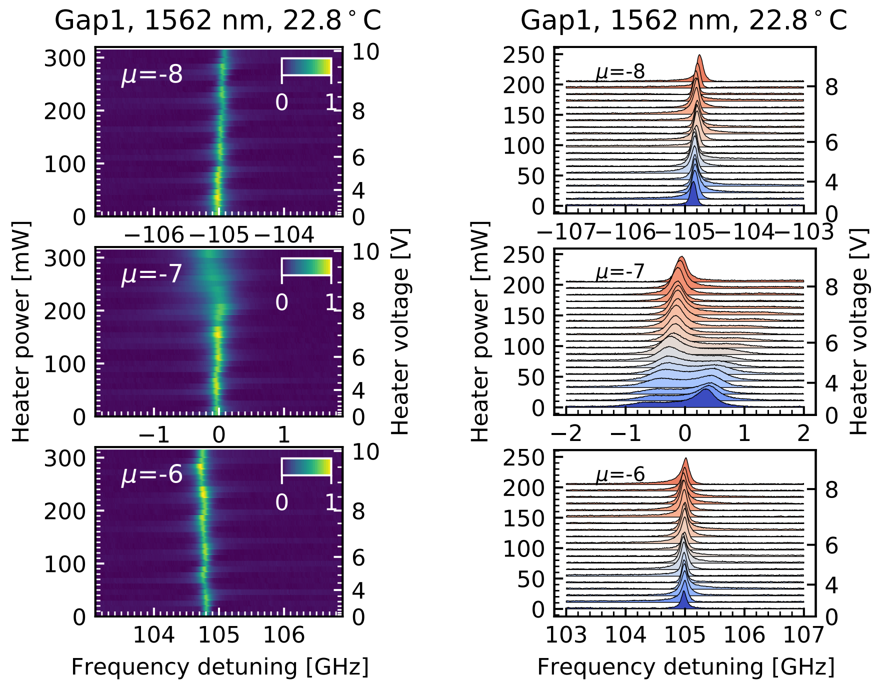

Figure 2.11: *Normalized and inverted transmission plots from the μ =-8,μ =-7 and μ =-6 modes around* 1562 nm*. Middle row shows an avoided mode crossing between two modes while top and bottom row only show the fundamental mode. Middle row is identical to Figure 2.10.*

and the fundamental resonance shows up on the other side of the higher order mode.

The effect of the mode interaction is becomes very visible if we look at the three modes surrounding the mode interaction. This is depicted in Figure 2.11 where the top and bottom row of plots (labelled (μ =-7 & μ =-9) show only a single mode across the heater power tuning. The middle row shows the same figures as displayed in Figure 2.10. By tracing the peaks of the two interacting modes at $\mu = -7$ we can investigate how the mode interaction changes if we change the base temperature of the chip. This is shown on Figure 2.12, where we see that changing the base temperature can change the point where the mode interaction causes a splitting, but cannot change the size of the splitting. This is because the thermal tuning only changes the detuning between the two interacting modes and not the interaction strength.

The mode interactions in these devices are not designed, but rather a product of fabrication imperfections and they will therefore vary between different devices, even with the same fabricated geometry. This can be seen on Figure 2.13, where the integrated dispersions at a range of heater powers, for two different devices, are plottet. Some of the mode interactions appear at the same positions (1562 nm and 1582 nm), whereas some are shifted (1600 nm), and some only exist in one of the devices (1541 nm).

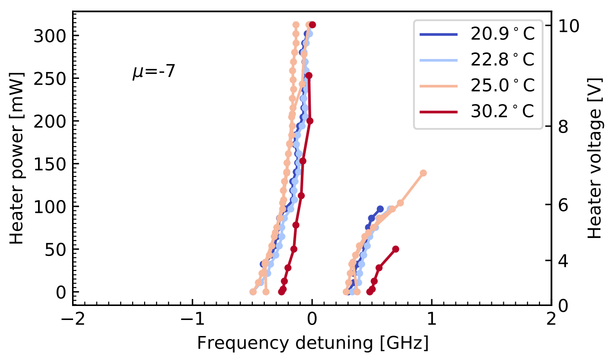

Figure 2.12: *Plot of the transmission dips in the avoided mode crossing, for different base temperatures. Below 30 °C the splitting does not increase by lowering the base temperature further.*

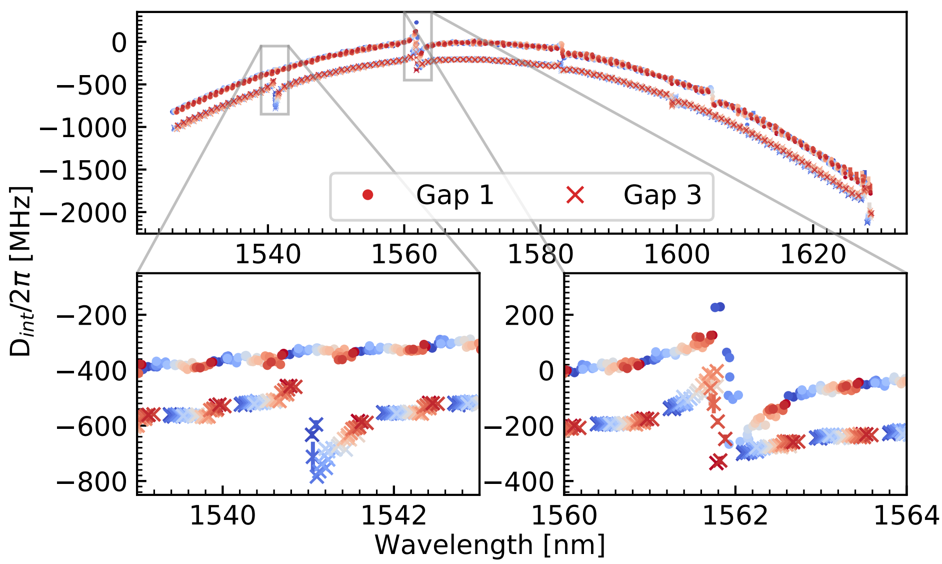

Figure 2.13: *Measured integrated dispersion at different heater powers for two different devices with identical fabrication dimensions. The mode interactions are not equally strong or similarly placed between the two devices. The data labelled Gap 3, as been offset by −200 MHz for visibility.*

All the dispersions presented so far have been evaluated around an arbitrarily chosen resonance around 1570 nm. If we instead look at the integrated dispersion around the mode interaction we get Figure 2.14. For FWM gain the dispersion of interest is always from the pumped mode, i.e. the phase shift the other resonances have compared to the pumped resonance. Here it is clear to see that from the perspective of the pumped mode the mode interaction is shifting all the other modes. When the optical power now shifts the resonances downwards due to the Kerr effect, the net phase shift will be zero and the the FWM process will be possible. The overall shape of the integrated dispersion still curves downwards and therefore shows normal dispersion, which will allow a dark soliton pulse to propagate. Because we have now measured the dispersion at a range of different heater powers, we can use this to simulate comb generation using micro heaters. This will be explained in the following section.

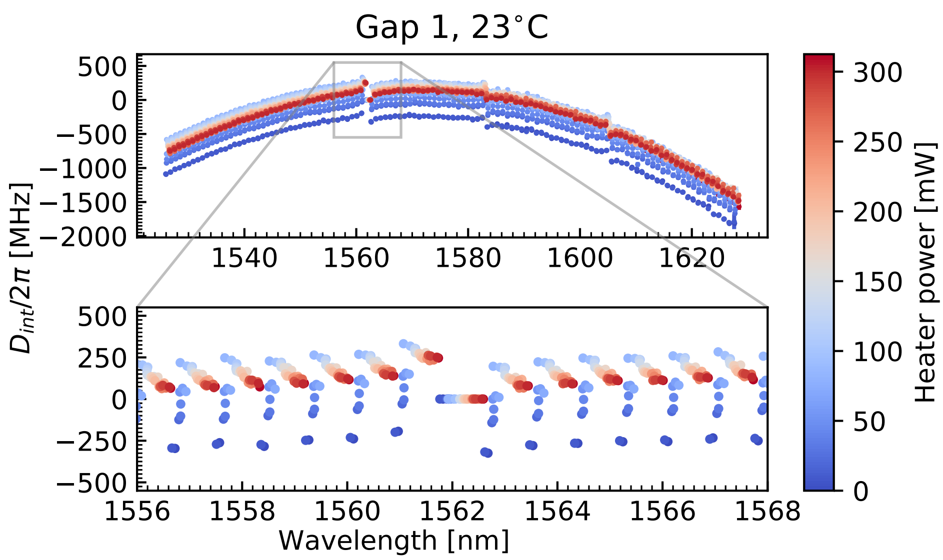

Figure 2.14: *Integrated dispersion calculated around the resonance which experiences the strong mode interaction around* 1562 nm*.*

2.3 Simulating micro ring resonators

In the first chapter we derived an equation which governs the evolution of light inside a MRR(Equation 1.3.59). We will now use this equation to simulate the behaviour of bright and dark soliton Kerr combs, using the dispersion data extracted from measurements described in the previous section. Simulating the dynamical behaviour of these resonators is interesting because we can infer information about the electrical field inside the resonator, which is impossible to measure in practice.

The split step Fourier method

To solve Equation 1.3.59 we use the split step Fourier method. It is described in [53], but we will briefly go through the main points here. We start by quickly splitting the terms in Equation 1.3.59 into the linear and nonlinear parts, referring to the physical effects which gave rise to them:

$$t_R\frac{\partial A}{\partial t} = \overbrace{\sqrt{\theta}A_{in} - \left(\frac{\alpha L+\theta}{2}+i\delta_0\right)A + iL\sum_{n=2}^{\infty} i^n\frac{\beta_n}{n!}\frac{\partial^n}{\partial\tau^n}A}^{\text{linear}} + \overbrace{iL\gamma|A|^2A}^{\text{nonlinear}} \tag{2.3.1}$$

Instead of solving the full equation, we will solve the linear and nonlinear parts independently, by assuming that over small enough step sizes they act independently. This effectively splits the propagation into two steps, first propagating the linear part of the equation, followed by the nonlinear part. In most real world applications the accuracy is typically improved by utilizing a symmetrized split step method, where three steps are used instead of two. In this way we first propagate half a step of the linear part, then the nonlinear part, and then another half of the linear part.

Here we will rely on the pyLLE package[64] to perform the numerical simulations, though with a few choice modifications to the code. Similar to our derivation of the Lugiato-Lefever equation (LLE), the authors of the pyLLE package do not truncate the higher order dispersion at second order, but instead rely on the integrated dispersion D_{int}. The package then simulates the LLE across many modes in the frequency domain by solving:

$$\begin{aligned} t_R\frac{\partial E(t,\tau)}{\partial t} = &-\left(\frac{\alpha'}{2}-i\delta_0\right)E + i\text{FT}^{-1}\left[-t_R D_{int}(\omega)\cdot\text{FT}[E(t,\tau)]\right] \\ &+\gamma L|E|^2E+\sqrt{\theta}E_{in}, \end{aligned} \tag{2.3.2}$$

which is identical to our own equation above, if we collect $\alpha L + \theta = \alpha'$ which represents the total loss in a round trip. In order to seed the FWM process, random quantum noise is added to every resonator mode at each roundtrip, and it is this noise which grows into new frequency components if the phase matching condition is fulfilled.

As mentioned earlier, the generation of soliton combs is goverend by three important nonlinear effects; Four-wave mixing, cross-phase modulation, and self-phase modulation. All these are controlled by only tree parameters; The

53. Agrawal, *Nonlinear Fiber Optics*(2001)
64. Moille et al., "Pylle: A Fast and User Friendly Lugiato-Lefever Equation Solver"(2019)

detuning between the pump laser and the pumped resonance, the pump power, and the dispersion, with the latter typically being fixed at the fabriaction time of the device. We will therefore use the measured dispersion and simulate sweeping the detuning of the pump laser at a fixed pump power.

Bright Solitons

We start with validating our model by simulating the generation of bright solitons. Here the dispersion is adequetly described with a second order polynomial, with the integrated dispersion measured by a student in our lab [59] to:

$$D_1 = 103\,\text{GHz} \tag{2.3.3}$$

$$D_2 = 616\,\text{kHz} \tag{2.3.4}$$

$$D_3 = -0.3\,\text{kHz} \tag{2.3.5}$$

$$\beta_2 = -65\,\text{ps}^2/\text{km} \tag{2.3.6}$$

Here we also measured an average intrinsic Q-value of 10×10^6, and we approximate the nonlinear parameter γ as 1 based on an effective mode area of $0.7\,\mu\text{m}^2$[65]. With these numbers, and the pyLLE package, we are now able to simulate bright soliton generation. We choose a pump power of 200 mW and sweep the pump detuning lineary from 0.8 GHz to −20 GHz during the simulation. The result is shown on Figure 2.15 where a) shows the comb power as a function of detuning, i.e. the combined power in all the generated comb lines. b) shows a false color plot of the power (in dB) at each wavelength, for each detuning, and c) shows the amplitude of the electrical field inside the microring resonator for each point in fast time, i.e. at each point inside the ring. d)-f) show the full comb spectra at different detunings.

We see that as the detuning is swept from positive (blue detuned), to negative (red detuned), light will couple into the MRR and the FWM process becomes phase matched and starts to generate a lot of new frequency components (Figure 2.15 f)). In the beginning these are just a few strong lines sometimes referred to as primary comb lines[54]. These are typically spaced multiple FSR away from the pump (Figure 2.15 f). These primary lines will in turn, through four-wave mixing, produce subcombs, which at some point the subcombs will start to overlap. This will create a structure which looks very similar to a comb when viewed on a spectrum analyzer but is actually a chaotic state where comblines from different subcombs co-exist within the same resonator mode, but not at exactly the same frequency. This will cause strong beatnotes at very low frequencies (≤ 1 GHz). The name chaotic refers to the temporal structure which changes constantly, thus creating low frequency noise. If the detuning is further decreased, we enter a regime where the chaotic state is no longer sustainable. Instead the pulses will transform into solitons, pulses which do not change amplitude or shape during propagation (Figure 2.15 e). Once stable solitons have been achieved the comb lines will be phase-locked to each other and represent a true frequency comb. The soliton state can consist

59. Nielsen, "Behaviour of Picosecond and Femtosecond Pulses in SiO 2 / Si 3 N 4 Microring Resonator Filters" (2020)
65. Ye, "Ultralow-Loss Silicon Nitride Waveguides for Nonlinear Optics" (2021)
54. Kippenberg et al., "Dissipative Kerr Solitons in Optical Microresonators" (2018)

of one or several soliton pulses, distinctively different from the chaotic modulation instability state because the temporal structure, i.e. the angle between the solitons in the micro resonator, stays constant. This is visible in the fast time plot (Figure 2.15 c), where we see a lot of chaos until around −0.5 GHz detuning, were two single lines emerge, corresponding to two solitons. Once one or more solitons have been generated, it is always possible to detune the pump further and end in a single soliton state (Figure 2.15 d), which is also visible in Figure 2.15 (c) where one of the two solitons disappears as we see the down step in comb power in Figure 2.15 (a). This is characterized by step like drops in comb power, and is often referred to as soliton steps. We see that the comb appears at negative detunings, i.e. with the pump on the red detuned side of the MRR resonance. This has been shown both theoretically [66] and experimentally [43],[67], and can serve to validate our simulation model.

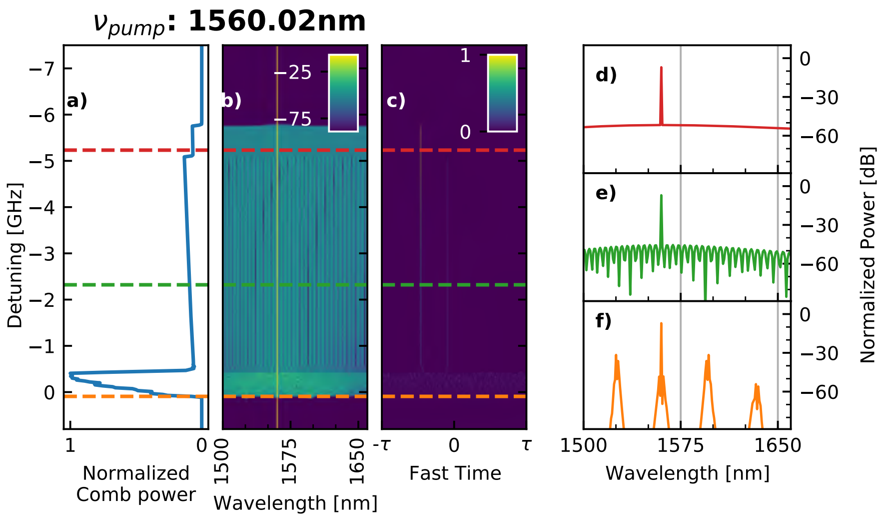

Figure 2.15: *Simulation of bright soliton generation where the detuning is swept linearly. Plot a) shows the comb power, plot b) shows the power per comb line, plot c) shows the intra cavity field intensity, plot d)-f) shows the frequency spectra of the output of the MRR at different points in the simulation.*

A different simulation is shown in Figure 2.16, where the small insets show the intensity of the intra cavity electrical field inside the circular resonator. Here we once again see the generation of primary comb lines in Figure 2.16 b), where the intra cavity electrical field starts to oscillate. It then transitions into the chaotic state Figure 2.16 c) where the intra cavity field is unstructured and rapidly changing from roundtrip to roundtrip, yet the frequency output could look like a frequency comb with several distinct frequencies. After the first drop in power we end up in a state with 4 circulating solitons, whereafter the system quicly drops through several soliton states until it ends in a 1 soliton state with a smooth spectrum. While the spectrum looks very choppy and uneaven in the multi soliton state the comb lines are still phase-locked. The unevenness is due

66. Coen et al., "Universal Scaling Laws of Kerr Frequency Combs" (2013)
43. Yi et al., "Active Capture and Stabilization of Temporal Solitons in Microresonators" (2016)
67. Herr et al., "Mode Spectrum and Temporal Soliton Formation in Optical Microresonators" (2014)

to a combination of interference between multiple solitons and the different angles between them. This can be shown by simulating the resulting pulse trains from a multi soliton state and Fourier transforming them to obtain the spectrum. This is shown in Figure 2.17 where the left plot shows the effect of different angles between two solitons, and the right plot shows the effect of different numbers of isoangulary spaced solitons. When the angular spacing is the same between two solitons, we see that every second line disappears due to perfect destructive interference and the spectrum looks like a frequency comb with two times the FSR. As soon as the angle starts being uneven, the interference is not perfect and several different structures can appear.

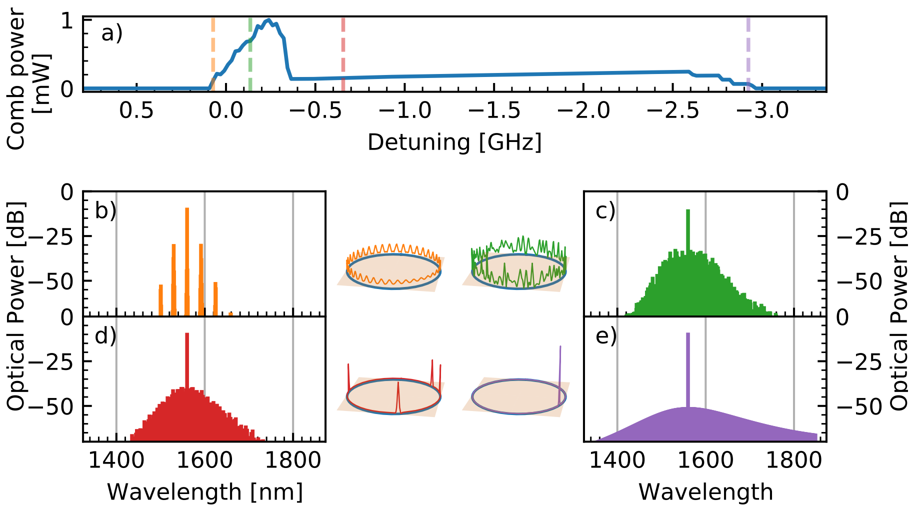

Figure 2.16: *Simulation of bright soliton generation where the detuning is swept linearly. Plot a) shows the comb power, plot b)-e) show the frequency spectra at different points in the simulation (The dashed lines). The small insets are the intra cavity field intensity.*

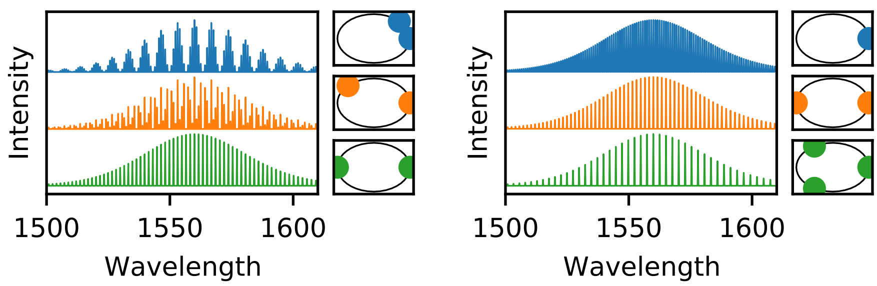

Figure 2.17: *Fourier transform of simulated pulse train. The spectra show the fourier transform of simulated pulse trains arising from 1-3 solitons propagating in the ring with different angular spacing. The small diagrams show the number and relative position of the soliton pulses.*

Extending the pyLLE package for Dark Pulse Combs

As mentioned earlier the normal dispersion devices rely on avoided mode crossings from mode interactions in order to achieve a local anomalous dispersion. The numerical simulation package from pyLLE can natively deal with this as it does not truncate the dispersion at second order, but works directly with the integrated dispersion. Unfortunately this is assumed to be a static value which we know is not the case if we change the heater power. In order to include this in the simulation we create a linear iterpolation of the integrated dispersion for each mode as a function of heater power. We then also include the thermal tuning coefficient which specifies how the detuning is affected by the heater power. With these two changes to the code of pyLLE we can now simulate the effect of ramping the heater power and try to generate dark pulse kerr (DPK) combs. To align the simulations with laboratory conditions we choose to ramp the heater voltage instead, and use the resistance R of the micro heater to convert it to an applied electrical power:

$$P_{\text{heater}} = \frac{V_{\text{heater}}^2}{R} \tag{2.3.7}$$

Figure 2.18 shows the simulation of a dark pulse comb where we ramp the heater voltage linearly from 6 V to 5 V. We fix the pump laser on the blue side of the voltage-shiftet resonance (at 6 V) and then ramp the voltage downwards, which gradually blueshifts the resonace due to the positive thermo optic coefficient of S_3N_4. As in the bright soliton case this decreases the detuning and crosses the point where the effective detuning is zero. This results in the generation of the DPK comb seen on Figure 2.18 d). In contrast to the bright soliton there is no distinct power drop visible in Figure 2.18 a) that indicates that we have now entered a soliton state. Instead there seems to be a very rapid rise in comb power followed by a broadening of the spectral structure as seen from Figure 2.18 d)-f). While it is not clear from these plots, we know that this spectral structure is indeed a mode locked frequency comb. To show the importance of the avoided mode crossing we also simulate pumping two other modes of the MRR. This is shown in Figure 2.19 and Figure 2.20, where the former shows a comb generated at a mode right next to the avoided mode crossing, and the latter shows the result of pumping far away from the crossing. While Figure 2.19 is still able to generate something that resembles a comb, Figure 2.20 cannot. It simply generates strong primary comb lines, but no further formation of a coherent comb.

A more detailed view of the dark pulse formation is shown on Figure 2.21. The top panel a) is again the comb power as a function of detuning. The black dashed line indicates the heater voltage, which is actually the parameter being swept in the simulation. The spectra in b)-e) show the comb at different states in the simulation, with the small inserts showing the time domain profile of the intra cavity intensity overlaid on top of the ring. The dark pulse Kerr comb manifests in the time domain as a strong background intensity with a periodic, square-like dip. As reported in [39],[40],[62] the width of the dip, and number of

39. Parra-Rivas et al., "Origin and Stability of Dark Pulse Kerr Combs in Normal Dispersion Resonators" (2016)
40. Nazemosadat et al., "Switching Dynamics of Dark-Pulse Kerr Frequency Comb States in Optical Microresonators" (2021)
62. Xue et al., "Mode-Locked Dark Pulse Kerr Combs in Normal-Dispersion Microresonators" (2015)

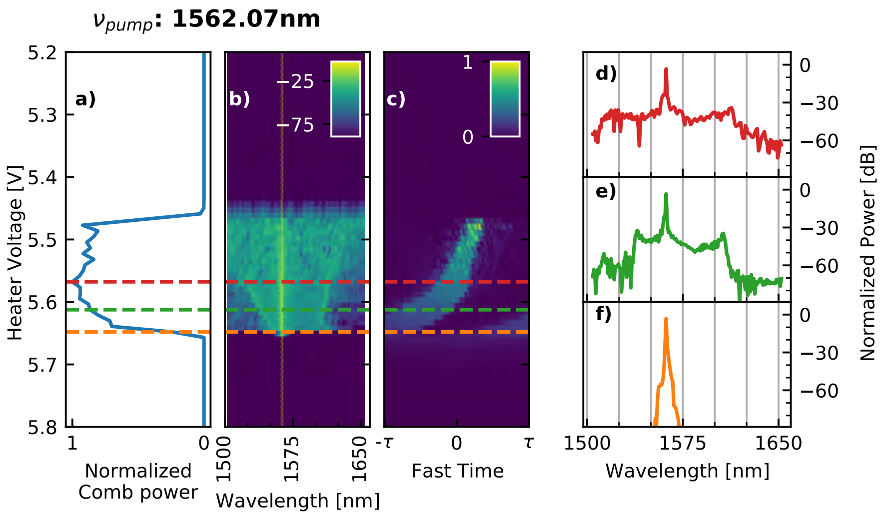

Figure 2.18: *Simulation of dark pulse Kerr comb generation.*

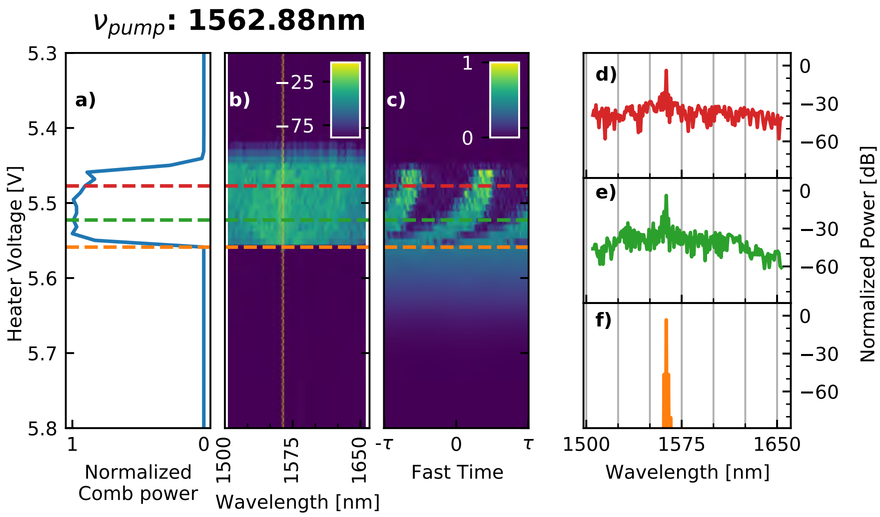

Figure 2.19: *Simulation of dark soliton generation when pumping a mode next to the avoided mode crossing.*

small oscillations at the bottom, is connected to the bandwidth of the generated comb. Mathematically it can be explained as switching waves connecting two stable, steady state solutions to the Lugiato-Levefre equation[39]. Besides not having the step like behaviour of bright solitons it is also possible to tune continuously back and fourth between different points.

Our simulation results in Figure 2.21 show that the comb is generated at negative (red) pump detunings. This clashes with the experimental and

39. Parra-Rivas et al., "Origin and Stability of Dark Pulse Kerr Combs in Normal Dispersion Resonators" (2016)

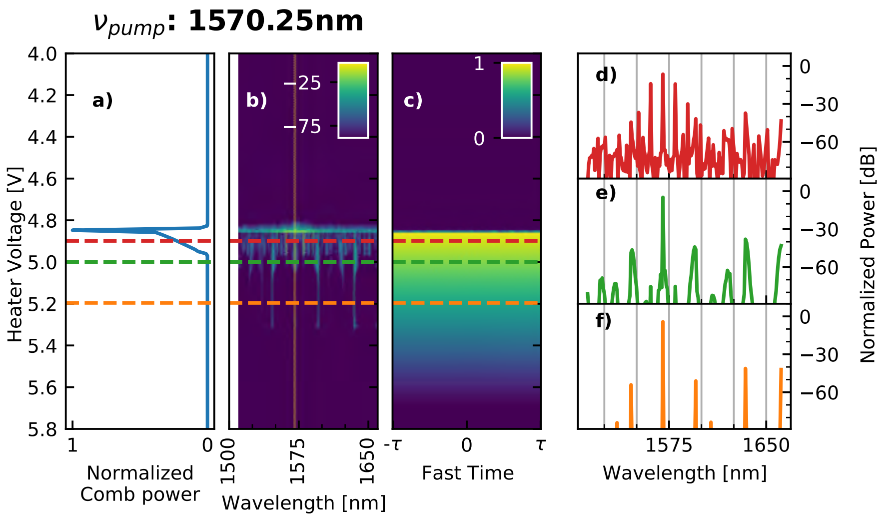

Figure 2.20: *Simulation of dark soliton generation when pumping a mode far from the avoided mode crossing.*

theoretical predictions shown in [40],[62] which strongly suggest that the DPK combs exist with the pump on the blue detuned side of the resonance. But while our model is not capturing all the dynamics of the system, it does offer an alternative to the common way of simulating these systems using coupled mode theory. By mapping out the dispersion at several different heating powers, we are able to forgo the need for modelling the mode interaction and simply extract the influence on the dispersion, which is what matters for our simulations.

40. Nazemosadat et al., "Switching Dynamics of Dark-Pulse Kerr Frequency Comb States in Optical Microresonators"(2021)
62. Xue et al., "Mode-Locked Dark Pulse Kerr Combs in Normal-Dispersion Microresonators"(2015)

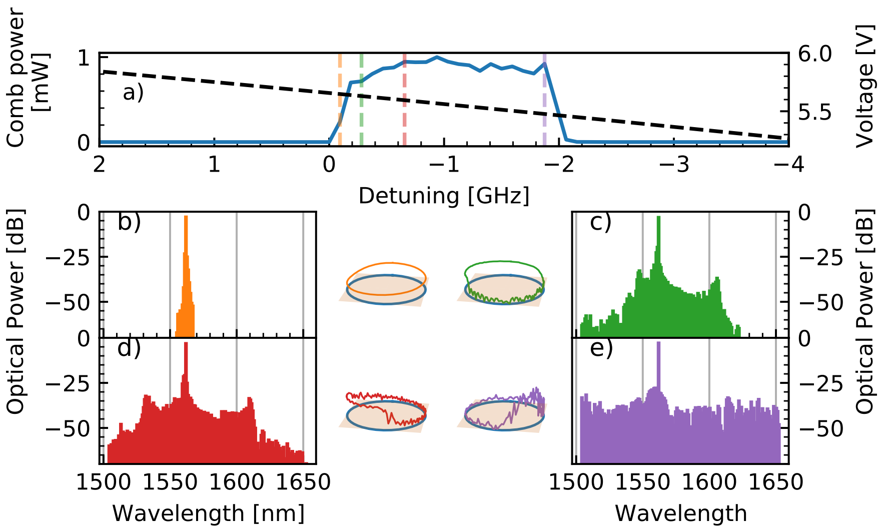

Figure 2.21: *Simulation of dark soliton generation where the heater voltage is swept linearly. Plot a) shows the comb power, plot b)-e) show the frequency spectra at different points in the simulation (The dashed lines). The small insets are the intra cavity field intensity.*

2.4 Comb generation

As we saw from both the theory and the simulations the effective pump detuning is the main parameter we will control when trying to generate and stabilize soliton frequency combs. But while our simulations could accurately control the detuning it is more difficult in practice. Due to the thermo-optical effect the MRR resonance frequency will change as the power inside the ring changes, as absorption will heat up the ring locally. This is especially a problem for bright solitons as they only exist when the pump is effectively red detuned. In materials such as S_3N_4 with positive thermo-refractive coefficients this leads to an unstable equilibrium, as illustrated on Figure 2.22. In the red detuned case, the pump moving closer to the resonance will result in an increase in optical power due to better coupling, which will increase the temperature and cause the resonance to redshift even closer to the pump, and visa versa when the pump moves away from the resonance. As shown in the previous section, when bright solitons are generated they first go through a stage of chaotic modulation instability, where the generated comb power increases. Once a soliton is formed the average power drops considerably and suddenly. Because bright solitons are always red detuned from the pump, this will cause a blueshift of the resonance which often causes the soliton state to be lost. One therefore needs to counter this with a quick "back step" either by quickly shifting the power or the detuning in the opposite direction[43], and has been shown to dramatically increase the likelihood of generating and maintaining a soliton state.

On the other hand, the dark soliton existence range is on the blue detuned side of the resonance, which leads to a form of passive stabilization as illustrated on the right panel of Figure 2.22. This also allows for a much simpler generation of dark solitons where the heater voltage can simply be tuned slowly by hand. As is also evident from the simulations (Figure 2.21), there is no clear indication in the comb power of individual soliton states. This makes it very difficult to systematically and repeatedly access identical dark pulse states, especially because the effective detuning can be very difficult to measure directly. One option is to use electro optical (EO) sidebands and the pound drever hall (PDH) technique[68], however this adds a level of complexity to the setup that we would like to avoid.

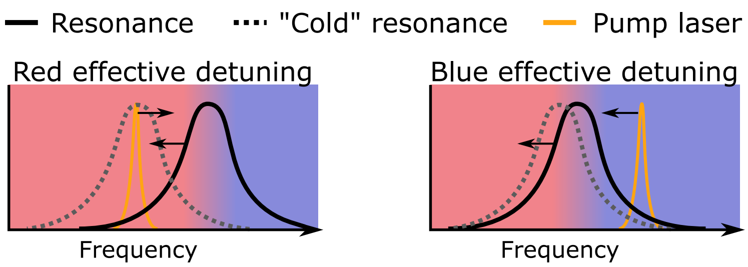

Figure 2.22: *When the thermo-optical coefficient is positive an increase in temperature, typically due to increased optical power, will redshift the chip resonance. In the red detuned case, this leads to an enhancement of the pump laser frequency fluctuations, whereas they are diminished in the blue detuned case.*

43. Yi et al., "Active Capture and Stabilization of Temporal Solitons in Microresonators"(2016)
68. Yi et al., "Soliton Frequency Comb at Microwave Rates in a High-Q Silica Microresonator"(2015)

It was realized as early as 2013[66], that the intra cavity power of a bright soliton would theoretically depend linearly on the detuning, and therefore inversely that the detuning could be inferred from the output power of the comb. This was used to successfully generate and stabilize a bright soliton based on feedback from the measured comb power[43]. The aim of the work presented in the following is therefore to investigate if this technique can be used to generate and stabilize dark solitons. Furthermore we will try to control the pump detuning by shifting the MRR resonance with the micro heater instead of tuning the frequency of the pump laser itself, allowing us to use a fixed frequency pump laser. Fixed frequency lasers are generally more stable in both long term stability and linewidth, and since all the comb lines are generated from the pump laser, they will all inherit this performance.

Resistive micro heaters have already been used to generate and stabilize bright solitons[69] and dark solitons in photonic molecules[6][70], but the challenge of utilizing the same thermal tuning technique for our devices is that the mode interaction, which facilitates the generation of dark solitons, also strongly depends on the applied heat. Effectively this couples two of the three important parameters, namely the effective detuning and the dispersion.

Automatic Comb Generation

In order to generate and stabilize DPK combs we use the setup seen on Figure 2.23. The frequency spectrum of the light is illustrated as small plots above the fibre at different stages of the setup. We use an id-photonics Cobrite type NX tunable continuous wave laser[71] with an upgraded linewidth of 10 kHz and 16 dBm of output power, of which we use a few mW. This is then amplified to 200 mW to 600 mW in an erbium doped fibre amplifier (EDFA) which also introduces a broad background due to amplified spontaneous emission (ASE). The light is then sent through an optical band pass filter (BPF) to remove the ASE before an adjustable lensed fibre is used to couple the light onto the straight waveguide on chip (see Section 1.2 for details.). From the straight waveguide the light leaks into the MRR and a comb is generated and emitted back into the waveguide. Another adjustable lensed fibre is then used to couple the light off the chip again. After the MRR two cascaded −20 dB power couplers are used to sample off a small amount of the light. The tap from the first coupler is sent through a short pass filter (SPF) in order to remove the remaining pump light before detection on a fibre coupled photodiode. While the SPF does remove half of the comb power, the signal will be proportional to the amount of generated comb light. The light from the second coupler is directly detected and will be dominated by the residual pump power. We can then use this to monitor the fibre coupling efficiency on and off the chip.

The easiest way to generate a DPK comb is by applying a large heating power to the ring and then place the pump on the blue detuned side of the

66. Coen et al., "Universal Scaling Laws of Kerr Frequency Combs"(2013)
43. Yi et al., "Active Capture and Stabilization of Temporal Solitons in Microresonators"(2016)
69. Joshi et al., "Thermally Controlled Comb Generation and Soliton Modelocking in Microresonators"(2016)
70. Óskar Bjarki Helgason, "Dissipative Kerr Solitons in Normal Dispersion Microresonators"(2020)
71. IdPhotonics, *Mainframe Series CoBriteMX Lasers Accessed on 2021/04* ()

[6] Photonic molecules are two coupled micro resonators, where the mode interaction is tunable independently of the MRR resonance frequency.

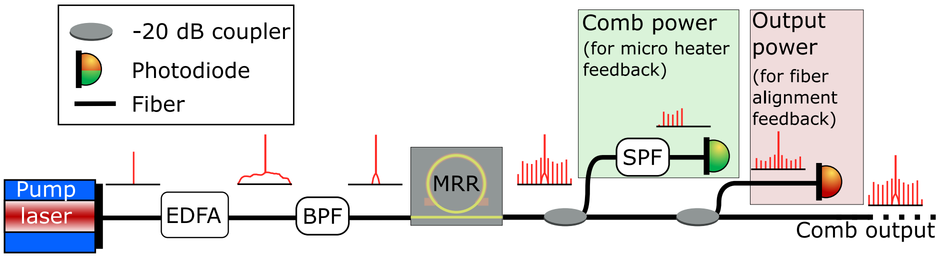

Figure 2.23: *The optical setup used to generate and stabilize the DPK combs.*

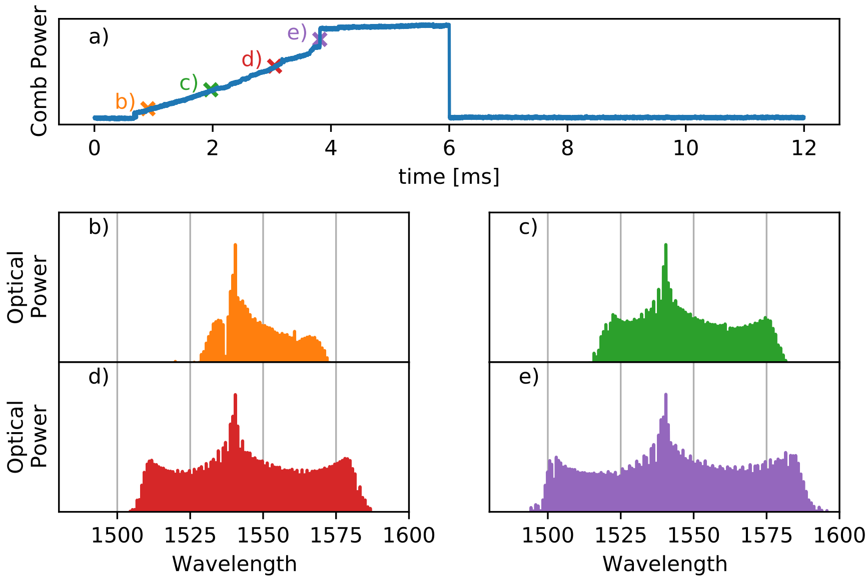

Figure 2.24: *Experimental data showing the continuous tunability of the dark soliton. Data from Gap 2, pumped around 1540 nm with 28 dBm pump power.*

thermally shifted resonance. We then simply sweep the voltage downwards and thereby cool the ring, which blueshifts the resonance closer to the pump. This was done experimentally in [40], and we replicated it in our setup, getting the results plotted on Figure 2.24, which agree qualitatively with the simulations presented in Figure 2.21

Choosing the right pump frequency is a crucial part of generating the pump. For our devices the strongest mode crossings are around 1540 nm and 1562 nm, and such we are restricted to pump these resonances. While each device is slightly different, they will generally produce combs which look similar. An example of two combs is shown on Figure 2.25 where the optical spectrum of a comb at two different mode crossings is plotted. The large background is because this particular data is taken without an optical BPF to remove the ASE. Both combs are equally wide and have comparable conversion efficiencies, but as we will see in the next chapter, we wish to use the comb for telecommunica-

40. Nazemosadat et al., "Switching Dynamics of Dark-Pulse Kerr Frequency Comb States in Optical Microresonators" (2021)

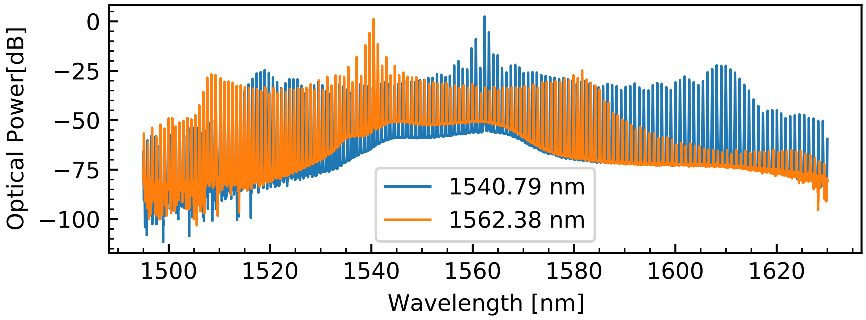

Figure 2.25: *Optical spectra of two dark pulse Kerr combs from the Gap 2 device, pumped at two different wavelengths. In this particular experiment we did not have the optical BPF to remove the ASE from the pump EDFA.*

tion experiments, and we therefore focus on combs generated around 1562 nm from here on out.

As mentioned earlier, the dispersion and detuning are both linked to the heater voltage. This means we need to adjust the pump laser position very carefully, in order for the thermally controlled detuning to coincide with the correct dispersion. This can be seen in Figure 2.26 where three different attempts at generating combs are plotted

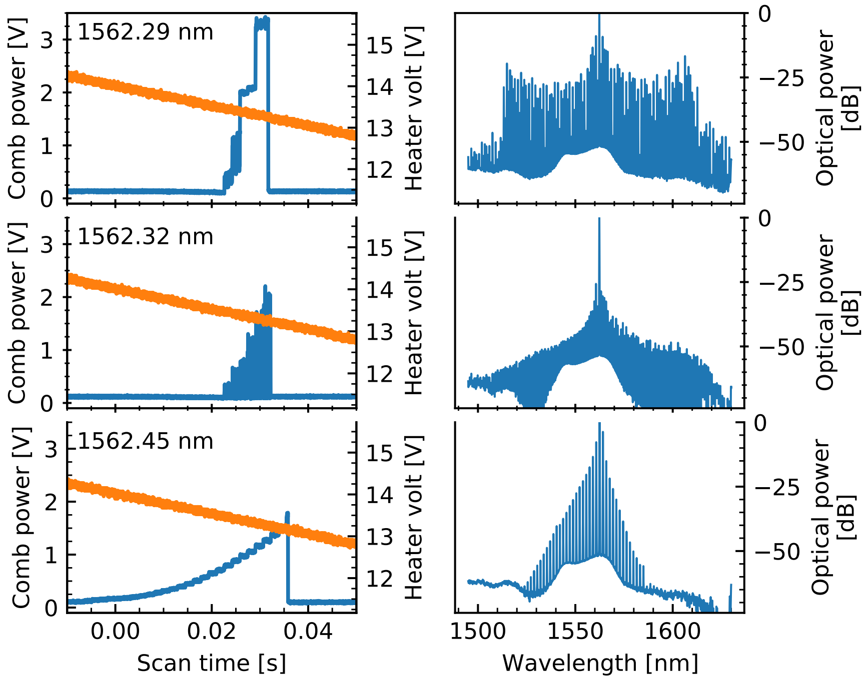

Figure 2.26: *Three different attempts at producing combs in the Gap 2 device around* 1562 nm*. The left column shows the comb power (blue) and heater voltage (Orange). The right column shows the optical spectrum of the comb if the heater voltage is stopped at the highest point of the feature shown in the left column.*

2.5 Comb stabilization

It is normally not advised to use thermal control for stabilization, as the thermal relaxation period of most materials is low and thereby limits the feedback bandwidth. However the small size of micro ring resonators compensates for this. The frequency response of the heater can be investigated by measuring the Bode plot of the device. This is done by applying a small sinusoidal voltage to the heater and recording the resulting resonance shift. By increasing the frequency of the applied sine wave we can find the point where the resonance shift cannot follow the heater voltage. This is shown on Figure 2.27. The plot shows a -3 dB gain point (red dashed line) at 16 kHz and a 180° phase lag point at 180 kHz. As this is open loop gain, a controller could easily be created which allowed feedback bandwidths up to 100 kHz.

The feedback circuitry is built around a RedPitaya (STEMlab 125-14) as shown on Figure 2.28, which is much faster than 100 kHz. Through the use of the software package Python RedPitaya Lockbox (PyRPL)[72] the RedPitaya can run Proportional-Integral-Derivative (PID) based feedback loops on the internal field programmable gate array (FPGA), while still allowing us to configure the settings of the PID from an external computer. The RedPitaya has

72. Neuhaus et al., *PyRPL*(2016)

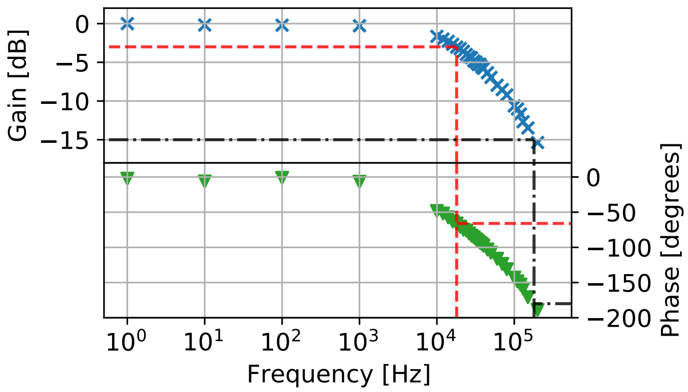

Figure 2.27: *Bode plot of heater feedback system.* −3 dB *gain point is at* 16 kHz *(red dashed line) and* 180° *phase lag point is at* 180 kHz *(black dotted line).*

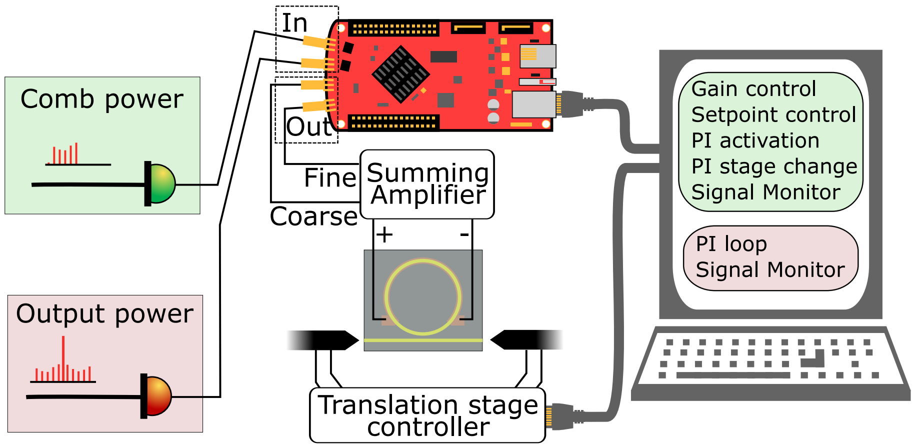

Figure 2.28: *A schematic overview of the feedback systems used in generating and stabilizing the DPK combs.*

two inputs which are used for the comb power (green) and the output power (red), and two outputs which are both used to control the micro heater, as shown on Figure 2.28. The fibre translation stages are controlled through a dedicated piezo controller through the external computer.

In investigating the stability of our generated dark solitons we will distinguish between two different types of stability:

- Comb state stability, which describes the stability of the comb operation, i.e. how long the soliton can persist inside the micro ring resonator and produce a working comb.
- Comb line stability, which details the frequency, phase, or amplitude stability of the individual comb lines.

The main difference is that the state stability is important for any comb application, as they all rely on the existence of equidistant frequency components, whereas the degree of comb line stability required varies vastly for different applications.

The comb power feedback loop uses a Proportional and Integral (PI) loop, with the gains and setpoints being controlled remotely by the computer as shown on Figure 2.28. When generating a soliton state we need to be able to sweep the heater voltage over a larger range than what is necessary when stabilizing a state. Combined with the fact that the RedPitaya is limited to $-1\,\mathrm{V}$ to $1\,\mathrm{V}$ on the outputs with a minimum step size of $0.122\,\mathrm{mV}$ due to the 14-bit resolution of the digital to analog converter (DAC), we therefore use both of the outputs on the RedPitaya and add them together with unequal weights in order to create a *fine* and *coarse* feedback signal. The addition is done using an operational amplifier which also amplifies the feedback signal to $0\,\mathrm{V}$-$15\,\mathrm{V}$. The two outputs are controlled by two separate PI loops running internally on the RedPitaya, and we switch between them using some digital logic implemented on the remote computer.

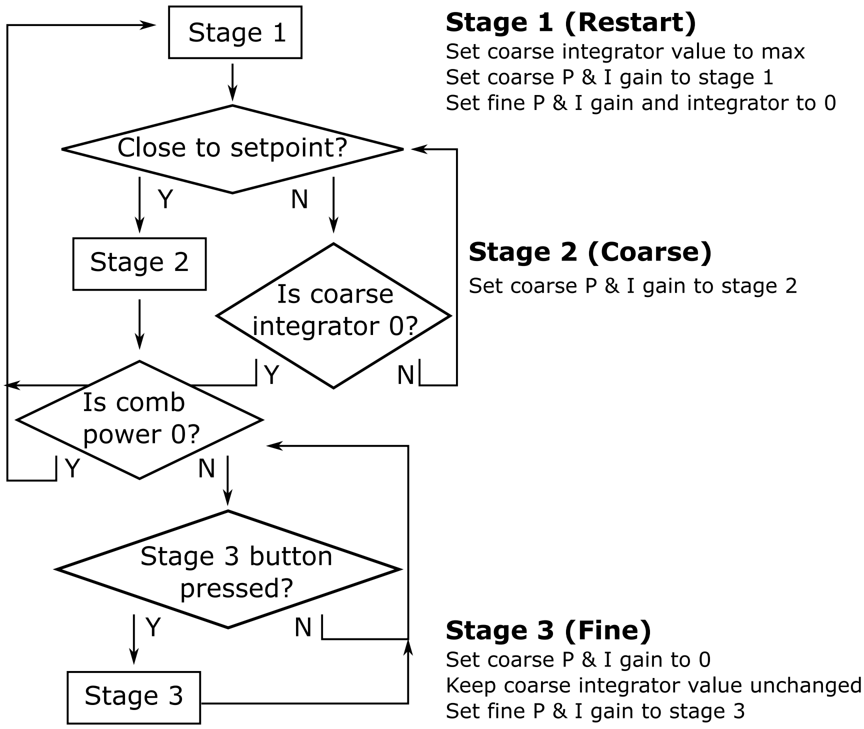

Figure 2.29: *Block diagram of the feedback loop used to generate and stabilize the dark soliton comb state.*

A block diagram of the comb generation and stabilization process can be seen on Figure 2.29. The state generation starts in *Stage 1* where the fine PI loop is turned off by setting all internal values to zero. The coarse P and I gain is set low and high respectively, and the integrator value is set to the maximum output of the RedPitaya. Because the comb power at this point is zero, the coarse PI loop will drive the integrator value downwards, effectively sweeping the heater voltage downwards. This changes the dispersion, and shifts the resonance frequency closer to the pump laser. As the detuning decreases, the FWM process will begin, and comb power begins to rise. Once the comb power starts approaching the setpoint, the coarse PI loop will slow down the ramp speed and weakly stabilize at the correct value. At this point the computer is constantly checking the measured comb power value. If it is sufficiently close to the setpoint, the computer will go to *Stage 2* where the I gain is lowered considerably and the P gain is increased. The coarse PI loop cannot always generate a soliton state, as the sudden increase in comb power tends to influence the system thermally[7]. It is therefore highly likely that comb power can be generated, but the coarse PI loop not react fast enough. In this case, the integrator will continue towards zero, and will restart once it hits zero.

In *Stage 2* the comb state can be maintained over an extended period of time. As shown on Figure 2.30 the comb state becomes unstable and disappears shortly after the PID feedback is turned off at the 27 minute mark. If the comb

[7] Though still less than the power drop in bright soliton generation.

state is lost while the feedback system is running, it will automatically restart and go back to *Stage 1*.

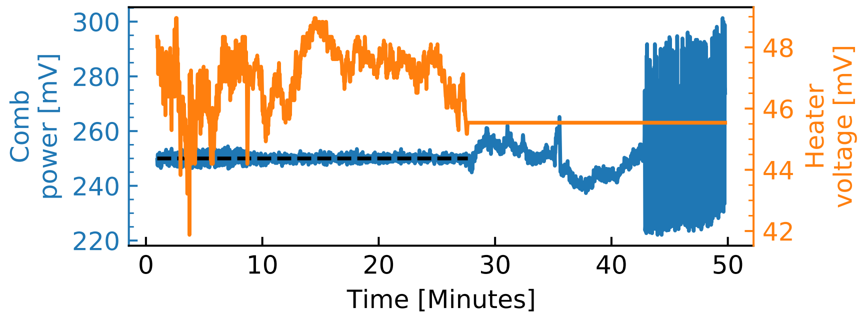

Figure 2.30: *Comb power and heater voltage over 50 minutes. The black dashed line indicates the comb power stabilization setpoint. The stabilization feedback is turned off (frozen) around 28 minutes. Afterwards the comb state quickly disappears.*

An illustration of generating a comb state is shown on Figure 2.31, where we see the process restart 4 times before it finally manages to stabilize and end in *Stage 2*. In this process, the coarse I-gain is used to determine the sweeping speed, which is important as it needs to be slow enough to allow sufficient comb generation, but fast enough to not be influenced by thermal effects.

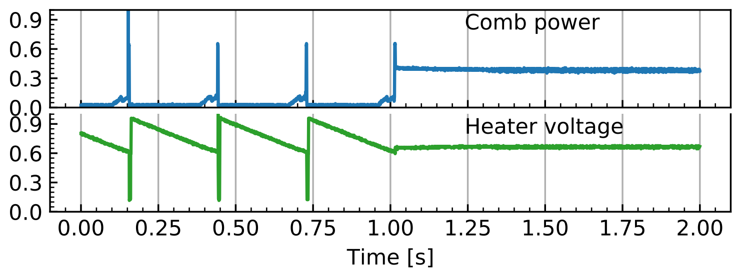

Figure 2.31: *Locking scheme for generating Dark pulse Kerr combs. Top plot shows normalized comb power, bottom plot shows normalized heater voltage.*

In order to shift from the coarse to the fine output, we freeze the coarse PI loop by zeroing the P and I gain, but keeping the integrator value constant. We then set the P and I-gain of the *fine* loop to a non zero value, which causes the fine PI loop to take over the stabilization. This can be seen in Figure 2.32 where the system shifts from *Stage 2* to *Stage 3* around the 5 s mark, and clearly shows the difference in dynamic range of the PI loops. While the digital controller has many advantages, such as allowing different phases during a locking sequence, and easy adjustment of parameters, it also adds digitization noise. This can be seen in Figure 2.33 where a 10-bit RedPitaya is compared to a 14-bit RedPitaya. It is clear from the figure that the 10-bit PI loop has digitization errors larger than the fluctuations of the input signal, which limits the performance of the PI loop.

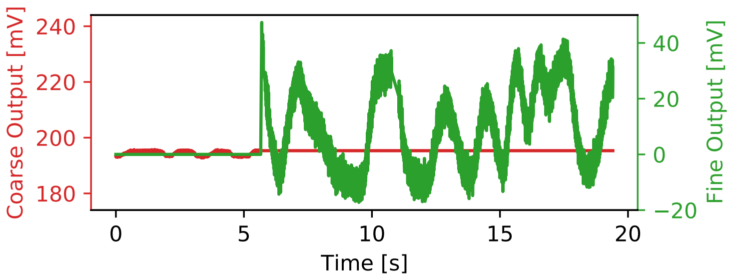

Figure 2.32: *Output of the fine and coarse PI loops from the RedPitaya. Around the 5 s mark the control goes from Stage 2 to Stage 3, which increases the dynamic range of the controller*

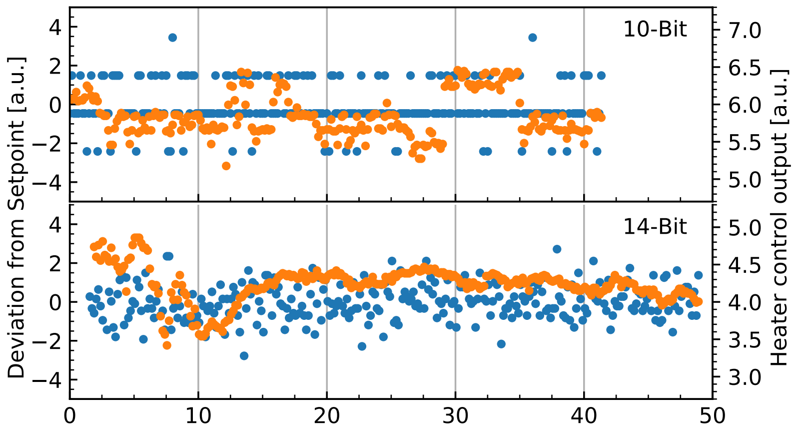

Figure 2.33: *Difference between stabilizing with a 10-bit digital PID controller or a 14-bit controller. Blue traces are deviations from setpoint (errors), Orange trances are heater controller output.*

Input power stability

Once a comb has been generated and the comb power stabilized, the second most important thing is to maintain a constant input power to the chip. Not only does the power directly determine the FWM gain, but the local heating in the ring due to absorption will in turn influence the detuning and the dispersion. It is therefore important for long term operation, that the input power is stable. As mentioned earlier, the input power depends on two things; the free space coupling efficiency, and the power stability of the pump laser. The latter has been measured to be stable, as we run the EDFA into saturation in current control mode, effectively making the EDFA output independent of the input power. It is therefore the free space alignment of the lensed fibres which is our main cause of power instability. As seen on Figure 2.34, the output power drops significantly over the course of a few hours. This is strongly correlated with the temperature of the lab and is most likely caused by a difference in thermal expansion and contraction of the chip holder and fibre holder. The

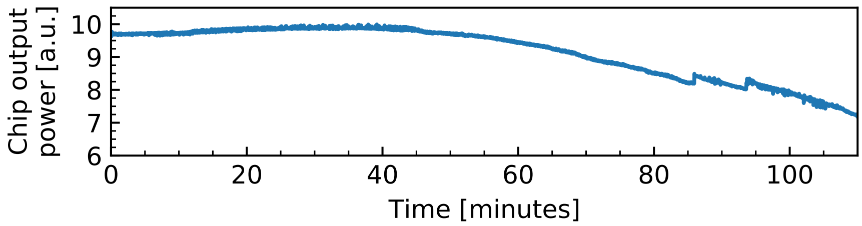

Figure 2.34: *Power output of a comb as a function of time, when fibre alignment feedback is not implemented. A significant output power drop happens in just over an hour. This is primarily due to misalignment of the coupling fibres.*

input fibre also displays a thermal runaway behaviour. This is likely due to small misalignments causing large amounts of light to be reflected off the facet instead of coupling into the waveguide. The reflected light then heats up the tip of the lensed fibre and misaligns it further. A similar thing can be observed on the output fibre, but here it is just the light not coupled to the fibre which instead heats up the side of the fibre thereby displacing it. It has been observed how the output fibre would move up to 500 µm when the power to the chip was increased. To counteract this we use piezo controlled translation stages to continuously readjust the fibre position by changing the alignments perpendicular to the fibre axis. Controlling only 2 of the 3 degrees of freedom is sufficient to keep the power stable and minimizes the risk of accidentally damaging the chip facet with the fibre.

The fibre alignment itself is a simple peak search algorithm running on a remote computer. We still use the RedPitaya to digitize the measured output power (red path in Figure 2.23 and Figure 2.28), but use separate piezo controllers to control the translation stages directly from the computer. The block diagram for the power stabilization loop can be seen in Figure 2.35, but can be boiled down to:

1. Step piezo voltage in one direction until power drops.
2. Then step piezo voltage in opposite direction until power drops again.
3. Change piezo.

The feedback system is made stable by adjusting the step size and adding an artificial delay between steps. An example of the loop running can be seen in Figure 2.36, where the output power is maintained over several hours. The top plot shows the piezo voltage of the 4 axes perpendicular to the chip facet with two input and two output piezo voltages. The black graph shows the air temperature. We see a correlation between the air temperature and the feedback applied to the piezos as they compensate for the change in laboratory conditions. The bottom plot shows the measured chip output power while the stabilization is active. While there are still variations we have largely decoupled it from the air temperature and the thermal runaway effects no longer happen. The remaining variation in power likely due to not adjusting the axis parallel to the fibre. The chip output power does depend on whether a comb is generated or not, so our system briefly disables the power optimization

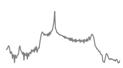

if the comb stabilization unlocks, and engages it again once a comb has been generated.

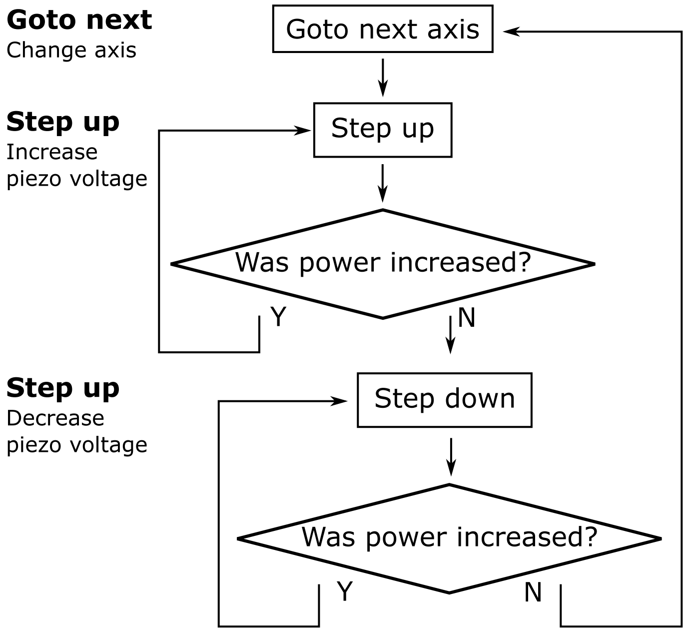

Figure 2.35: *Programming block diagram for the simple peak search algorithm implemented to stabilize the optical power output of the chip.*

Besides the laboratory air temperature, the setup is also sensitive to air currents which affect the surface temperature of the chip through convection, and more importantly cause the free hanging part of the lensed fibres to move around and misalign leading to problems similar to the ones stated above. This was alleviated by placing the entire setup inside a box enclosure. The effect can be seen in Figure 2.37(b) and Figure 2.37(a) which show multiple scans of a resonance over 50 s with and without the lid on the box enclosure. Without the lid on we see that the chip resonances shift several tens of MHz over the course of a minute. This can make it very difficult to maintain a stable pump laser detuning.

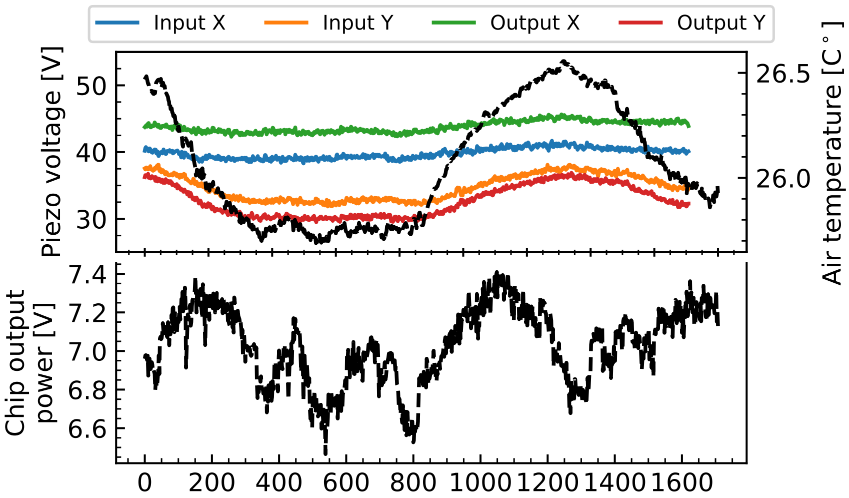

Figure 2.36: *Power output of a comb as a function of time, when fibre alignment feedback is implemented. The top plot shows four coloured traces corresponding to the piezo voltage on the four axes perpendicular to the chip facet (two for input and two for output). The black trace is the air temperature. The bottom plot shows the measured chip output power.*

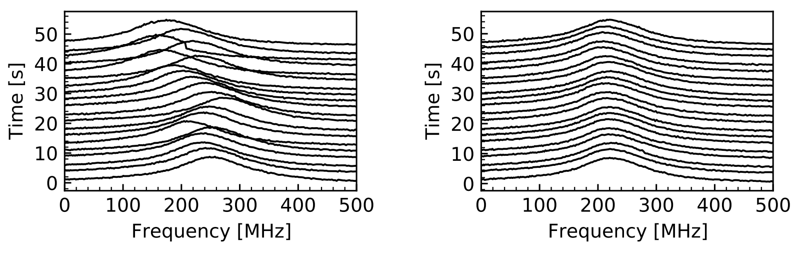

(a) (b)

Figure 2.37: *Multiple scans taken over* 50 s *of a device resonance with* ***a)*** *no enclosure and* ***b)*** *a full enclosure surrounding the chip holder. Without the enclosure the resonance shifts several tens of* MHz.

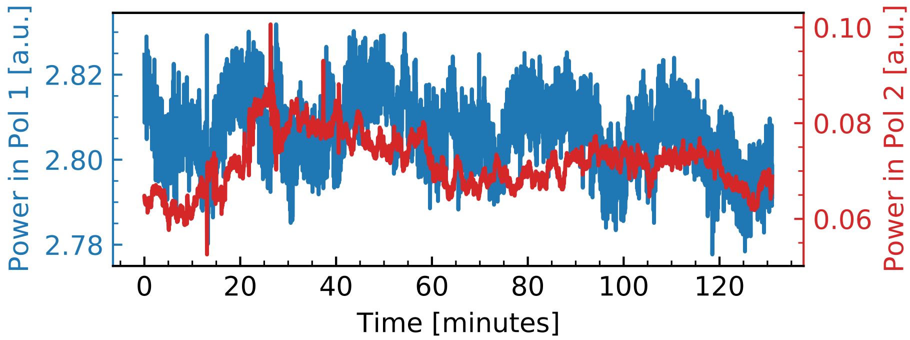

Figure 2.38: *Measured optical intensity of both input polarizations monitored over two hours. We observe no significant change in polarization.*

Polarization stability

The DPK comb setup is polarization sensitive as the chip is optimized to just one of the polarization modes. We therefore minimize the light coupling to the wrong polarization by using a set of paddlewheels for manual polarization control, however the lensed fibres do not contain stress cores and are therefore not polarization maintaining. This was chosen in order to prevent the need of rotational fibre mounts, on top of the existing 3D translation stage. We test the feasibility of this solution by inserting a temporary −20 dB coupler to split of a small amount of light right after the paddlewheels, but before the lensed fibre used for incoupling. A polarizing beamsplitter was then used to separate the two polarizations and the optical power levels of each were monitored. As seen in Figure 2.38, there is no significant change in polarization over the two hour measurement timespan.

Determining a phase-locked comb state

Once the comb state has been generated and stabilized, we need to ensure that the state is indeed a frequency comb where the lines are phase-locked to each other. While DPK combs do not go through the same stages of modulation instability as bright solitons, they can still enter a chaotic state where there will be visible beatnotes in the radio frequency (RF) domain due to multiple overlapping but non-locked sub combs. On Figure 2.39 we see a measurement of the RF spectrum performed by sampling the entire comb spectrum on a photodiode. Here, the top depicts a noisy comb, where the optical spectrum has an unexpected shape and the RF spectrum shows multiple frequency components. In comparison to that the bottom plots on Figure 2.39 show a completely flat RF spectrum and the expected optical spectrum shape. We do expect to see a beatnote in the RF spectrum corresponding to the FSR of the comb but as it 105 GHz for these devices it will be impossible for us to detect with our normal photodiodes.

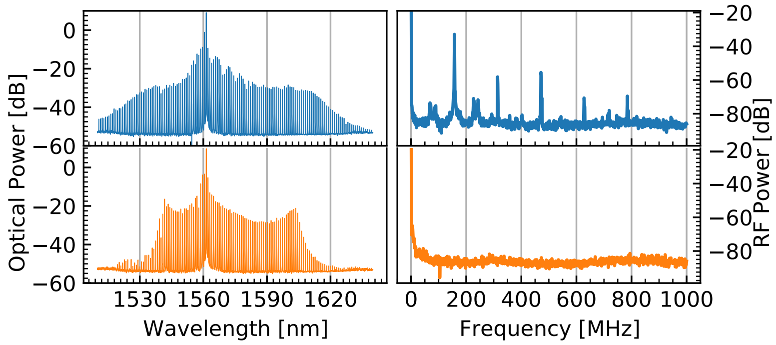

Figure 2.39: *Top row shows a non phase-locked comb, with clear beatnotes between different parts of the comb in the RF spectrum shown on the right. The optical spectrum on the left also does not look like what we expect from our simulations. Bottom row is a phase-locked dark pulse Kerr comb, indicated by the clean RF spectrum on the right plot and the familiar optical spectrum on the left.*

Comb line stability

Will all the above mentioned stabilization schemes in place, the setup is able to maintain a phase-locked frequency comb over several hours, and in some cases days, as seen on Figure 2.40. While the comb does unlock at some points, indicated by the black markers above the plot it automatically relocks and regains a phase-locked comb state.

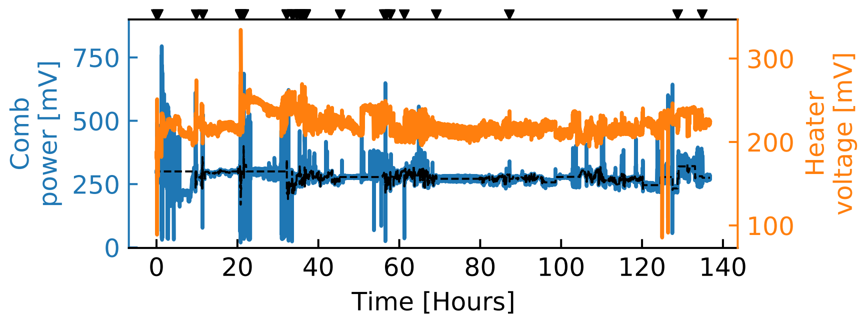

Figure 2.40: *Comb power and heater voltage over a 5 day period. The black dotted line indicates the setpoint and the black triangle markers at the top indicate when the comb relocked automatically.*

As mentioned previously, there are no immediately distinct features visible in the comb power, like the bright soliton power drop, which can be used to distinguish different DPK comb states. A bright soliton state is characterized by the number of propagation solitons (see inset in Figure 2.16) and it is only possible to tune in the direction that reduces the number of solitons. On the other hand dark pulse states are only characterized by the time domain width of the intensity dip, and can furthermore be tuned freely back and fourth over

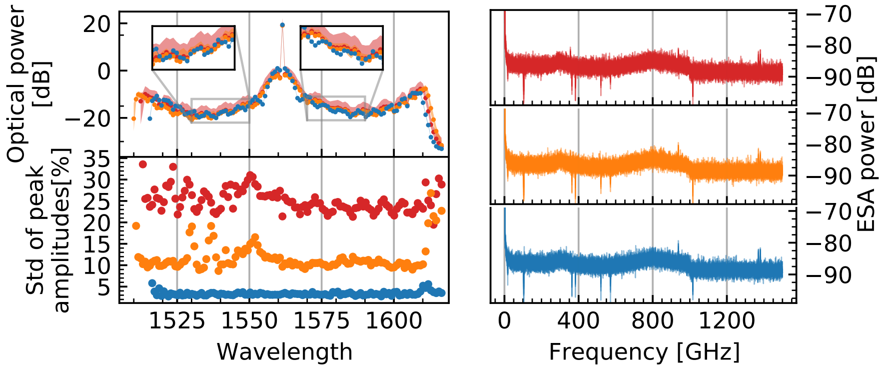

Figure 2.41: *Left shows the peak amplitude of each comb line (top), recorded 30 times, with the shaded area representing the min/max values. The standard deviation is plotted (bottom) as a percentage of the mean value of each peak. The ESA traces are shown on the right plot.*

a large parameter space as shown in Figure 2.24 which leads to these states being less robust against parameter fluctuations. As we will show now this leads to continuous changes of the comb states even when the comb power is stabilized and the RF spectrum is clean.

Short term stability

To investigate the short term stability we generate a comb state three times (red, yellow and blue) using the same stabilization parameters, and record 30 scans of the optical spectrum on an optical spectrum analyzer (OSA) and 30 scans of the RF spectrum on an electronic spectrum analyzer (ESA) over the course of 5 min. For each scan we measure the peak amplitudes of the optical spectrum and calculate the standard deviation of the peak amplitudes over the 30 scans. This is shown on the left plots of Figure 2.41 where the top left plot shows the average peak amplitudes of the 30 scans, with the shaded area representing the min/max of the recorded values. The standard deviation as a percentage of the mean peak amplitude is plotted on the bottom left, in order to better compare comb lines with different peak powers. The right plots on Figure 2.41 show the corresponding RF spectra for the three generated combs. We see that one of the generated combs (red) has a peak amplitude standard deviation of 25-30 percent of the mean peak amplitude, which is also evident by the large shaded area in the top left plot. The two other states (yellow and blue) both show better but different performance. Our current method of generation and stabilization therefore leads to non-reproducible comb states with vastly different comb line amplitude stabilities. To exclude any instabilities of the heater system itself we also compare to a comb state stabilized by tuning the laser frequency instead of the heater, while still using the monitored comb power as the input. Figure 2.42 shows that there are no significant difference in statistics over 30 measurements between the feedback mechanisms except that the line to line variation is smaller for the heater feedback system. This indicates that the issue lies with determining the comb state or pump detuning

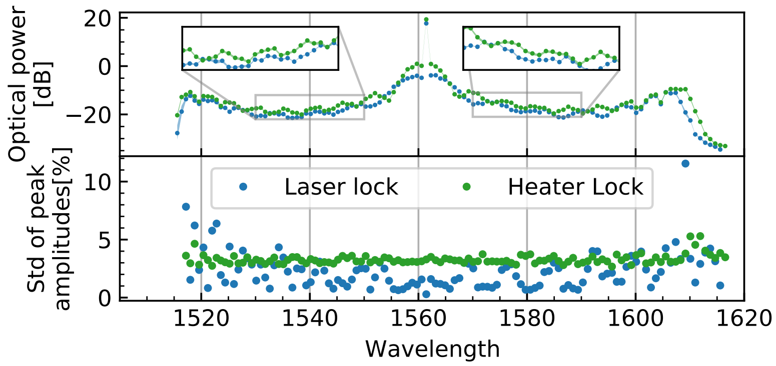

Figure 2.42: *Optical spectrum, and standard deviation of peak amplitudes over 30 optical spectra, obtained with the comb state stabilized using either the heater or the laser frequency.*

based on the measured comb power.

Long term stability

If we shift our focus towards the long term stability, then we can see from Figure 2.40 that the comb can operate for several hours at a time. But if we zoom in on just a small part of the graph, and plot it by itself, we get the data in Figure 2.43. Here the top plot shows the comb power stabilized to the black dashed line indicating the setpoint. Around the 45 min mark we see the heater voltage feedback signal suddenly jumps to a different level and operate there for a few minutes. This means the PI feedback system suddenly decided to change the output.

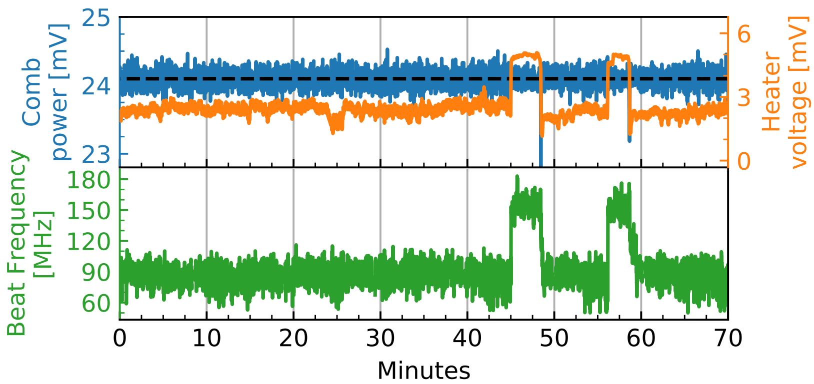

Figure 2.43: *Top plot shows comb power and heater voltage control signal over time. The dashed line indicates the comb power setpoint. We see two sudden jumps in heater voltage, with almost no response in the comb power. Bottom plot shows the frequency of one of the comb lines, measured up against a stable frequency reference.*

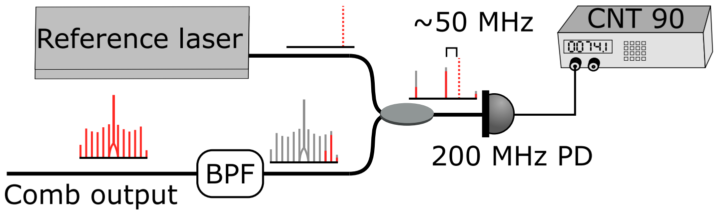

Figure 2.44: *An optical BPF is used to filter out a small number of comb lines. This group is then combined with the reference laser of choice in a 3 dB coupler. The reference laser is tuned to be near one of the lines and the resulting beatnote is measured on the frequency counter (Pendulum CNT-90).*

As this data is only recorded every second while the feedback loop is running much faster, it is likely that the feedback reacted to some short fluctuation in the comb power. Normally this would lead to a sudden change of heater feedback which would then change the comb power and the feedback loop would then adjust the heater voltage to drive the comb power back to the setpoint. But from Figure 2.43 we see that the comb power is the same at the two different heater levels, indicating that there are two different configurations of applied heater voltage which produce the same comb power signal.

Simultaneously with measuring the comb power and heater feedback we also measure the frequency of one of the comb lines. This is done through a heterodyne beat measurement using the setup shown in Figure 2.44. A small group of lines are extracted from the comb using a narrow optical BPF, and are then combined with a stable reference laser and measured using a commercial frequency counter[8][73]). The bottom plot of Figure 2.43 shows the beat frequency measured simultaneously with the comb power and heater voltage above. At the point where the heater voltage changes we see a shift in frequency of $\sim 70\,\mathrm{MHz}$, which is expected as a change in heater voltage will shift the MRR resonances. This measurement indicates that the comb output power is not ideal for stabilizing the comb, as two different heater voltages can produce identical comb powers. Because the comb power is the total integrated power over half of the comb bandwidth (see Figure 2.23), it is possible that the two heater voltages result in comb states with vastly different comb line amplitudes, but similar total comb power.

Similar features can be if the comb power setpoint is changed. This is illustrated on Figure 2.45 which shows what seems to be the existence of several distinct states which the comb prefers to operate in. The top plot in Figure 2.45 shows the comb power input to the RedPitaya and the heater control output from the RedPitaya over several seconds sampled at $\sim 1\,\mathrm{ms}$. The black dotted line is the setpoint of the feedback system. The comb power seems to jump between two levels, with the heater output showing some repeated pattern correlated with the comb power jumps. The jumping effect is triggered by choosing a setpoint between the two levels. As neither the high nor the low comb power level is at the setpoint, the integrator will drive it away from that

73. Pendulum, *CNT-90 Datasheet Accessed on 2021/04* ()

[8] Pendulum CNT-90

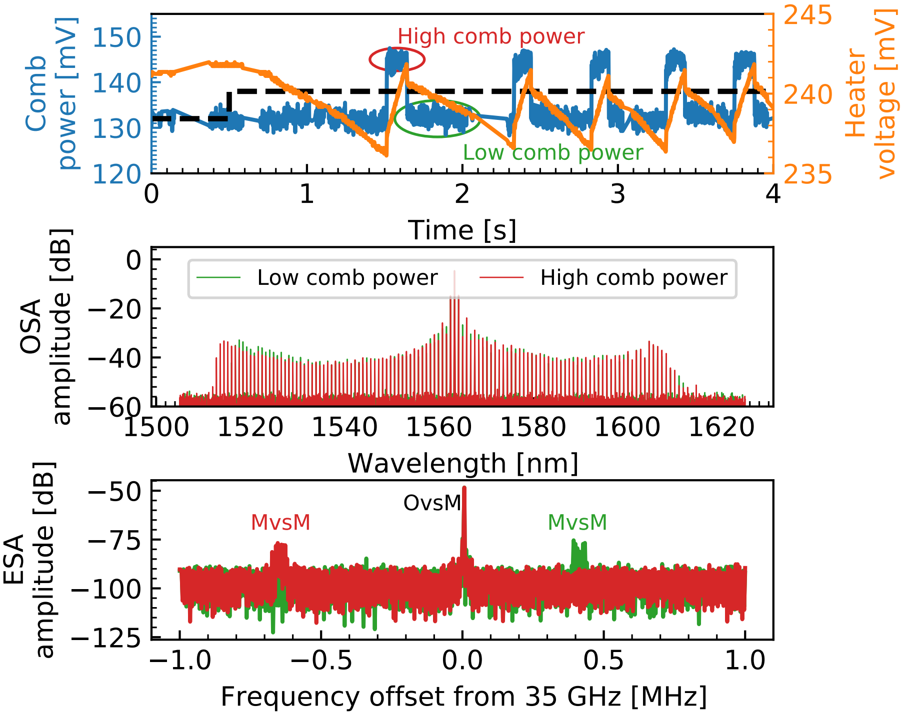

Figure 2.45: *Investigation of state changes due to change of feedback setpoint. Top plot shows comb power and heater voltage control signal as a function of time. Black dashed line indicates setpoint. Middle plot shows OSA spectra of the two comb power states indicated on the top plot. Bottom plot shows the RF spectrum of the two comb states after electronic downconversion using the setup in Figure 2.46.*

state and cause a sudden jump. In contrast with Figure 2.43 these jumps are visible in both the measured comb power and the applied heater control signal.

The middle plot of Figure 2.45 shows the optical spectrum of the two states labelled "High power" and "Low Power" in the top plot. We see that they are clearly two different states with both a different number of comb lines and different amplitudes in the comb lines. In order to get a better idea of whether the FSR is affected by such a heater voltage jump, we used a technique called electronic down conversion, where the entire comb output is sent through a Mach-Zehnder modulator (MZM) as illustrated on Figure 2.46[9]. The intensity modulator is run at $\nu_{\mathrm{mod}} \approx \frac{1}{3}\mathrm{FSR} = 35\,\mathrm{GHz}$, which creates two symmetrically placed sidebands on each side of the primary comb lines. When looking at the RF spectrum of the modulated combs shown on the bottom plot of Figure 2.45, we see one sharp peak around the modulation frequency labelled "OvsM". This is the beatnote between the original lines and the lines generated through modulation (O and M respectively on Figure 2.46). It will always be equal to the modulation frequency, but as illustrated on Figure 2.46 the beatnote from two neighbouring M lines will be at a frequency equal to $\mathrm{FSR} - 2 \times \nu_{\mathrm{mod}}$.

[9] A more detailed description of this process will be presented in the next chapter.

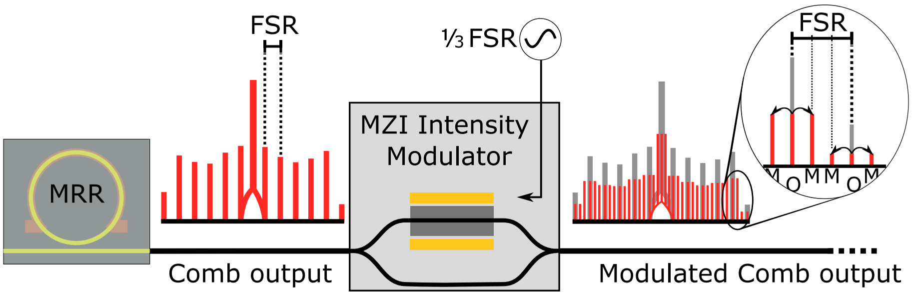

Figure 2.46: *Modulation setup used for electronic downconversion of the FSR beatnote. The entire comb is passed through a MZM run at a third of the FSR. Some smart caption.*

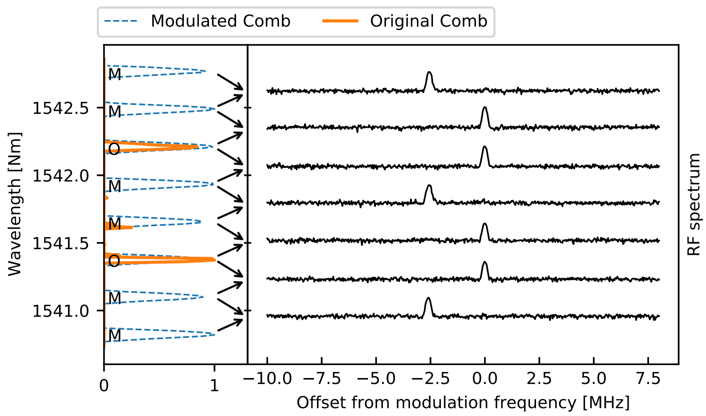

Figure 2.47: *Plot of multiple beatnotes between lines in the modulated comb, two at a time. We see that the beatnote between a original line (O) and a modulation generated line (M) is always the modulation frequency, in contrast to the beatnote between two modulated lines originating from different original lines.*

With this technique we are able to see from the bottom plot of Figure 2.45 that the "MvsM" beatnote changes 1.1 MHz between the high and low power comb states, which corresponds to the FSR getting 1.1 MHz larger when going from the high to the low power state. We also see that the "MvsM" beatnotes appear wider than the "OvsM" beatnote, however these beatnotes are the sum of all the beatnotes across all the comb lines. Figure 2.47 instead shows the RF spectra if we isolate one pair of lines at a time. Here we see no discernable difference between the "OvsM" and "MvsM" linewidths, so further work is needed to identify the underlying issue seen in the bottom plot of Figure 2.45.

The state change jumps shown on the top plot of Figure 2.45 can be avoided by changing the comb power locking setpoint to one of the two comb power levels, but this must be regularly changed as conditions in the laboratory change. This is shown in Figure 2.48, where the air temperature and the setpoint changes necessary to avoid jumps appear to be weakly correlated.

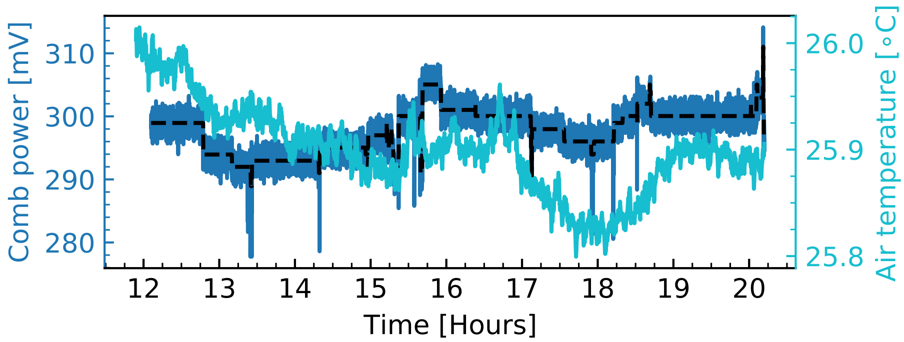

Figure 2.48: *Comb power and temperature over an 8 hour period. The blacked dashed line indicates the setpoint. The setpoint is changed every time the comb power starts jumping like in Figure 2.45. There is a correlation between the setpoint changes and the air temperature.*

Frequency Stability

While the instabilities and comb state jumps listed above are undesired, they are not necessarily detrimental depending on the use case for the comb. We therefore also characterize the short term frequency stability of the comb lines. As mentioned previously, the lines should in theory all inherit the properties of the pump laser. In order to confirm this, we use the same setup as before for heterodyne beatnote measurements (see Figure 2.44). But this time we are interested in how the beatnote frequency evolves over time. For metrological purposes the long term frequency stability can be more interesting than the short term frequency stability. This is because if the beatnote frequency is stable over long times, then we can more accurately determine the mean frequency through averaging as the uncertainty of the mean will decrease as:

$$\sigma_{mu} = \frac{1}{\sqrt{N}}, \tag{2.5.1}$$

where N is the number of repeated measurements. The problem for frequency stability measurements is that most systems are dominated by noise types which prevent the variance from converging, and thus repeated measurements will not give increasingly better estimates of the mean value. Instead different types of variance estimations have been developed, which help characterize frequency references by providing information about what types of noise dominate at different timescales. A list of them can be found in [74], but the most famous and simplest is the Allan variance [75], which calculates the average squared distance between two time-adjacent measurements:

$$\sigma(\tau)^2 = \frac{1}{2(M-1)} \sum_{i=1}^{M-1} (y(\tau)_{i+1} - y(\tau)_i)^2,$$

where M is the number of measurements, and y is a measurement averaged over τ seconds. In practise one obtains as many short measurements as possible, i.e.

74. Riley et al., *Handbook of Frequency Stability Analysis*(2008)
75. Allan, "Should the Classical Variance Be Used as a Basic Measure in Standards Metrology?"(1987)

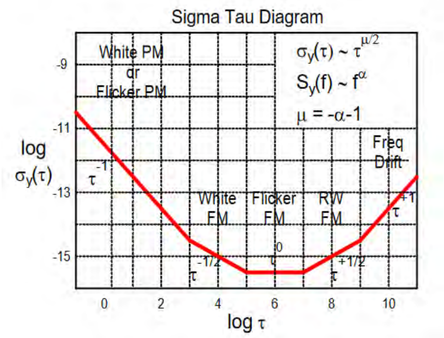

Figure 2.49: *Illustration of how the slope of the Allan variance is determined by which noise type is dominant. Here S_y indicates the power spectral density. Image is from [74]*

with as low τ as possible, and longer measurements can then be reconstructed by dividing the data into blocks of length τ and calculating the average of each block. By looking at how $\sigma(\tau)$ changes as a function of τ we can determine what noise source is dominant at what timescale simply by looking at the slope as shown on Figure 2.49. More advanced variance estimators have been developed from Allan variance which provide a better statistical confidence, or an increased ability to distinguish white phase noise from white flicker noise. Common for all these variances is that they are made to agree with the standard variance for white frequency noise, i.e. Gaussian distributed frequency spreads where each point is independent from the previous one. In this case the Allan deviation decreases as $\frac{1}{\sqrt{\tau}}$ just like the standard uncertainty of the mean.

To investigate the frequency stability of our generated comb, and whether the modulation process affects the frequency stability, we measure four different beatnotes:

- Tunable reference laser vs an original comb line from the modulated comb.
- Tunable reference laser vs a modulation comb line from the modulated comb.
- Tunable reference laser vs a comb line from the original comb
- Fixed frequency, ultra stable reference laser vs the tunable reference laser.

Which is also summarized in Figure 2.50. We then calculate the overlapping Allan deviation for each dataset and plot it on Figure 2.51. The tunable reference laser used is identical to the pump laser (CoBrite NX). As any comb lines should inherit the performance of the pump laser we therefore assume they both contribute equally to the measured frequency (in)stability which allows us to divide the calculated Allan deviation by $\sqrt{2}$. The fixed frequency laser is a NKT Koheras BasiK E15 module ([76]) and is used to measure the stability of tunable reference laser, which will also give us the stability of the pump laser itself. While Figure 2.51 shows a small variation in the Allan deviation at short timescales (low τ), they do overlap from 1 ms and onwards indicating

76. NKT, “Koheras Basik Accessed on 2021/08” (2014)

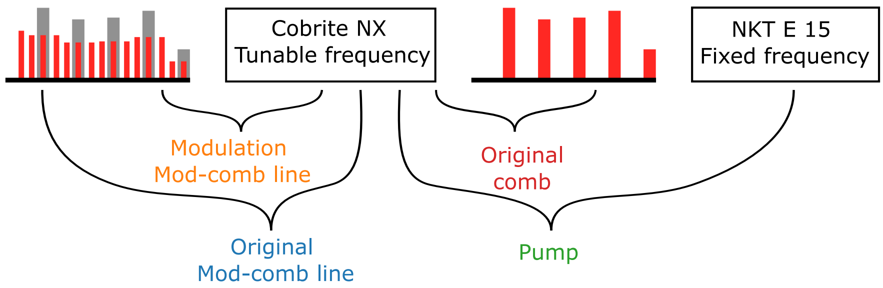

Figure 2.50: *Illustration of the different beatnotes measured to investigate the frequency stability of the generated comb. The colours and names refer to Figure 2.51.*

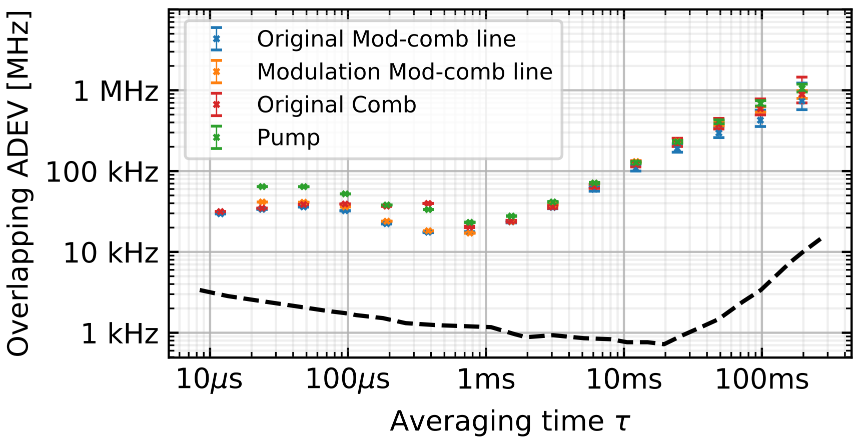

Figure 2.51: *Allan deviation stability of different comb lines, with and without the additional $\frac{1}{3}$ FSR modulation. The reference for the blue, orange and red lines is an identical laser so they have been divided by $\sqrt{2}$. The reference for the green line is a much more stable, fixed frequency laser, so the result has not been divided. The dashed line indicates the stability of the reference laser as specified by the manufacturer.*

that the comb lines do inherit the stability of the pump laser, and the modulation process does not generate additional frequency noise. Note that the blue, red and orange trace have been divided by $\sqrt{2}$, but since they coincide with the green trace it confirms that the tunable laser used to pump the comb, and the tunable laser used to measure the beatnotes, are identical in stability. The dashed line shows the stability of the E15 laser as given by NKT[77].

Summary

In conclusion, even though we can maintain a phase-locked comb state for several hours, and even days with automatic relocking, there are several instabilities we cannot control. Firstly we see a degeneracy in the comb power which allows for two different heating voltages to produce the same total comb

77. Photonics, "Analysis of Laser Frequency Stability Using Beat-Note Measurement"(2013)

power (when measuring half the comb after a SPF). These two different heating voltages cause an absolute shift in the comb frequency which is expected due to the frequency shift of the chip resonances. Secondly there exists distinct comb power states in which the device prefers to operate. Trying to stabilize it at a comb power between these two states will cause the feedback system to drive the heater voltage up and down and force a jump between the comb states which is associated with comb FSR changes. Further work is necessary to identify whether both types of jumps affect both the absolute frequency and the line spacing. Lastly we find that the comb states are not reproducible and have very different comb line amplitude stabilities. However when investigating the frequency stability we see that the comb lines inherit the stability of the pump laser and the additional process of modulating the comb does not add any additional instabilities, which will be important in the following chapter.

Chapter 3

Kerr combs for telecommunication

Since the launch of the world wide web in 1983, when the TCP/IP protocol was officially implemented, the internet has grown exponentially in size. The amount of traditional access points, such as computers and smartphones, reached 5.8 billion in 2018 and is projected to reach 8.7 billion by 2023[78]. On top of this, the number of internet-of-things devices such as fridges[79][10], is predicted to increase by 30 % every year!

To keep with with this ever growing demand for data access, the global annual internet traffic data between data centres has increased exponentially by a factor of 5×10^8 from 2 TB in 1987 to 1 ZB in 2017[83]. This has only been possibly due to constant improvements in fibre optical communication technology, where the goal is to push as much data as possible from A to B, preferably as energy efficiently as possible. In this chapter we will show one way of using chip based frequency combs to transfer extremely large amounts of data simultaneously using only a single light source.

The basis of any optical communication is data modulation. Data is written onto the light by modulating either the phase, frequency, amplitude, or a combination of these. In the simplest case we can imagine on-off keying, in which *on* represents a `1` and *off* represents a `0`, which transmits one bit of information at a time. The state of the light, in this case on or off, is called the symbol, and the symbol rate indicates how fast the state can be changed. The symbol rate is also called the baud rate. For most applications the baud rate is twice the modulation rate, i.e. twice the frequency of the RF signal driving the modulator, typically denoted R. This means the symbol bandwidth will be equal to the spectral bandwidth of the frequency modulation. More advanced modulation schemes exist, where one uses a mixture of a sine and cosine wave, at different amplitudes. This is called quadrature amplitude modulation (QAM), or IQ modulation and while it can perfectly replicate frequency or phase modulation, it is mostly used to increase the number of transmitted bits per symbol. The IQ plane is divided into $2^{N_{\text{bits}}}$ distinct points, which means each symbol can represent N_{bits}. The data rate is then given as $N_{\text{bits}} \cdot R$. It is very common to use 32,64 or 256 QAM corresponding to $N_{\text{bits}} = 5, 6, 8$

78. Annual et al., *White Paper Cisco Public*(2018)
79, *SamsungSmartFridge*()
83. Jones, “How to Stop Data Centres from Gobbling up the World’s Electricity”(2018)

[10] but also water bottles[80], batteries[81], cat lavatories[82], and much... much... more.

respectively, but as much as 4096 QAM has been demonstrated[84]. Higher order modulation requires a better signal to noise ratio (SNR), which means more optical power. Unfortunately more power leads to stronger nonlinearities in the transmission fibre, which negatively affects the data transmission. Increasing the baud rate, is the other option for increasing data transmission, but this requires modulating and sampling at higher frequencies. State of the art modulators are currently limited at 100 GHz bandwidth[85], while waveform generators cannot do more than 100-200 GHz[86],[87]. And while modulators could potentially reach 500 GHz[88] in the future, going beyond that will hit the hard limit of the electrons mobility. A simpler way of increasing data transmission is by using multiple channels in parallel. This can either be achieved by sending data through individual fibres, or by sending data through the same fibres, but in different states that will not interfere with each other. A good example of this is PDM, which simply data modulates the light in two orthogonal polarizations, effectively increasing the data rate by two. Another popular method is SDM, which uses different spatial paths, either through different cores in a multicore fibre, or through different, higher order fibre modes[17]. The limit of space division multiplexing (SDM) is only the cross talk between channels.

One last way is to utilize the wide transparency window in optical fibres from 1260 nm to 1675 nm to do WDM where there is minimal absorption. It is straightforward to divide the range up into several distinct frequency bands, and transmit independent data in each band. WDM is connected with the modulation, in the sense that the channels cannot be spaced closer than the modulation frequency without avoiding channel interference. This is illustrated in the top part of Figure 3.1. Typically WDM systems are created by interleaving individual lasers, but because the lasers will drift randomly and independently, the modulation rate must be smaller than the line separation. This empty channel space is called the guard band, and limits the spectral efficiency of a WDM system. A state of the art extended cavity laser (ECL) system used for data transmission experiments drifts up to 5 GHz per year[71]. One further limitation of WDM systems is the technology available to amplify the signals. It is common to only use a small subset of the full transmission window, typically denoted the C and L band, ranging from 1525 nm to 1650 nm, where EDFAs can be used efficiently.

In summary: The transmitted data rate in bit/s, if all of these methods are used simultaneously,will be given as:

$$\text{rate} = \overbrace{n_{\text{WDM}} \cdot m_{\text{SDM}} \cdot n_{\text{PDM}}}^{\text{number of channels}} \times \overbrace{\text{baudrate} \cdot \text{bits/symbol}}^{\text{data per channel}}, \tag{3.0.1}$$

where:

84. Terayama et al., "4096 QAM (72 Gbit/s) Single-Carrier Coherent Optical Transmission with a Potential SE of 15.8 Bit/s/Hz in All-Raman Amplified 160 Km Fiber Link" (2018)
85. Xu et al., "High-Performance Coherent Optical Modulators Based on Thin-Film Lithium Niobate Platform" (2020)
86. Yamazaki et al., "IMDD Transmission at Net Data Rate of 333 Gb/s Using over-100-GHz-bandwidth Analog Multiplexer and Mach-zehnder Modulator" (2019)
87. Nagatani et al., "A Beyond-1-Tb/s Coherent Optical Transmitter Front-End Based on 110-GHz-Bandwidth 2:1 Analog Multiplexer in 250-Nm InP DHBT" (2020)
88. Schmidt et al., "Data Converter Interleaving: Current Trends and Future Perspectives" (2020)
17. Rademacher et al., "10.66 Peta-Bit/s Transmission over a 38-Core-Three-Mode Fiber" (2020)
71. IdPhotonics, *Mainframe Series CoBriteMX Lasers Accessed on 2021/04* ()

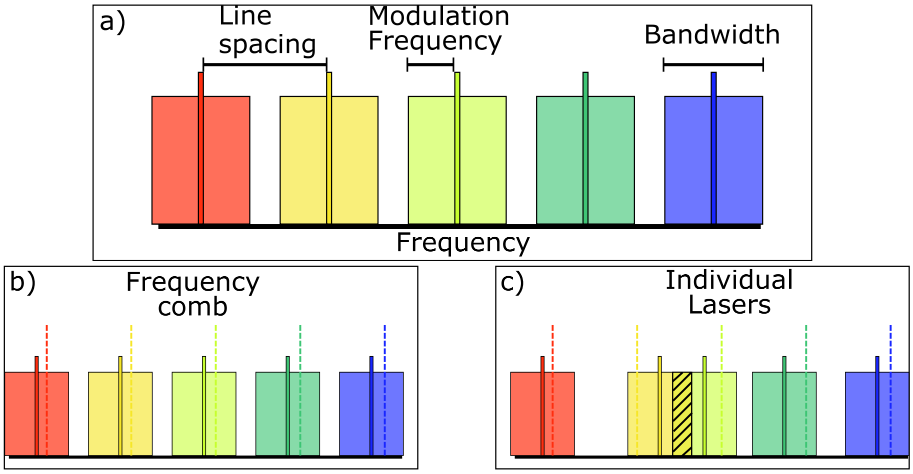

Figure 3.1: *Principle behind WDM data transmission. a) Shows an equidistant grid of frequency lines, separated by the line spacing. The shaded area represents the modulated area. If these areas overlap there will be crosstalk between the channels. In the case of drift, a grid made by a frequency comb will retain its line spacing (b), whereas a grid made of individual lasers can potentially begin to overlap (c).*

- n_{WDM} is the number of wavelength channels, restricted by the EDFA efficiency range, the modulation frequency, and the size of the guard bands.
- m_{SDM} is the number of spatial channels, only restricted by the amount of available physical channels.
- n_{PDM} is the number of polarization channels, and is rarely more than two.
- baudrate is the number of symbols per second. This is limited by the available equipment but cannot be larger than the WDM channel spacing.
- bits/symbol depends on the modulation format, which is limited by the available SNR. As higher order formats require more optical power this is also limited by the required transmission distance, as nonlinear effects cause signal degradation.

There are many more factors to take into account when adjusting these parameters, but they are outside the scope of this thesis.

3.1 Combs for telecommunication

Frequency combs lend themselves naturally to WDM, as their frequency domain form is an equidistantly spaced grid of narrow frequencies. Furthermore, as the comb lines are traced to a single laser, any drift will be identical across all lines, as seen on Figure 3.1. This significantly reduces the requirement of guard bands and allows for higher modulation rates, and thus higher data transmission rates.

For this purpose, many types of frequency combs have be used, such as EO combs[19] or fibre based combs[89]. But MRR based combs have one large advantage: they are directly integrable with existing photonic circuits and manufacturing procedures. It is because of this that data transmission with dissipative kerr soliton micro combs have gathered a lot of attention in the past years[18],[90]–[92]. For most cases, the number of WDM is restricted by the effective bandwidth of the amplifiers, and the baud rate is limited by the bandwidth of the IQ modulators and the linespacing. The number of SDM channels is then only limited by the power in each comb line, as each additional SDM channel reduces the available optical power, and thus the SNR. The dark pulse kerr combs we have seen in the previous chapters all have a line spacing around 100 GHz, far beyond the capabilities of the 32 Gbaud transmission systems we have available at Technical University of Denmark (DTU) (32 Gbaud takes up 32 GHz of the channel total channel width, and is thus much lower than the 100 GHz line spacing.). In order to optimize the number of channels, we therefore employ a small trick by modulating the entire comb to create additional comb lines and reduce the comb line spacing.

Capacity scaling with comb lines

To see the advantage of this we need to briefly discuss theoretical data capacity. The fundamental data transmission capacity C for a single channel only influenced by white Gaussian noise, can be expressed as the Shannon-Hartley theorem, first published in 1947[93]:

$$C = R \cdot \log_2\left(1 + \frac{P_{\text{Signal}}}{P_{\text{Noise}}}\right) = R \cdot \log_2(1 + \text{SNR}) = R \cdot \log_2\left(1 + \frac{R_{\text{ref}}}{R}\text{OSNR}\right), \tag{3.1.1}$$

where R is the channel bandwidth, R_{ref} is the reference bandwidth of 0.1 nm, and (O)SNR is the (optical) signal-to-noise-ratio.[11] If we now assume that a comb will not need any guard bands, then we can set the bandwidth R of each channel equal to the comb line spacing. This spacing can be found by

19. Hu et al., "Single-Source Chip-Based Frequency Comb Enabling Extreme Parallel Data Transmission" (2018)
89. Puttnam et al., "2.15 Pb/s Transmission Using a 22 Core Homogeneous Single-Mode Multi-Core Fiber and Wideband Optical Comb" (2015)
18. Marin-Palomo et al., "Microresonator-Based Solitons for Massively Parallel Coherent Optical Communications" (2017)
90. Pfeifle et al., "Coherent Terabit Communications with Microresonator Kerr Frequency Combs" (2014)
91. Fülöp et al., "High-Order Coherent Communications Using Mode-Locked Dark-Pulse Kerr Combs from Microresonators" (2018)
92. Corcoran et al., "Ultra-Dense Optical Data Transmission over Standard Fibre with a Single Chip Source" (2020)
93. Shannon, "Cominunication Theory in the Presence of Noise" (1949)

[11] The conversion between OSNR and SNR stems from difference in definition. SNR is the total signal power divided by the total noise power, while optical signal to noise ratio (OSNR) is the total signal power divided by the noise power in the reference bandwidth:

$$\text{SNR} = \frac{P_{\text{Signal}}(R)}{P_{\text{Noise}}(R)} \neq \frac{P_{\text{Signal}}(R)}{P_{\text{Noise}}(R_{\text{ref}})} = \text{OSNR}$$
$$\text{SNR} = \frac{P_{\text{Signal}}(R)}{P_{\text{Noise}}(R)} = \frac{P_{\text{Signal}}(R)}{P_{\text{Noise}}(R_{\text{ref}})\frac{R}{R_{\text{ref}}}} = \frac{R_{\text{ref}}}{R}\text{OSNR}$$

taking the total comb bandwidth BW and dividing by the number of comb lines N_{comb}:

$$R = \frac{BW}{N_{\mathrm{comb}}}. \tag{3.1.2}$$

We can then find the total data transmission capacity for the comb, by summing over all comb lines:

$$C_{tot} = \sum_{i}^{N_{\mathrm{comb}}} C_i = N_{\mathrm{comb}} \cdot \frac{BW}{N_{\mathrm{comb}}} \log_2 \left(1 + R_{\mathrm{ref}} \frac{N_{\mathrm{comb}}}{BW} OSNR \right). \tag{3.1.3}$$

For telecommunication the spectrum of the comb will be equalized to the power of the lowest comb line P_{min}, and the OSNR for each channel can therefore be approximated as $P_{\mathrm{min}}/P_{\mathrm{Noise}}$.

For MRR based micro combs where the losses are much lower than the coupling coefficient to the cavity, it was shown in [94] and [41] that P_{min} scales inversely with the number of lines within some power cutoff:

$$P_{\mathrm{min}} \approx K \frac{P_{\mathrm{pump}}}{N_m athrmcomb^2}, \tag{3.1.4}$$

where P_{pump} is the optical power used to pump the comb, and K is a proportionality constant determined by the power cutoff, i.e. $K = 3.53$ for $P_{min}/P_{max} = -3\,\mathrm{dB}$. This means we can express the OSNR as a function of pump power and number of comb lines:

$$OSNR = \frac{P_{\mathrm{min}}}{P_{\mathrm{noise}}} = K \frac{P_{\mathrm{pump}}}{N_{\mathrm{comb}}^2 P_{\mathrm{noise}}}. \tag{3.1.5}$$

If we insert this scaling into the total capacity equation we arrive at:

$$C_{tot} = BW \log_2 \left(1 + R_{\mathrm{ref}} \frac{N_{\mathrm{comb}}}{BW} K \frac{P_{\mathrm{pump}}}{N_{\mathrm{comb}}^2 P_{\mathrm{noise}}}\right) \tag{3.1.6}$$

$$= BW \log_2 \left(1 + R_{\mathrm{ref}} \frac{K}{BW} \frac{P_{\mathrm{pump}}}{N_{\mathrm{comb}} P_{\mathrm{noise}}}\right). \tag{3.1.7}$$

The consequence of this is that the total capacity will favour a comb with a large line spacing, as long as the data modulation equipment is able to match the spacing.

One trick is to utilize this by creating a comb with a line spacing far larger than the possible data modulation rate and then intensity modulate this comb in order to increase the number of lines. This will decrease the power and thus the OSNR of each comb line, but it will also reduce the linespacing. The OSNR per line kan then be expressed as:

$$OSNR = K \frac{P_{\mathrm{pump}}}{N_{\mathrm{comb}}^2 P_{\mathrm{noise}}} \cdot \frac{1}{N_{\mathrm{mod}} 2L}, \tag{3.1.8}$$

where N_{comb} is the number of comb lines in the MRR generated comb, N_{mod} is the number of lines generated by the modulator, and $2L$ is the loss associated

94. Bao et al., "Nonlinear Conversion Efficiency in Kerr Frequency Comb Generation" (2014)
41. Helgason et al., "Dissipative Solitons in Photonic Molecules" (2021)

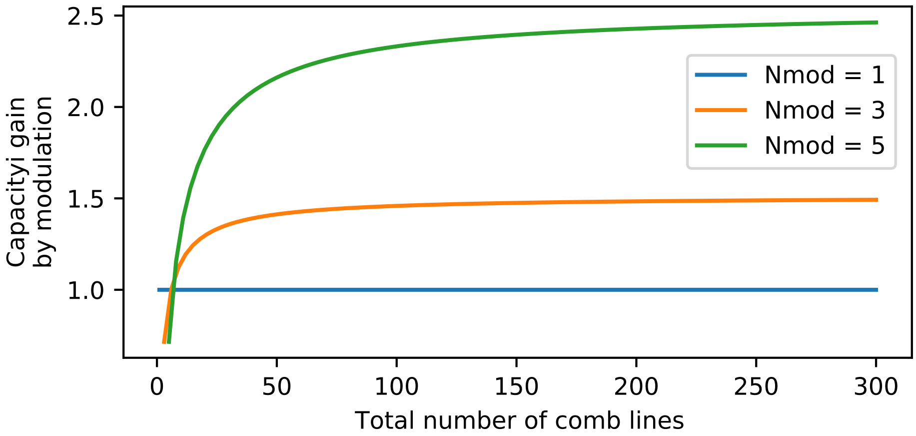

Figure 3.2: *Scaling of total capacity as a number of total comb lines. The input losses of the modulator L are set to 3 dB. It is clear that it is advantageous to modulate the comb after generating it.*

with the modulator. The factor of two comes from the inherent loss in an intensity modulator, and L accounts for any input losses. The total number of lines in the comb, after this modulation is then $N_{\mathrm{tot}} = N_{\mathrm{comb}} \cdot N_{\mathrm{mod}}$. The channel bandwidth R then become:

$$R == \frac{BW}{N_{\mathrm{tot}}} = \frac{BW}{N_{\mathrm{comb}} \cdot N_{\mathrm{mod}}}, \tag{3.1.9}$$

with the total capacity then becoming:

$$\begin{aligned} C_{tot} =& N_{\mathrm{comb}} N_{\mathrm{mod}} \frac{BW}{N_{\mathrm{comb}} N_{\mathrm{mod}}} && (3.1.10)\\ & \log_2\left(1 + R_{\mathrm{ref}} \frac{N_{\mathrm{comb}} N_{\mathrm{mod}}}{BW} K \frac{P_{\mathrm{pump}}}{N_{\mathrm{comb}}^2 P_{\mathrm{noise}}} \cdot \frac{1}{N_{\mathrm{mod}} 2L}\right) && (3.1.11)\\ =& BW \log_2\left(1 + \frac{R_{\mathrm{ref}}}{BW} \frac{K}{2L} \frac{P_{\mathrm{pump}}}{N_{\mathrm{comb}} P_{\mathrm{noise}}}\right). && (3.1.12) \end{aligned}$$

While this equation looks strikingly similar to Equation 3.1.7, it is important to note that it is independent of N_{mod}, under the assumption that we can modulate each comb line into N_{comb} lines with equal amplitude. This way the total capacity will increase if we decrease N_{comb} simply because the optical power per line scales as $\frac{1}{N_{\mathrm{comb}}^2}$, and the optical power reduction from modulation scales as $\frac{1}{N_mathrmmod}$. This is also shown in Figure 3.2 where the total capacity C_{tot} is plotted for 3 different modulation cases, with the total number of channels held constant.

SDM scaling

From a maximum capacity viewpoint capacity viewpoint the number of possible SDM channels will depend on the OSNR, as it will decrease linearly with the number of SDM channels. The total capacity can then be expressed as:

$$C_{tot}^{\mathrm{SDM}} = N_{\mathrm{SDM}} BW \log_2 \left(1 + \frac{R_{\mathrm{ref}}}{BW} \frac{K}{2L} \frac{P_{\mathrm{pump}}}{N_{\mathrm{comb}} P_{\mathrm{noise}} N_{\mathrm{SDM}}} \right). \tag{3.1.13}$$

Because the total capacity scales as the logarithm of the OSNR, it means not all OSNR is created equally and it is more advantageous to lower the OSNR if it increases either the number of WDM or SDM channels. With WDM being limited by the total bandwidth and current EDFAs, and modulation format being limited by the maximum amount of power that can be sent through a fibre, SDM could be the currently most efficient available scaling dimension. Especially because SDM channels are the cheapest to scale to larger numbers, due to the relatively low cost increase of laying additional fibres [95], and that fibre companies today can pack over 800 fibres in a 20 mm diameter cable.

3.2 Petabit Transmission Experiment

Most of the testing and characterization of the MRRs presented in this thesis was done at the Niels Bohr Institute (NBI). In order to characterize the devices in a data transmission experiment, we had to take down the chip setup and set it up again 10 km away at the photonics laboratory at DTU. The only hardware that was transferred was the chip and the RedPitayas used as locking circuits. It is truly a testament to the overall robustness of the source that it only took a few hours to setup the comb.

The main goal of the experiment was to transmit as much data as possible through a single fibre using the MRR based dark pulse comb described in the previous chapter as a source. The comb had an FSR of 105 GHz which was decreased to 35 GHz through intensity modulation. We used a 32 Gbaud dual polarization IQ modulation system and a spectral bandwidth of 9 THz from 1530 nm to 1600 nm to transmit data 7.9 km through all 37 cores of a multicore fibre. This type of full system level experiment showcased the potential of chip scale sources, both with respect to the beneficial optical properties, but also with the general operation of the device, and source as a whole. While the previous chapter revealed a few stability issues with the dark pulse comb platform, which should be investigated and improved, the fact that the comb could be used to perform 8251 measurements, consisting of 223 wavelength channels through 37 fibre cores, demonstrates how mature the technology is. The systems experiment itself combined many methods and technologies from several different active areas of research. Spanning from advanced digital signal processing (DSP) with probabilistically shaped modulation formats, to the intricate fibre fabrication of the multicore fibre itself. It is beyond the scope of this thesis to go into full detail with all the subjects, however for completeness, the experiment and all the relevant parameters will be described here.

Experimental setup

The experiment can be divided into four distinct parts:

95. Winzer, "Chapter 8 - Transmission System Capacity Scaling through Space-Division Multiplexing: A Techno-Economic Perspective" (2019)

- The source, which provides the light used to carry the data.
- The transmitter, which loads data onto the source and conditions it for transmission.
- The link, which represents the transmission from sender to receiver.
- The receiver, which receives, conditions and extracts the transmitted data.

In the following, each part will be described individually, to give a complete idea of the transmission experiment performed.

Source

The source in our experiment is a dark pulse Kerr comb generated by a S_3N_4 MRR with normal dispersion and 105 GHz FSR. The setup is sketched in Figure 3.3. The MRR is placed on a setup identical to the one described in Figure 1.5(b) with a chip placed on a temperature controlled base and light guided on and off using lensed fibres. The micro heater is controlled through DC contact probes which are not shown in Figure 3.3.

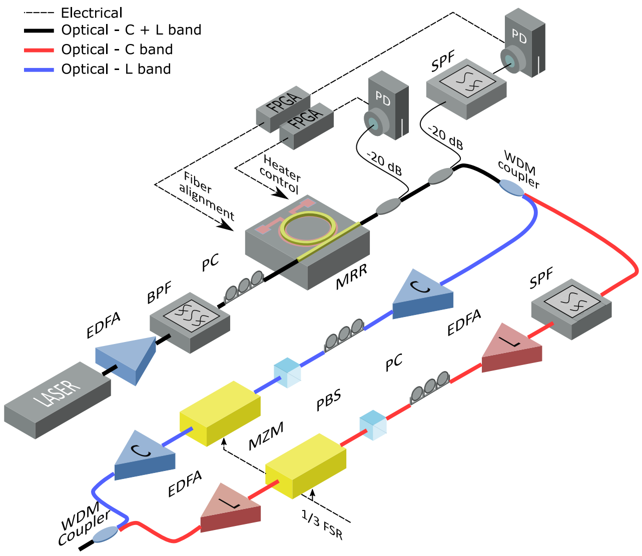

Figure 3.3: *Experimental setup of the source, including all used amplifiers and splitters/combiners.*

The pump laser is a id-photonics CoBrite type NX with an upgraded linewidth of 10 kHz and an output power between 8 dBm to 16 dBm[71]. During the experiment the pump is fixed around 1562 nm using the provided software. It is therefore not an absolute measure of frequency and is adjusted 1 GHz to 2 GHz over the course of a week, in order to compensate from small drifts due to changing laboratory conditions. This is not an issue for a data transmission experiment, where frequency changes on that scale are can be compensated in

71. IdPhotonics, *Mainframe Series CoBriteMX Lasers Accessed on 2021/04* ()

the DSP process. The first part of the setup up until the first WDM coupler, is the generation and stabilization of the initial comb, and is identical to the setup shown in the previous chapter (Figure 2.23). The pump is amplified in a high power EDFA to 32 dBm and passed through a narrowband optical BPF in order to filter out the ASE of the EDFA. PCs are used to match the input polarization to the orientation of the chip waveguide before the light enters the chip. Right after the chip, a −20 dB coupler splits off a small part of the light and captures it on a 1 GHz photodiode used for the fibre realignment system explained in Section 2.5. Another −20 dB coupler splits off another small portion of light and uses an optical SPF to filter out the pump. The remaining light is captures on a 1 GHz photodiode.

A typical spectrum of the comb light at this stage is plotted on Figure 3.4 (Top). The C and L band have been indicated to showcase how much of the standard telecommunication bands the comb covers. At 32 dBm pump power the comb has −13 dBm power in the lowest line and a conversion efficiency (converted power/pump power) of 13 %. Because we need around 0 dBm optical power for data transmission we need to amplify the comb. As ordinary commercially available EDFAs cannot cover both bands, me must split the comb light before amplifying it separately in the C and L bands. This is achieved with WDM couplers which split the light into the C band and L band, indicated in blue and red on Figure 3.3 respectively. A spectrum of the comb after the first amplification is shown on Figure 3.4 (Mid). Here the OSNR has also been calculated following the standard method of estimating the out-of-band noise. The spectrum has not been scaled to represent the actual power of the comb, as only a relative power measurement is necessary for OSNR estimation.

From the figure we clearly see the bandwidth limit of the C-band amplifier which cannot amplify below 1525 nm. In the C-band part of the spectrum we use a short pass filter to equalize the power of the pumped mode to the rest of the comb lines. Together with the finite rolloff of the WDM couples this means three lines in the middle of the spectrum are lost due to attenuation. After the first set of amplifiers the polarization is cleaned using a set of paddle wheels (PC) and two polarizing beam splitter (PBS). MZMs are then used to modulate the two parts of the spectrum separately at $\frac{1}{3}$ FSR as explained in the previous chapter. This triples the number of comb lines, at the cost of 10 dB optical power. 3 dB come from the inherent loss in the modulators, another 5 dB come from splitting the lines 1:3, the last 2 dB loss stem from input losses in the MZMs. This also reduces the line spacing and thus the channel bandwidth to ≈ 35 GHz.

After modulation we amplify the spectrum again to compensate for the modulation losses and combine the spectrum using another WDM coupler. The spectrum of our final source is plotted in Figure 3.4 (bottom) together with the calculated OSNR. In the C band, the OSNR is 10 dB lower than before the modulation, as expected, while it fluctuates a lot more in the L-band. This is due to a strong polarization mode dispersion (PMD) effect observed in the L-band EDFAs. The effect is mitigated, but not removed, by carefully adjusting the polarization before modulation. This compensates for the PMD observed in the first set of amplifiers, and mitigates the issue in the second set of amplifiers.

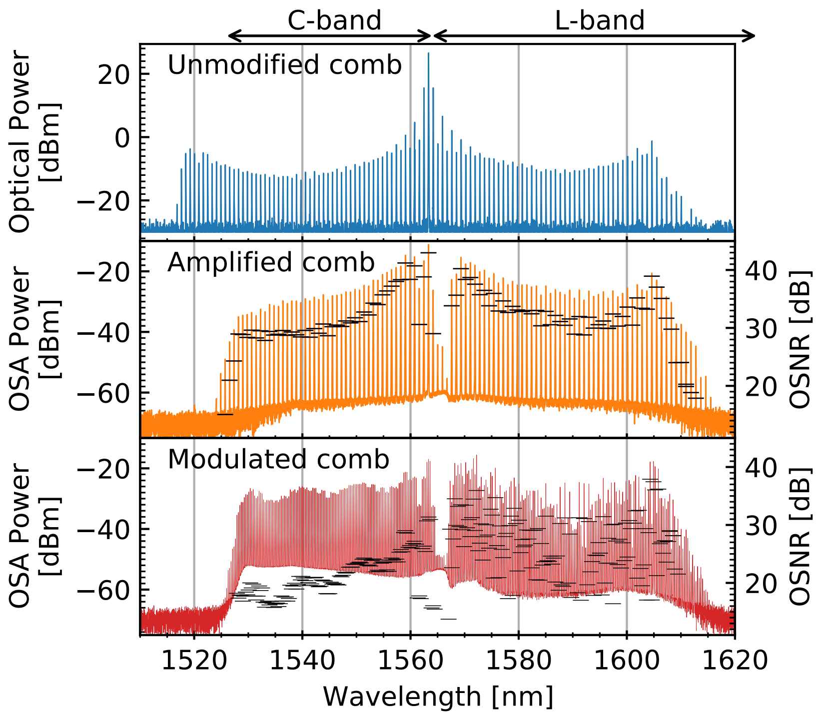

Figure 3.4: *Spectra of the comb source at various stages. Only the top plot is a measure of the full optical power.* ***Top*** *Spectrum of the comb as it is right off the chip* ***Mid*** *Spectrum of the comb after being amplified. Black lines show calculated OSNR.* ***Bottom*** *Spectrum of the comb after being modulated, Black lines show calculated OSNR. The OSNR is 10 dB lower than in the middle plot, as expected due to the loss of the modulation process.*

Transmitter

From the source the light enters the transmitter which supplies the data modulation using the setup depicted in Figure 3.5. The ideal scenario would be to load independent data on each channel, but due to the infeasibility of acquiring and setting up 223 transmitters and receivers, we opt to test one wavelength channel at a time. This is done by using a wavelength selective switch, which is a programmable, narrowband optical filter. We use the switch to split the light into three parts: Even and odd channels, and the channel under test (CUT). All even and odd channels are loaded simultaneously with two different sets of dummy data. This means no neighbouring channels are identical and allows us to identify any crosstalk issues between channels. The channel under test is loaded with the actual test data, and we perform the system experiment by iteratively designating each channel as the CUT.

The data modulation itself is done by first amplifying and filtering out polarization noise with the PBS. The light is then IQ modulated at 32 Gbaud (16 GHz) with a pseudorandom binary sequence generated by a 64 Gsample/s arbitrary waveform generator. Because the channels in the comb do not all have the same OSNR, we start each transmission by sending a short pilot set

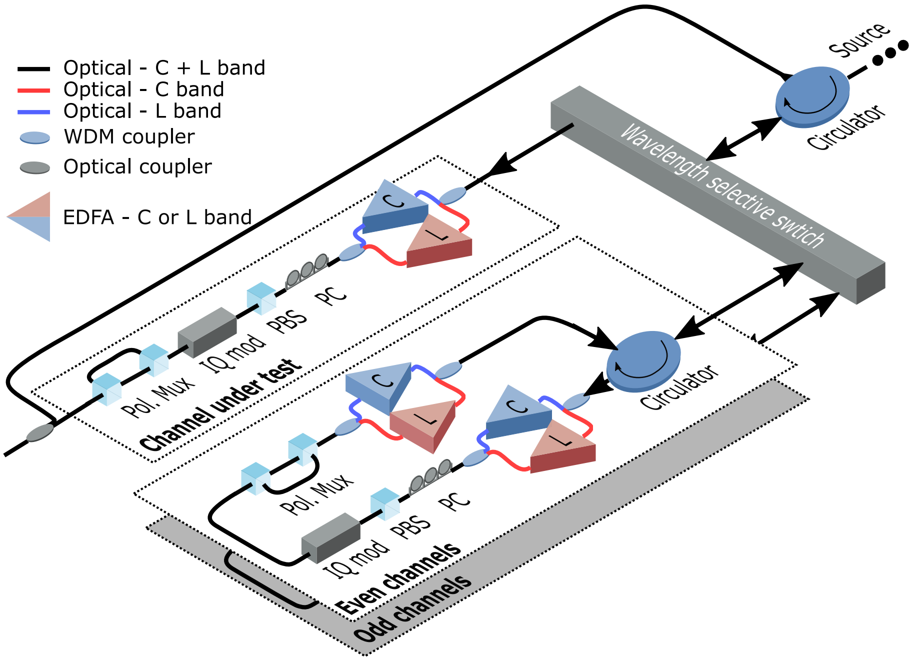

Figure 3.5: *Experimental setup of the transmitter which illustrates how the wavelength selective switch splits the data into three parts: The odd channels, even channels and the singular channel under test. The odd and even channels are recirculated through the wavelength selective switch to combine them to a single signal again.*

of data. On the receiver side we can determine the received SNR and make a decision about modulation formats based on this, similar to the work done in [96]. We modulate at two different formats: 64 QAM and 256 QAM with 50 % and 33 % low density parity check (LDPC) based forward error correction (FEC) code respectively.

We improve on this modulation format by using probabilistic constellation shaping based on the received SNR from the pilot data. The brief idea is that we distribute the bits we wish to transmit according to some probability distribution, most often making the lower amplitude modulation bits more probable as these are more resistant to noise. This becomes more clear when looking at Figure 3.6(a) and Figure 3.6(b) where the SNR makes it impossible to distinguish the outer symbols. If all symbols had been used with equal probability, the data would most likely have been unrecoverable on the receiver side. The probability shaping has therefore effectively limited the number of "noisy" symbols transmitted, which leads to a decrease in data rate, as we are not effectively using all symbols. On the other hand it allows us to change the modulation format with much finer granularity to match the SNR than by simply changing the modulation format and FEC overhead. The end result is a modulation scheme which can adapt much better to the varying SNR from channel to channel. While the adaptation requires a pre-transmission SNR measurement it will in general not change over time and thus only have to be

96. da Silva et al., "Experimental Characterization of 10x8 GBd DP-1024QAM Transmission with 8-Bit DACs and Intradyne Detection"(2018)

done once. For this experiment we restrict the adaptation to only modify the shaping between different wavelength channels and always measure the SNR on the fibre core with the largest loss. We do this because the SNR measurements constitute a significant overhead when we are only transmitting short amounts of data in order to test the system.

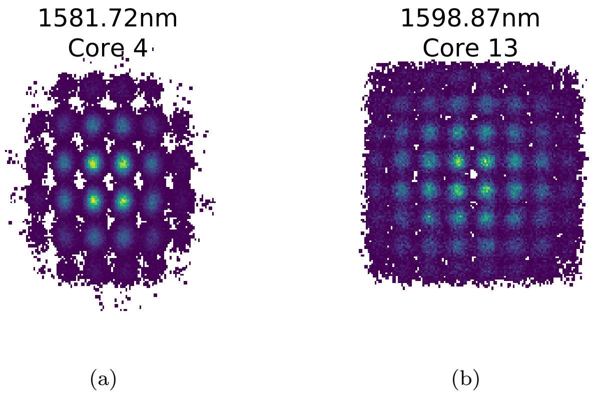

Figure 3.6: *Representative demodulated constellation shapes. The probabilistic shaping is clear in both constellations as brighter indicates a larger count.* ***a*** *64 QAM and* ***b*** *256 QAM.*

After data modulation the channels are polarization multiplexed using emulators with a large delay between the two polarizations to ensure decorrelation of the data modulated onto each polarization. The odd and even channels are amplified again before being circulated back into the wavelength selective switch (WSS) to be combined as a single signal. The WSS can also attenuate the individual channels and is used to flatten the output spectrum, with half of the attenuation applied at each pass through. The odd, even, and CUT are now combined in an ordinary 3 dB coupler and are ready for transmission. A spectrum of the light at this point can be seen in Figure 3.7 where we see that all the channels have been equalized in power, and data modulated as they are now spectrally broader.

Link

The link part of the setup takes the data modulated signal and transmits it through the 37-core multicore fibre as shown on Figure 3.8. Before transmission the signal is amplified to achieve a launch power of 9 dBm into each core. The signal is then split in a 1:64 splitter with only 37 of those channels being used. This is mainly due to available equipment, and essentially reduces the available SNR of each channel by 2.3 dB. The 37 core fibre has a measured crosstalk of less than −50 dB across the C and L band[97], but to ensure that crosstalk does not influence our experiment we decorrelate all 37 channels spatially by varying the propagation distance. A cross section of the multicore fibre is shown in Figure 3.8 After propagating 7.9 km through the fibre, the channels all enter a switch from which a single spatial channel is selected at a time.

97. Sasaki et al., "Single-Mode 37-Core Fiber with a Cladding Diameter of 248 Um"(2017)

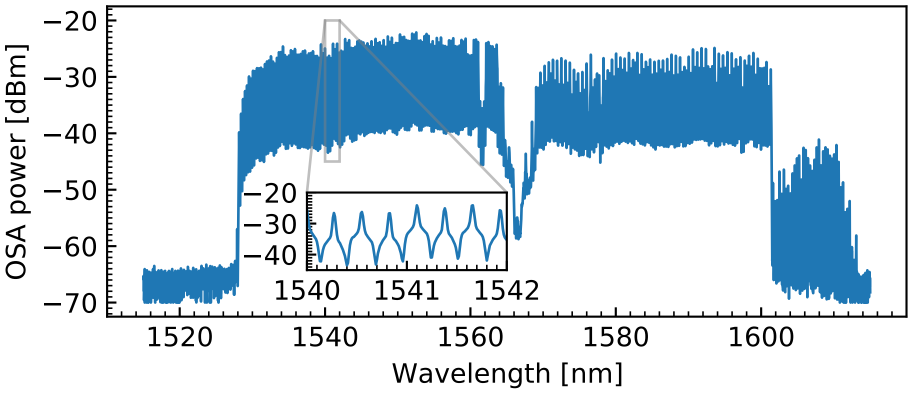

Figure 3.7: *Spectrum of the data modulated comb lines, right before transmission. The data modulation broadens the lines to fill almost the entire spacing.*

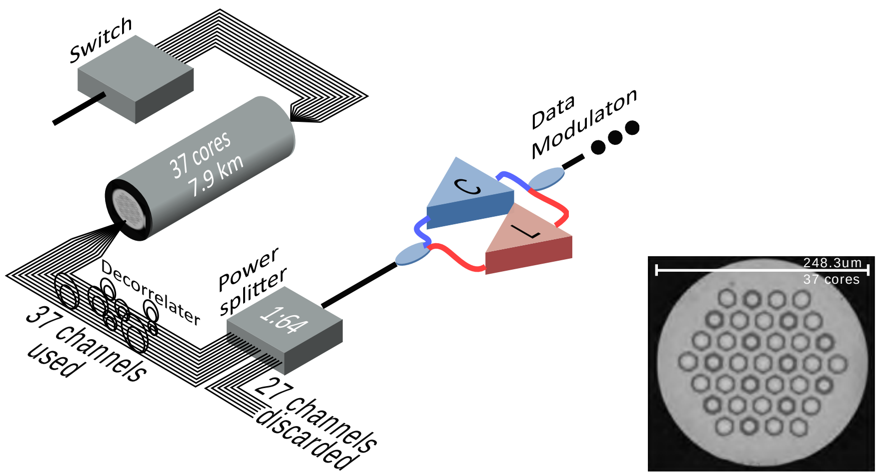

Figure 3.8: ***a*** *Experimental setup of the link, including fan-in and fan-out of the multi core fibre.* ***b*** *Cross section image of the multicore fibre, adapted from [97].*

Receiver

After the switch selects one of the 37 spatial channels, the channel is amplified in either a C band or a L band amplifier depending on the wavelength. It is then optically filtered using a BPF to isolate only the CUT and the two neighbouring channels, as shown on Figure 3.9. The detection scheme uses a local oscillator at 15 dBm, with −5 dBm of signal power in the channel under test. The detector is a dual polarization coherent receiver which outputs the two quadratures (I and Q) for each polarization (X and Y). The four signals are detected on 33 GHz photodiodes and 1 million samples are saved on a 80 Gsample/s digital storage oscilloscope for offline processing.

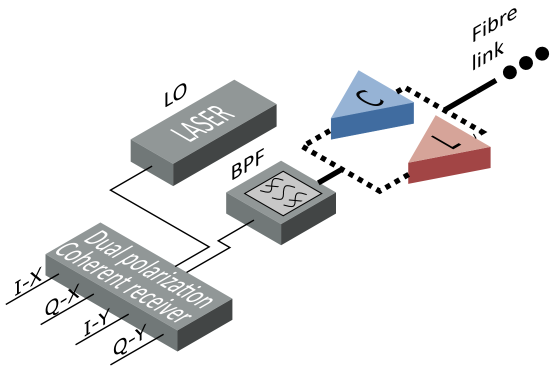

Figure 3.9: *Experimental setup of the receiver. The single spatial channel signal from the fibre link is amplified in either a C or L band EDFA depending on where in the wavelength band the channel under test (CUT) is. A band pass filter (BPF) isolates the CUT and its neighbouring channels before detecting them on a dual polarization coherent receiver.*

Digital signal processing and results

After saving the transmitted data the DSP is applied. The DSP flow is a research topic in and of itself and follows in line with similar experiments performed at the photonics department of DTU. For completeness the DSP process will be briefly described here but focus will be on analysis of the results.

The DSP starts with low-pass filtering, resampling and synchronizing the signals. A pilot aided radius directed adaptive equalization with a spacing of T/2 and 221 taps is used to demultiplex the polarization, compensate for chromatic dispersion, and mitigate the imperfect frequency response of the modulators. After this, a decision directed phase-locked loop corrects the frequency offset and performs the carrier phase recovery. Finally the signal is LDPC decoded to evaluate the post-FEC bit error rate (BER). The pilot overhead reduces the final data transmission rate and constitutes 4 %. The post-FEC BERs are shown in Figure 3.10. Most of them show 0 BER, but a hand full are nonzero. By assuming another outer layer of hard decision FEC it has been shown that BERs up to 5×10^{-5} can be reduced to 10^{-15} at the cost of 1 % increased overhead. This will get rid of most of the errors, and we discard the channels with BER above 5×10^{-5}.

The achieved transmission results are shown on Figure 3.11 as a function of wavelength channel. The left axis shows the achieved data bits per symbol per core for a single polarization. The blue and red points represent 64 QAM and 256 QAM modulation formats respectively. These fluctuate across the spectrum as they illustrate the fine granularity achieved by using the probabilistic shaping process. Each data point represents only one of the 37 cores, but because we did not change the modulation format between cores, all cores have achieved the same number of bits per symbol. To calculate the actual data rate of each wavelength channel we use the equation:

$$\text{Rate} = \text{baudrate} \cdot B_s \cdot N_{\text{pol}} \cdot N_{\text{cores}} \cdot OH_{\text{pilot}} \cdot OH_{\text{outerFEC}}, \tag{3.2.1}$$

where, B_s is the bits per symbol, N_{pol} is the number of polarizations, N_{cores} is the number of cores, and OH_{pilot} and OH_{outerFEC} is the inserted overhead

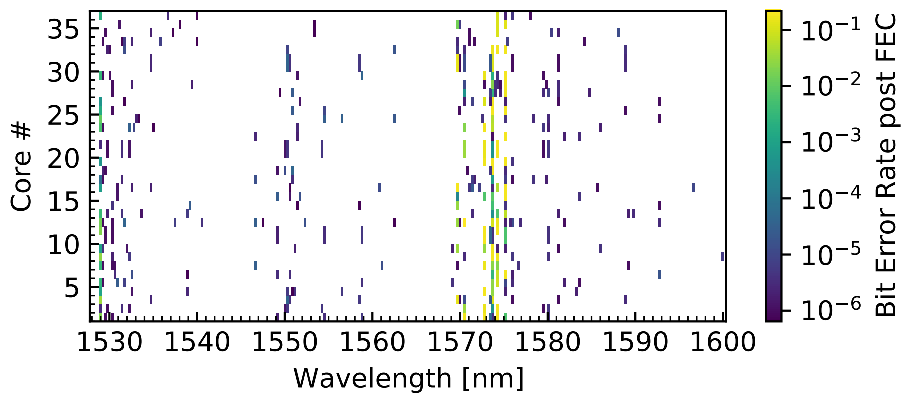

Figure 3.10: *Plot of calculated data transmission results as a function of core number and wavelength, most are white which indicates 0 Bit Error Rate.*

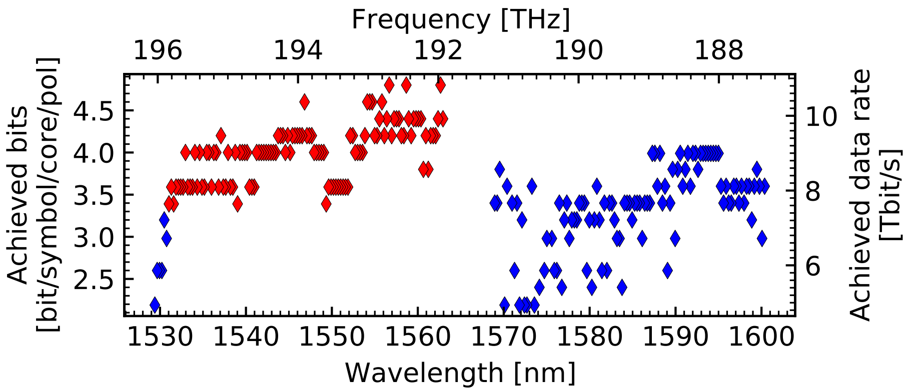

Figure 3.11: *Plot of calculated data transmission results. Blue points represent 64 QAM modulation and red points represent 256 QAM modulation.*

required for the pilot aided equalization and outer FEC, respectivly. In total this leads to:

$$\text{Rate} = 32\,\text{Gbaud} \cdot B_s \cdot 2 \cdot 37 \cdot \frac{1}{1.04}\frac{1}{1.01}, \tag{3.2.2}$$

which is shown on the right axis of Figure 3.11.

The channels in the L band all perform poorly, which matches the visual interpretation of the transmitted spectrum in Figure 3.7. From the original comb spectrum in Figure 3.4 (top) we see that there is no fundamental difference in the signal quality between the C band and the L band part of the comb. The poor performance is due to the EDFAs used. Even though they are a commercial product, L band EDFAs are a less mature technology and are not as good as the C band EDFAs. The difference between C band and L band EDFAs is mainly that the latter uses much longer nonlinear fibres which leads to them having lower gains and higher noise figures. The longer fibres

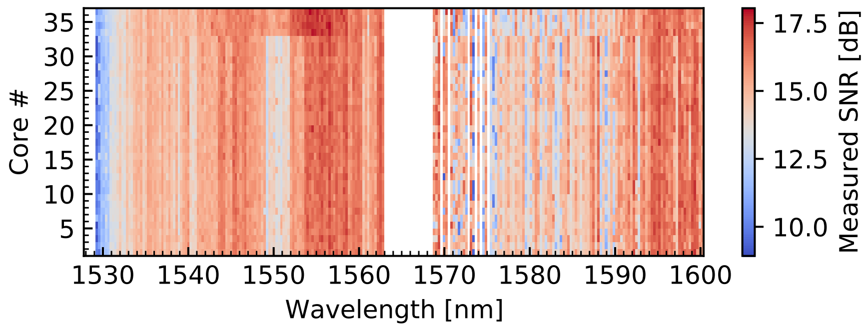

Figure 3.12: *Measured SNR of each wavelength channel for each of the 37 cores in the multicore fibre. The abrupt change at core number 32 is due to the last 5 cores being measured after the first 32, due to only having a 32 port fibre switch available.*

also proportionally increase other effects such as polarization mode dispersion. All this leads to a significant degradation in the signal quality every time we amplify the L band, and is visible just by comparing the spectra in Figure 3.4 from top to bottom.

This is the total net bit rate, or usable bit rate of each wavelength channel. The total capacity can now be calculated by simply summing across all wavelength channels:

$$R_{total} = \sum_{i}^{n_{wdm}} R_i = 1.84\,\mathrm{Pbit/s}. \tag{3.2.3}$$

This leads to a spectral efficiency in the range 1530 nm to 1600 nm of:

$$S = 211.3\,\mathrm{bit/Hz} = 25.9\,\mathrm{Tbit/nm}. \tag{3.2.4}$$

From the transmitted data we can also estimate the received SNR. This is shown on Figure 3.12 as a function of wavelength channel and core number. The sharp shift around core number 32 is because the switch used to choose a single core could only handle 32 connections. We therefore measured all the wavelength channels for 32 cores, and then for the remaining 37 cores. The adaptive shaping was estimated based on the first 32 cores, and not reestimated for the remaining 5. As this process took several days, it emphasizes the long term stability of the comb.

Figure 3.12 also shows a much larger variance in SNR in the L band compared to the C band. Before the experiment, the total loss between the power splitter before the fibre, and the output of the switch after the fibre, was measured. It varied between 25 dB to 28 dB across the cores. 18 dB are accounted for by the power splitter, 2 dB are from the fibre itself, and the remaining loss must be found in the decorrelation path, the coupling to and from the fibre and the final switch.

In relation to other experiments

When comparing transmission experiments, one cannot simply look at the total transmission rate. As an example, the group from NTT-Japan managed to do 10.66 Pbit/s in a 38-core, 3 mode fibre[17]. But their aim was to prove how much data the fibre could handle, and they therefore used the full SNR of their comb source for each spatial channel. In contrast the aim of our experiment was to transmit as much data as possible from a single light source, so we split the SNR evenly between the 37 spatial channels. Another MRR based transmission experiment was the one done by Marin-Palomo *et al.*[18], where they multiplexed together two bright soliton based combs with 100 GHz line spacing MRRs, in order to decrease the channel bandwidth to 50 GHz. However since every second wavelength channel is now generated by different MRRs, they can potentially drift slightly closer to each other. The interleaved comb lines are also not phase locked, so advanced things like joint DSP cannot be performed. The group of Victor Torres-Company have also presented transmission experiments done with dark pulse combs, but they have been limited to the C band only[91]. They had a very large line spacing of 203 GHz and only used 20 GHz of it for data modulation, but their goal was to prove the feasibility of using dark pulse combs for data transmission. Soliton crystals have also been used to transmit data in Australia[92], but while the soliton crystals can achieve very low spacings (48.9 GHz), they only barely cover the entire C band with almost no optical power in the L band.

We therefore believe we here have demonstrated the highest single MRR source data transmission rate. We have shown that dark pulse combs have an advantage over the bright solitons and soliton crystals because they have a high conversion efficiency with −13 dBm in the lowest comb line, which makes them able to easily supply 37 (and potentially much more) SDM channels simultaneously while covering both the C and L band. We have shown that the large line spacing can be overcome through intensity modulation at a loss of 10 dB, which is comparable to the power loss we would have if the comb had a natural line spacing of 35 GHz, as this would triple the number of lines and reduce the power in the lowest line a factor of $3^2 = 9$.

17. Rademacher et al., "10.66 Peta-Bit/s Transmission over a 38-Core-Three-Mode Fiber" (2020)
18. Marin-Palomo et al., "Microresonator-Based Solitons for Massively Parallel Coherent Optical Communications" (2017)
91. Fülöp et al., "High-Order Coherent Communications Using Mode-Locked Dark-Pulse Kerr Combs from Microresonators" (2018)
92. Corcoran et al., "Ultra-Dense Optical Data Transmission over Standard Fibre with a Single Chip Source" (2020)

Chapter 4

The acetylene frequency reference

Time references, and by extension frequency references, have been an integral part of the development of human civilization. From the first water clocks dating back to ancient Egypt, to the invention of the chronometer in the 18th century which connected societies previously separated by oceans. Today frequency references are a cornerstone of our modern system of units, as the second is the only SI unit which is still based on an experimental measurement. From the second, all other units are derived with the help of physical constants such as the Planck constant h or the elementary charge e.

The most common frequency references in modern day society are by far quartz crystal oscillators. They exist in almost every single electronic product and watch across the globe, and while they can be made incredibly stable, they are not an absolute reference. The frequency of a quartz oscillator is determined by the cut and size of the crystal. As they are mechanically constructed, their dimensions are chosen by calibrating them to existing frequency references. But how does one reference the first reference? There are many solutions to this problem, however very few of them are feasible. We could imagine a quartz crystal with every atoms position in the crystal lattice exactly specified. The physical properties of the atoms would then determine the dimensions of the crystal an absolute reference could be made. While it is not possible today to construct anything with such a degree of precision, the idea of using the properties of atoms is useful in another context as atoms themselves act as resonators when exposed to light. This was first discovered by Maxwell who observed the opposite effect where certain lamps would emit light with very distinct spectral lineshapes. Trying to interact with atoms using these types of lamps was difficult due to them emitting relatively broad spectral distributions. IT was with the invention of lasers that we were able to generate powerful "monochromatic" light sources, however while most lasers only emit light in a very narrow wavelength range, most are based off bulk semiconductor materials sandwiched together. The emission of a laser is therefore largely determined by the exact configuration of the materials, and it is therefore both impossible to produce two lasers which will emit at *exactly* the same frequency, and to guarantee that they will continue to emit at the same frequency over a longer period of time. However a system consisting of a laser locked to an atomic reference could be guaranteed to always produce light at the same frequency.

For data transmission which relies on modulating one laser source and demodulating using another, we have had to invent DSP techniques which can

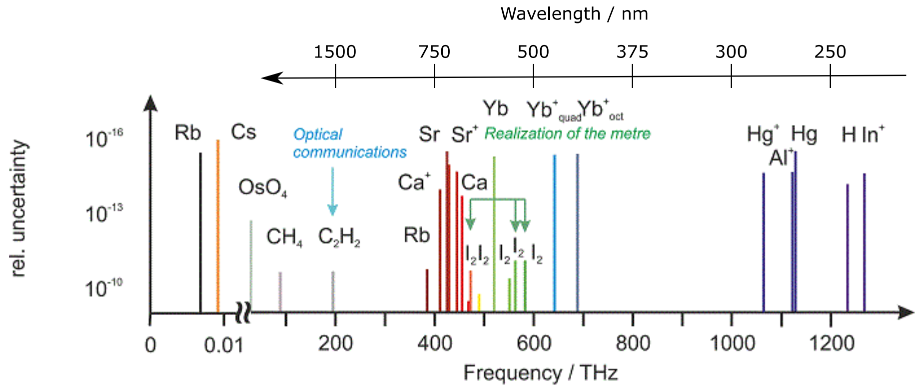

Figure 4.1: *Overview of the frequency standards recognized by the BIPM. Figure adapted from [98].*

compensate for the frequency drift between the two lasers. In this chapter we will present a frequency reference useful for locking a frequency comb operating in the telecommunication C band. Referencing combs have the advantage that we can reference any one of the comb lines in order to fix the entire comb. This is particularly useful because only certain atomic or molecular transitions are recognized as official standards and they are spaced far apart as shown on Figure 4.1.

The Acetylene standard

One specific frequency reference uses the acetylene molecule $^{13}C_2H_2$ which includes a carbon-13 isotope instead of the more commonly found carbon-12. The molecular structure of acetylene allows for five different vibrational modes ν_{1-5} with excitation frequencies (wavelengths) between 18.4 THz (16.31 µm) and 101.1 THz (2.965 µm). [99] They can however also interact nonlinearly and produce combinations of the vibrations with much higher excitation frequencies, with one combination being of particular interest; $\nu_1+\nu_3$ as it is in the middle of the C band. It has a specified transition frequency of 194.369 569 384 THz (1542.383 712 38 nm)[100] when probing a $^{13}C_2H_2$ gas at a 3 kPa pressure. Existing frequency references based on acetylene do exist, but they have all used lock-in amplifiers to increase the signal to noise ratio. This limits the feedback bandwidth to just a few kHz and therefore limits the short term stability. Here we present a setup based on a technique known as noise immune cavity enhanced optical heterodyne molecular spectroscopy (NICEOHMS) which does not have this feedback limitation.

4.1 The NICEOHMS technique

NICEOHMS is, as the name suggests, a spectroscopic technique which uses the advantages of cavity power build up without the downsides of cavity length

99. Riehle, *Frequency Standards*(2003)
100. BIPM, *Recommende Values of Standard Frequencies for Applications Including the Practical Realization of the Metre and Secondary Representation of the Second - Acetylene (1.54 Um)*(2007/ Oktober)

fluctuations creating amplitude noise. To explain the concept it is beneficial to take a step back and consider the PDH technique [101].

Pound-Drever-Hall

One of the main utilizations of the PDH technique is to stabilize a laser to a Fabry Pérot etalon or cavity. Such a cavity is typically made of two highly reflective mirrors, and has a reflection transfer function which can be shown to be[99]:

$$r_{FP}(\omega') = \frac{E_{\text{reflect}}}{E_{\text{in}}} = r\frac{1 - e^{-i\omega' 2L/c}}{1 - r^2 e^{-i\omega' 2L/c}}. \tag{4.1.1}$$

Here r is the reflection of the mirrors, L is the length of the cavity and ω' is the frequency of the incident light. The factor $e^{-i\omega' 2L/c}$ is the phase picked up by the electric field when travelling between the two mirrors. The reflection coefficient is complex with the real part representing the absorption of the cavity and the imaginary part representing the dispersion. These are both plotted on Figure 4.2 for two different reflectivities. The top row shows a zoomed in view around a cavity resonance, and the bottom row shows we have resonances at every $^c/_{2L}$ = integer which is also known as the cavity FSR.

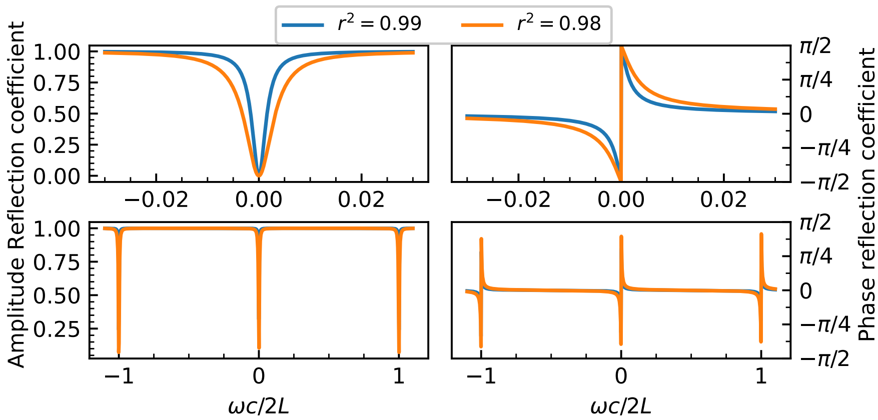

Figure 4.2: *Plot of the amplitude and phase cavity response. Left column shows the power reflection coefficient ($r_{FP}r^*_{FP}$), right column shows the phase reflection coefficient, i.e. the phase imprinted on a reflected beam from the cavity. Top row shows a zoomed in view of the bottom row.*

The phase response lends itself naturally as an error signal for stabilization as it is linear and monotone around the cavity resonance. One way of measuring the phase response would be to set up a small interferometer before the cavity and use the light reflecting off the cavity as one of the arms. It would however be very difficult to distinguish path length changes from frequency changes, as they would both affect the measured phase.

The PDH is a neat trick to avoid this where the idea is to phase modulate a laser beam using an EOM. We begin with the complex description of a

101. Drever et al., "Laser Phase and Frequency Stabilization Using an Optical Resonator"(1983)
99. Riehle, *Frequency Standards*(2003)

monochromatic polarized electromagnetic field oscillating at frequency ω with phase ϕ:

$$E(\omega) = E_0 \cos(\omega t + \phi) = \mathrm{Re}\{E_0/2e^{i\omega t+\phi}\} \tag{4.1.2}$$

We will now focus on the exponential, and then simply take the real part at the end. We can then apply a sinusoidal modulation of the phase with frequency Γ and amplitude β:

$$E_{\mathrm{mod}} = \mathrm{Re}\left\{E_0/2e^{i(\omega t+\beta\sin(\Omega t))}\right\} \tag{4.1.3}$$

We now use the Jacobi-Anger expansion to rewrite this in terms of Bessel functions of the first kind (J_k):

$$E_{\mathrm{mod}} = \mathrm{Re}\left\{E_0/2\left(J_0(\beta)e^{i\omega t} + \sum_{n=1}^{\infty} J_n(\beta)\left(e^{i(\omega+n\Omega)t} + (-1)^n e^{i(\omega-n\Omega)t}\right)\right)\right\} \tag{4.1.4}$$

For small modulations ($\beta > 1.5$) it is enough to limit ourselves to only the first term in the sum:

$$E_{\mathrm{mod}} = \mathrm{Re}\left\{E_0/2\left(J_0(\beta)e^{i\omega t} + J_1(\beta)\left(e^{i(\omega+\Omega)t} - e^{i(\omega-\Omega)t}\right)\right)\right\}. \tag{4.1.5}$$

We see that the positive sideband ($\omega + \Omega$) and the negative sideband ($\omega - \Omega$) have opposite signs and are thus 180° out of phase. This means the beatnote between the carrier and the positive sideband will be completely out of phase with the beatnote between the carrier and the negative sideband, and they will therefore completely destructively interfere. This can also be described as balancing the triplet because as long as the amplitude and phase relation between the three frequency components remains constant, there will be no observable beatnote.

When reflecting the triplet off a cavity the reflected field can be found using Equation 4.1.1:

$$\begin{aligned} E_{\mathrm{reflect}} = \mathrm{Re}\Big\{ E_0/2\big[& r_{FP}(\omega)J_0(\beta)e^{i\omega t} \\ & + r_{FP}(\omega+\Omega)J_1(\beta)e^{i(\omega+\Omega)t} \\ & - r_{FP}(\omega-\Omega)J_1(\beta)e^{i(\omega-\Omega)t}\big]\Big\}. \end{aligned} \tag{4.1.6}$$

This field is then measured by a photodiode which actually samples the intensity, $I \propto E \cdot E^*$. When the modulation frequency is smaller than the free spectral range, but larger than the linewidth of the cavity, the three frequency components in the triplet will sample different parts of the dispersion profile, i.e. experience different phase and amplitude reflection coefficients.

In the case where the carrier is close to, but not exactly on resonance, the two sidebands will be far off resonance and experience almost no phase response from the cavity. In contrast the carrier will experience either a positive or negative phase reflection coefficient. This will imbalance the triplet, and a beatnote will appear at the modulation frequency. By demodulating this beatnote we can create a DC signal which is proportional to the phase response of the cavity. This is shown on Figure 4.3 for two different reflectivities. The two symmetric features around the central point is the effect of one of the sidebands being on resonance with the cavity. This also causes a phase and amplitude imbalance which creates a phase response signal similar to the carrier, but with the opposite slope. A further advantage of the PDH method is that the error signal is generated at the modulation frequency and therefore immune to many DC noise effects and thermally induced electronic noise which is typically proportional to $\frac{1}{f}$.

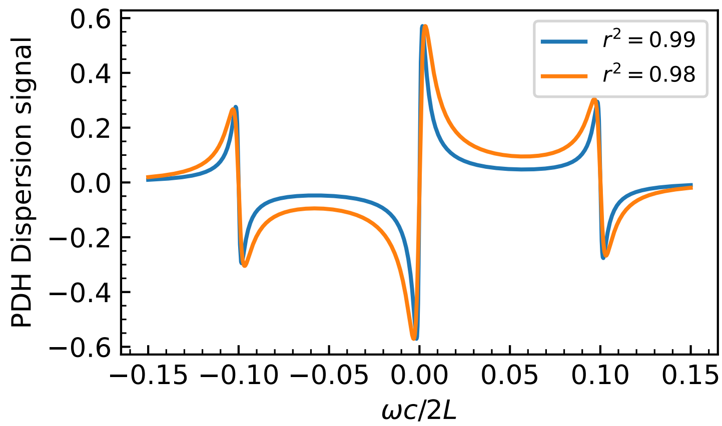

Figure 4.3: *The PDH response when demodulating in-phase at the modulation frequency ($\Omega = 0.1\omega c/2L$)*

Frequency Modulation Spectroscopy

While PDH does allows us to stabilize a laser to a cavity it will never be an ideal frequency reference as the absolute frequency position depends on the constructed length of the cavity. As mentioned in the introduction we instead want to use atomic signals to stabilize our lasers. The amplitude and phase response of an atom, also sometimes referred to as the imaginary and real part of the complex refractive index [102], looks in shape identical to the cavity response as seen on Figure 4.4. The major difference is that the centre resonance frequency is not determined by any man made constructs, but instead depends on the specific atomic or molecular structure. There are still a number of parameters which shift this frequency, such as collisions between atoms, their velocity, or external magnetic fields. But these are all properties which we can measure and control. One can argue that we could also simply control the length of a Fabry Pérot etalon. But as the unit of length is derived from the speed of light and the definition of the second[12], it becomes a circular argument where we need a well defined frequency reference to determine a well defined length reference to construct a well defined frequency reference.

102. Steck, *Quantum and Atom Optics Textbook*(2007)

[12] Which is just the inverse of frequency

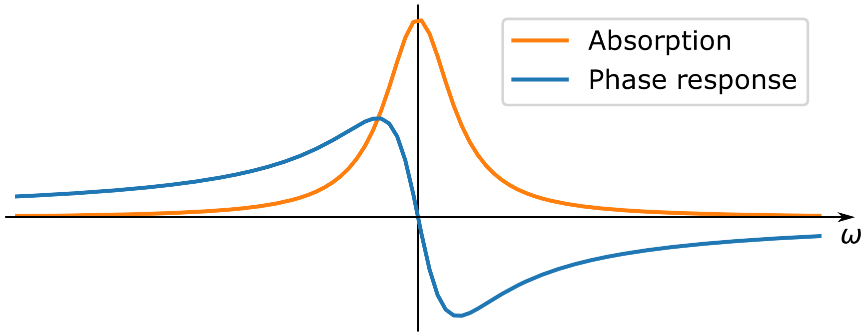

Figure 4.4: *Illustration of the optical atomic response, showing the absorption and the phase response around an atomic resonance.*

The best way of measuring, or probing, the transition frequency of atoms or molecules, is in their gaseous form as they here act as a large number of independent single entities. They will only interact weakly through collisions but these can be controlled and measured by adjusting parameters like the temperature and the pressure of the gas.

Because the phase response of atoms looks so similar to the cavity we can use the same idea to probe it by sending a phase modulated beam of light through a glass cell containing the atomic gas. If the modulation frequency is much wider than the linewidth of the atomic resonance only the carrier will be affected just like in the PDH technique. Recording the transmission and demodulating will then produce a signal similar to what we observed in the PDH reflection. This is called frequency modulation (FM) spectroscopy and has been a stable technique in atomic, molecular and optical physics since the 1980s[103].

NICEOHMS

While FM spectroscopy is a useful technique it it limited by the number of atoms we can interact with as we simultaneously wish to keep the pressure low in order to minimize inter-atom interactions. We can therefore increase the interaction length, i.e. the length of the beam path which overlaps with the atomic gas, by increasing the length of the gas cell or by passing it through the cell multiple times by placing mirrors on each side of the cell. If one then aligns the mirrors carefully so it becomes a cavity, then not only will the interaction length be increased proportional to the finesse of the cavity, but the power enhancement effect of the cavity will increase the interaction with the gas. The issue is now that FM spectroscopy relies on the frequency triplet only being affected by the phase response of the atoms, and if the triples also has to pass through a cavity, then the phase response of the cavity will be imprinted on the triplet simultaneously. This can be avoided if the phase modulation frequency matches the cavity FSR, as all three components of the triplet will now be on resonance with the cavity, but only the carrier frequency will be at resonance with the gas. This was first called cavity assisted FM spectroscopy and relied on the cavity being very stable, as any detuning between the probe laser and the

103. Bjorklund, "Frequency-Modulation Spectroscopy"(1980)

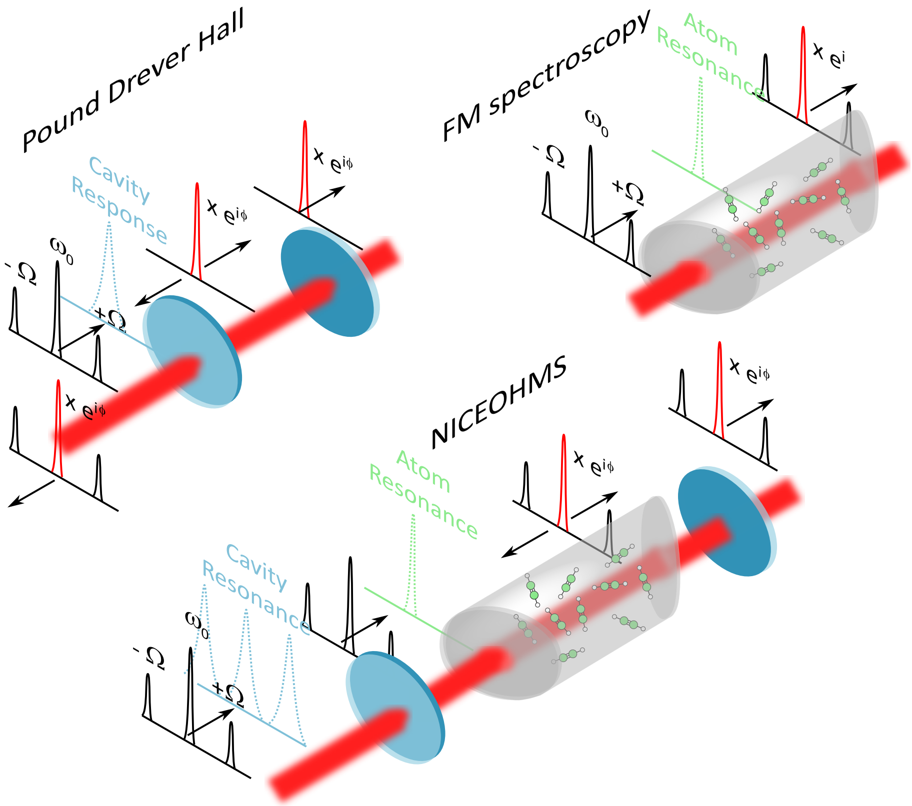

Figure 4.5: *Illustration of the PDH, FM and NICEOHMS spectroscopic technique. Each setup shows how the initially modulated frequency spectrum (in black) gets affected by the cavity resonance (dashed blue) or atomic resonance (dashed green). The frequency components affected are then marked with red. Each technique relies on detecting three frequency components with one of them being affected by the cavity/atom system.*

cavity would mix into the atomic phase response signal. If we combine the cavity assisted FM spectroscopy with the PDH method to keep the cavity locked to the laser, then we end up with a cavity enhanced spectroscopy technique which is insensitive to cavity detuning noise, also known as NICEOHMS[104]. A schematic illustration of the NICEOHMS technique, together with the PDH and FM technique is shown on Figure 4.5. This figure shows how the frequency triplet is affected by the cavity, the atomic response, or both, with the red colour indicating that a frequency component in the triplet has experienced some phase change. Another advantage of the NICEOHMS technique is that it can simultaneously be insensitive to the velocity of the atoms. Due to the finite temperature of the gas, the atoms will have a nonzero velocity. This will cause a Doppler shift of the atomic resonance relative to the laser, and will lead to an inhomogeneous broadening of the atomic transition, making the signal much wider than the natural linewidth. The optical standing wave in the cavity can

104. Ma et al., "Ultrasensitive Frequency-Modulation Spectroscopy Enhanced by a High-Finesse Optical Cavity: Theory and Application to Overtone Transitions of C_2H_2 and C_2HD" (1999)

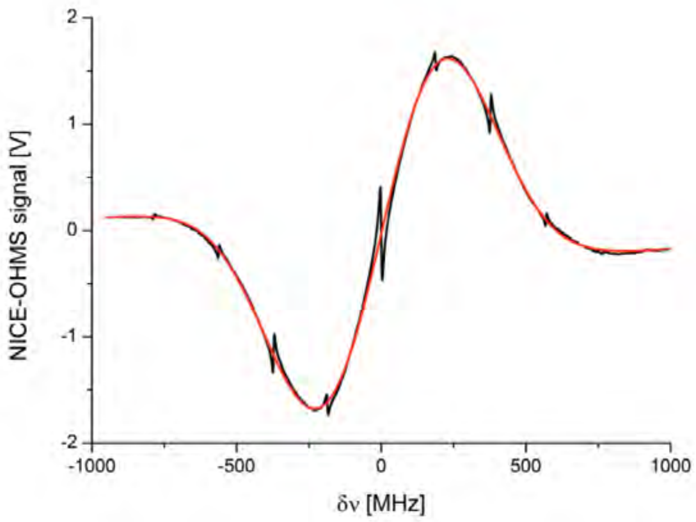

Figure 4.6: *Data from a full scan of a NICEOHMS signal of the acetylene (C_2H_2). The red is a fit to the Doppler broadened NICEOHMS signal. The discrepancies between the red and black are the subDoppler features which appear due to saturated absorption. The graph is from [105]*

be decomposed into two counter propagating travelling waves, and the atoms which have a nonzero velocity along the cavity axis will only interact with either the left or right propagating beam. However the atoms which only have a radial velocity will interact with both beams simultaneously. If the beams are strong enough the atomic transition will be saturated and the non Doppler broadened transition will appear as a decrease in absorption in the middle of the Doppler broadened absorption feature. Similarly the phase response will be smaller, and inverted, at the point where the non Doppler broadened transition is found. It is illustrated in Figure 4.6 where the black is data and the red is a theoretical fit to the Doppler broadened NICEOHMS signal. The discrepancies between the black and the red are the non Doppler broadened transitions. The largest and central transition is the carrier, while all the others are sidebands, similar to the structures seen in Figure 4.3. This data is from [105], and taken on a cell of acetylene (C_2H_2) gas at room temperature.

RAM

Because NICEOHMS relies on having a balanced frequency triplet from the phase modulation, it becomes sensitive to anything which upsets the triplet balance. This is often labelled as residual amplitude modulation (RAM) which has historically been defined as:

> By definition, RAM is the signal obtained with the sample and all other parallel optical surfaces removed from the postmodulator beam path. *Whittaker et.al. 1985*[106]

105. Silander, *Cavity Enhanced Optical Sensing*(2015)
106. Whittaker et al., "Residual Amplitude Modulation in Laser Electro-Optic Phase Modulation"(1985)

RAM can arise from many different sources such as the birefringence in the EOM crystals. If the polarization of the light is misaligned with the crystal axis then the output light will be elliptically polarized, but to a varying degree between the three frequency components in the triplet. Any polarization sensitive element after the EOM will then convert this difference in ellipticity to an amplitude difference and thus a triplet imbalance. This is especially a problem in fibre coupled EOMs as we cannot adjust the alignment between the fibre and the crystal[107]. Additionally any parallel surfaces in the setup will lead to parasitic etalons, which due to the typical low finesse will change the amplitude of the two sidebands differently, thus again leading to an imbalanced triplet and detectable beat note. These RAM effects are in principle not detrimental to frequency stabilization, except for the fact that they are typically affected by temperature and stress, making them fluctuate and thereby limiting the frequency stability. We can measure RAM by detecting the frequency triplet before the cavity. In that way we get a measure for the phase response of every component up until the cavity and gas cell which is our real interest. As demonstrated by multiple groups [107],[108], the RAM effect can generally be counteracted by applying a DC offset to the EOM. This has been shown on multiple occasions to reduce the effects of RAM and even work better than passive approaches to align the polarization with the EOM or remove the parasitic etalons.

107. Foltynowicz et al., "Reduction of Background Signals in Fiber-Based NICE-OHMS"(2011)
107. Foltynowicz et al., "Reduction of Background Signals in Fiber-Based NICE-OHMS"(2011)
108. Wong et al., "Servo Control of Amplitude Modulation in Frequency-Modulation Spectroscopy: Demonstration of Shot-Noise-Limited Detection"(1985)

4.2 Our experimental NICEOHMS setup

Our experimental NICEOHMS setup is illustrated schematically on Figure 4.7. It consists of an erbium doped fibre laser (NKT Koheras Basik E15) which is frequency stabilized to an acetylene gas cell using an acousto optical modulator (AOM). The fibre laser has an output of $\sim 40\,\mathrm{mW}$ and an internal piezo tuning which allows for frequency tuning with a bandwidth of 20 kHz to 30 kHz. The AOM is used for fast frequency feedback, as it allows us to achieve feedback bandwidths of a few MHz.

After the AOM the laser is passed through a fibre coupled EOM which provides three separate functions:

- Create sidebands at $\nu_{\mathrm{PDH}} = 10\,\mathrm{MHz}$ for PDH locking the length of the cavity to the laser (Blue electronic path in Figure 4.7). The cavity length is modulated by a piezo mounted to the mirror. This ensures that the cavity is always on resonance with the carrier laser
- Create sidebands at $\nu_{\mathrm{NICEOHMS}} = 1\mathrm{FSR}$ for NICEOHMS locking the laser to the acetylene molecules (Green electronic path in Figure 4.7).
- Apply a DC offset to the EOM which counteracts RAM (Yellow electronic path in Figure 4.7). This will be explained in detail later.

After the EOM the laser is brought via fibre to the free space part of the setup. Here a Faraday isolator is used to suppress any backscatter back into the fibre with 40 dB. It also acts as a polariser, ensuring a stable and linear polarization after the fibre. The first beam sampler encountered splits off some of the light reflected back from the first cavity mirror to generate the PDH signal (Blue path in Figure 4.7. This is done by demodulating the detected PD signal in a mixer. The error signal is then sent to a PID controller which applies a feedback to the input cavity mirror This is opposite of how we introduced the PDH technique, but the principle is the same whether we lock a laser to a cavity or vice versa. The second beam sampler splits off a bit of the forward propagating light before it hits the cavity. This signal is also demodulated using a mixer and produces the RAM error signal described earlier. This is then fed to a separate PID controller which applies a DC feedback to the EOM in order to counteract any RAM effects. As this technique can only measure RAM effects incurred up until the beam sampler it is important that it is mounted as close to the cavity as possible. The cavity itself is constructed of two curved mirrors with a radius of curvature of 9 m and a separation distance of 23 cm. This gives a waist size of 0.7 mm and an FSR of 650 MHz with a finesse around 300 A lens is used to mode match the light with the cavity in order to optimize the coupling efficiency, and a $\lambda/2$ waveplate is used align the polarization with the sides of the glass cell. They are cut at Brewster's angle in order to minimize reflections from entering and exiting the glass cell. As described previously the cavity transmission light consists of the carrier and the two sidebands at ν_{NICEOHMS} which are all resonant with the cavity. However since the phase of the carrier has been affected by the dispersion of the molecules, we can measure the phase response by demodulating the detected signal at ν_{NICEOHMS} using another mixer. This signal is then sent to a third PID controller which in turn stabilizes the frequency of the laser by feeding

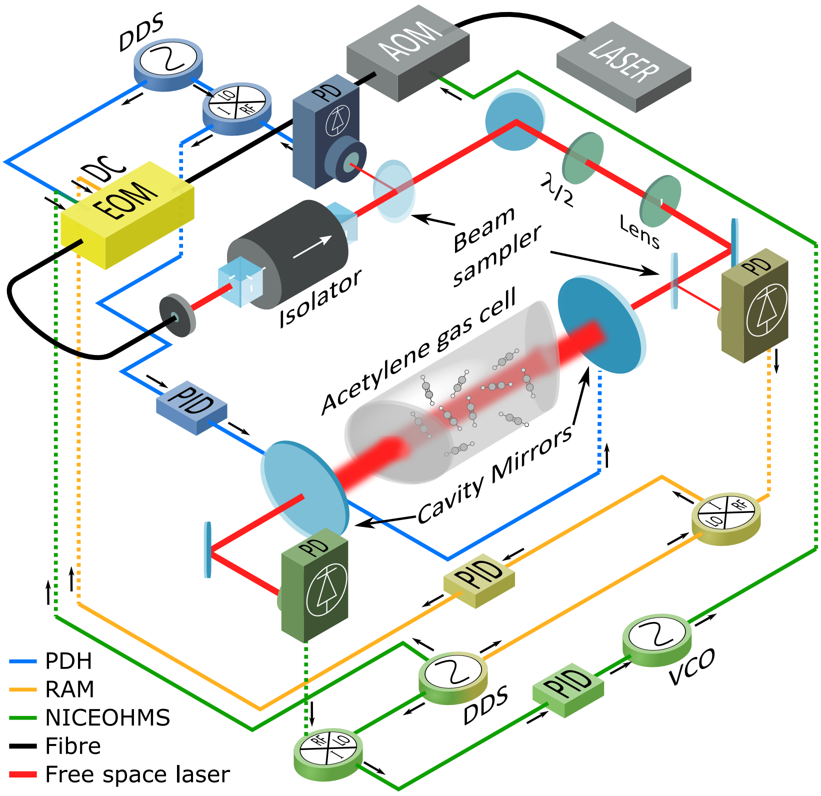

Figure 4.7: *A schematic illustration of the experimental NICEOHMS setup. The small arrows indicate the direction of the electrical signals.*

back to the voltage controlled oscillator (VCO) driving the AOM. In this way the laser itself is not stabilized and it is only the light after the AOM which is locked to the acetylene transition.

Our experimental setup is envisioned to work together with micro combs and other integrated components, and is therefore aimed at being compact and transportable. This is achieved by using fibre components for the alignment sensitive components such as the laser source, the EOM and the AOM. All the free space components fit inside an aluminium box measuring $144 \times 388 \times 528$ mm. The free space optical components are mounted on an aluminium breadboard, placed on vibration isolating rubber inside the box. The cavity mirror holders are furthermore glued onto a single piece of Zerodur low expansion glass, to prevent temperature fluctuations from influencing the cavity. All the electronic components except the photodiodes are placed outside the aluminium box, with the electrical signals being transferred through air tight feed through in the side of the box. The optical fibre is likewise installed with an air tight feed through which allows us to pump a vacuum in the box and thereby minimizing thermal and acoustical noise sources. A cross section of the box is illustrated in Figure 4.8.

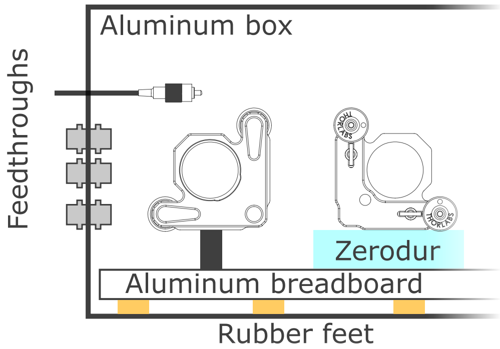

Figure 4.8: *A cross section view of the NICEOHMS setup. The aluminum breadboard is standing on rubber feet inside the aluminium box, and the cavity mirror mounts are further glued on top of a piece of Zerodur glass.*

Quality of the spectroscopic signals

The advantage of NICEOHMS over saturated absorption spectroscopy is evident if we look at the two signals plotted on Figure 4.9. The left plot is the transmission signal, i.e. the saturated absorption signal, and the right plot is the NICEOHMS signal, both taken under identical conditions. They can be modelled with a Lorentzian lineshape and a dispersion lineshape respectively:

$$L_{\mathrm{SA}} = A + B \cdot \nu + C \frac{E^2}{(\nu - D)^2 + E^2} \tag{4.2.1}$$

$$L_{\mathrm{NO}} = A + B \cdot \nu + C \frac{D^2 - \nu^2}{(D^2 - \nu^2)^2 + E^2 \nu^2} \tag{4.2.2}$$

And the red lines in Figure 4.9 are fits to these two models. The residuals of the fits are plotted on the lower part of Figure 4.9. Here we see that especially around zero detuning the models are not ideal. It is however not a concern for us as we will only be using the model and the residuals to estimate the noise of the signal. The NICEOHMS signal can be locked at zero detuning due to the discriminating slope, while the saturated absorption signal can be locked on either side of the peak, where the slope is largest. The actual locking performance is best evaluated by fitting a straight line around the locking point. This is done for both signals and plotted in green on Figure 4.9. The slope of this line represents our ability to measure frequency deviations as electronic signals.

We can also estimate the electronic noise by looking at the signals far detuned from the resonance, where the slope of the signal is zero. At such a point the signal will be insensitive to frequency noise of the laser, thus giving us an estimate of the electronic noise in the setup. For the saturated absorption signal we use the part indicated in orange on the residuals plot, while for the NICEOHMS we use part of the signal not visible on the plot. The quality of the signal can then be estimated by converting the electronic noise to frequency noise by dividing with the slope. This will give us the locking linewidth and indicate the smallest instantaneous linewidth we can achieve with a laser

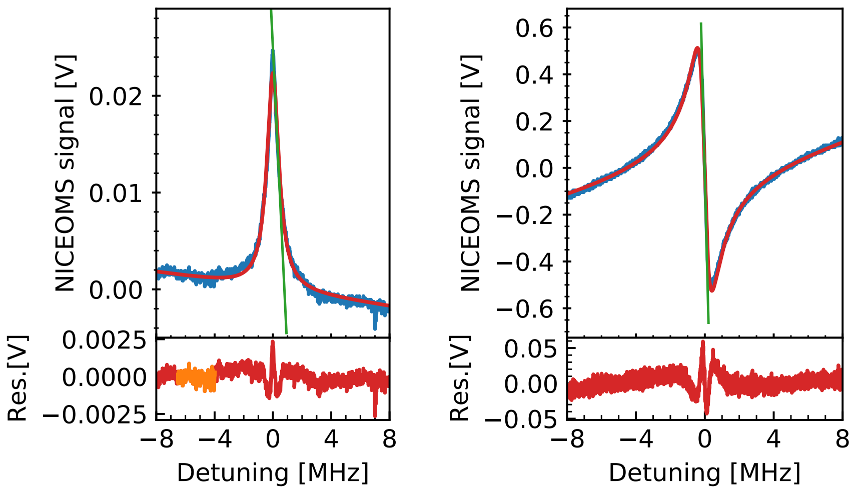

Figure 4.9: *Saturated absorption signal from the Acetylene glass cell (right). NICEOHMS signal from the Acetylene glass cell (left).*

locked to the signal:

$$\text{Sat.Absorp.} \quad E_{\text{noise}} = 0.31\,\text{mV} \quad \frac{d\nu}{dV} = 31.5\,\text{MHz/V} \quad \Delta\nu = 9.8\,\text{kHz} \tag{4.2.3}$$

$$\text{NICEOHMS} \quad E_{\text{noise}} = 6.4\,\text{mV} \quad \frac{d\nu}{dV} = 338\,\text{kHz/V} \quad \Delta\nu = 2.2\,\text{kHz} \tag{4.2.4}$$

So while both signals are sub Doppler, the NICEOHMS signal offers almost ten times lower locking linewidth.

RAM cancellation setup

While we plan to use the DC feedback to the EOM to minimize the RAM, we can also controllably induce it this way. Figure 4.10 shows the response from the RAM detection when we apply a triangular ramp the EOM DC voltage. By optimizing the amplitude of the sinusoidal we can maximise the RAM detection sensitivity. The effect of the RAM stabilization feedback can be measured by monitoring the NICEOHMS signal offset. As RAM will cause the dispersive signal (Figure 4.9) to shift up and down it will induce an offset of the NICEOHMS signal which we can monitor. This is shown on Figure 4.11 for both the case of with and without active RAM stabilization. The two traces show the NICEOHMS signal offset recorded over a period of 15 min and show a clear improvement in stability when the RAM is stabilized.

As stated earlier RAM can have many causes such as crystal misalignments or parasitic etalons and many of them will be connected to thermal variations in the setup. We test this by locally heating the EOM while the RAM stabilization is active. This will change the stress of both the internal crystal and the connecting fibres and will change the polarization mismatch in the EOM. The EOM is placed in a copper block in order to increase the thermal mass, and can be heated using a small heating pad underneath the copper block. The

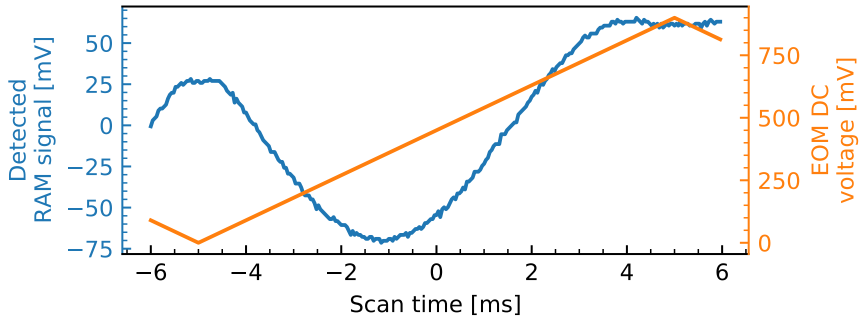

Figure 4.10: *Detected RAM signal when applying a ramping DC voltage to the EOM.*

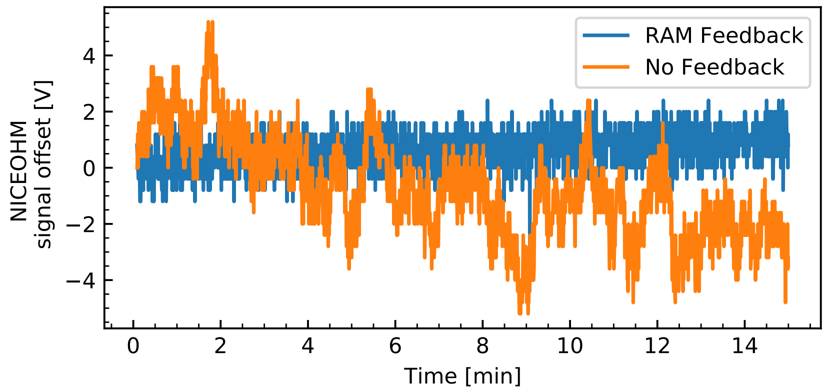

Figure 4.11: *NICEOHMS signal offset over time with and without the RAM feedback.*

temperature is shown on Figure 4.12 together with the NICEOHMS signal midpoint (upper) and the input and output from the RAM stabilization system (lower). It is evident that the feedback is able to compensate completely for the temperature change, and thus it is not necessary for us to stabilize the temperature of the EOM.

If we then instead look at heating the breadboard which the setup is mounted to we see the effect shown in Figure 4.13. Here the RAM feedback signal is not correlated with the temperature, and the NICEOHMS offset undergoes a strong oscillatory behaviour as the breadboard is heated up. The offset is almost as large as the amplitude of the NICEOHMS signal itself, meaning it could potentially drive the signal completely out of locking range. This is an unexpected behaviour as the RAM feedback system should be able to remove any RAM effects up until the sampling point. We can therefore assume that this is due to thermal effects happening between the first cavity mirror and the NICEOHMS signal photodiode. This might be an etalon between the last cavity mirror and the photodiode, and could be fixed by placing

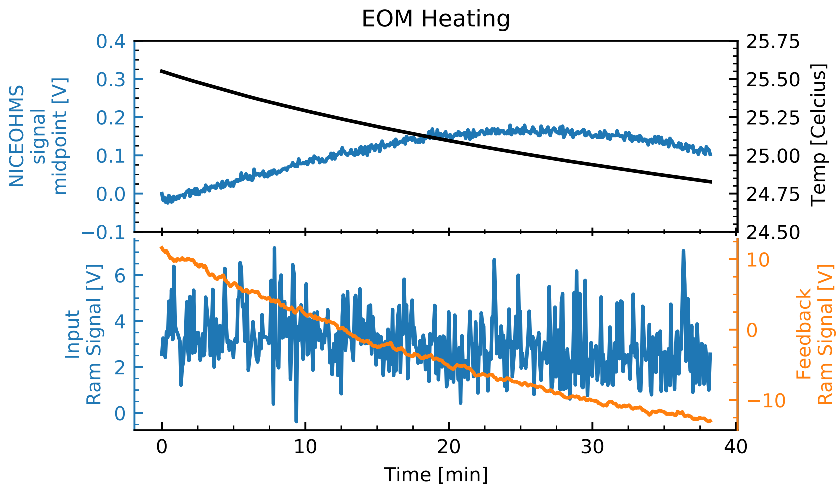

Figure 4.12: *NICEOHMS and RAM signal dependence on heating the EOM. When RAM DC feedback is applied, it can compensate for any heating effects applied to the EOM.*

the detector at an etalon immune distance[109]. If the detector is placed at a distance similar to the cavity length then any etalons created will not influence the phase or amplitude balance of the triplet as they will all be resonant with this new etalon. We do not have the space in the box to place the detector 23 cm away from the cavity so we instead angle the detector to misalign any parasitic etalons. With this we were able to minimize but unfortunately not remove the effect completely.

109. Ehlers et al., "Use of Etalon-Immune Distances to Reduce the Influence of Background Signals in Frequency-Modulation Spectroscopy and Noise-Immune Cavity-Enhanced Optical Heterodyne Molecular Spectroscopy" (2014)

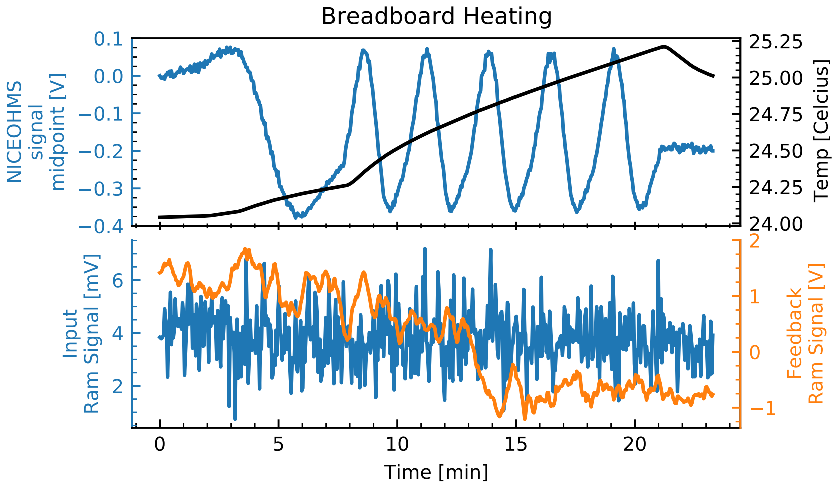

Figure 4.13: *NICEOHMS and RAM signal dependence on heating the breadboard of the setup. Even with RAM DC feedback it cannot compensate for heating effects applied to the breadboard.*

Estimating frequency stability

The instantaneous locking linewidth we calculated above determines how well we can determine the frequency of the atomic transition from a single measurement. However for metrology purposes the final goal is not to have the smallest linewidth, but rather to determine the transition frequency as accurately and precisely as possible. As explained in Section 2.5 the Allan deviation is the

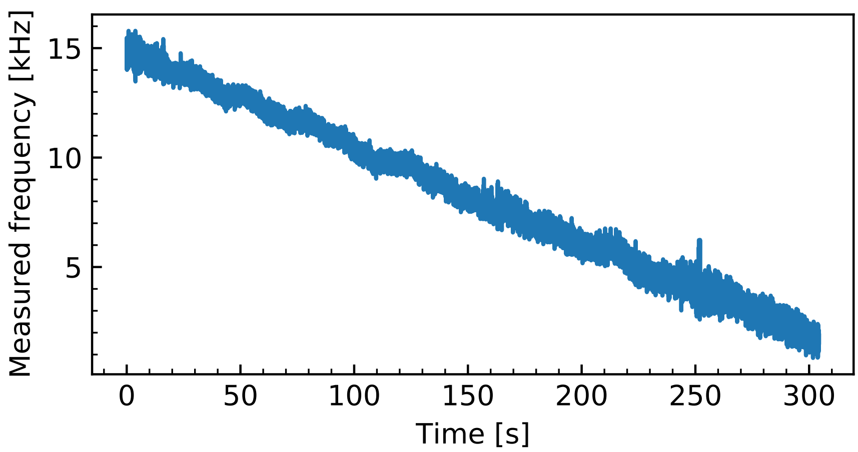

Figure 4.14: *Measured frequency beat note data between our two acetylene based frequency references. There is an observable linear frequency drift visible in the beat-note.*

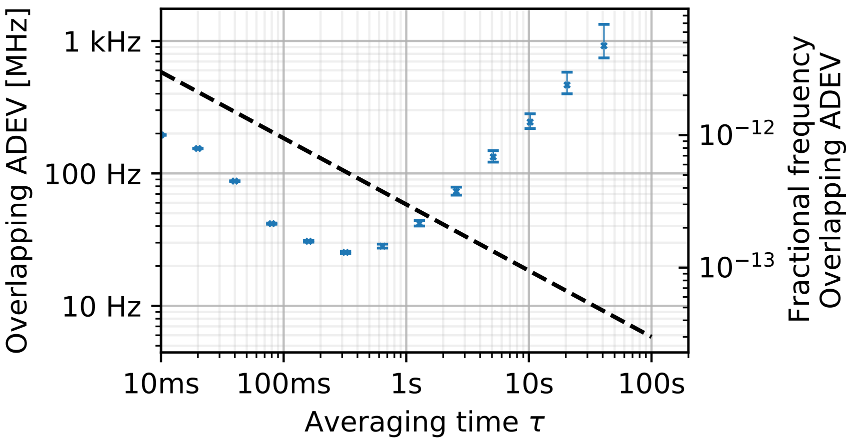

Figure 4.15: *Allan deviation as a function of measurement time τ for our Acetylene based molecular reference. The black dashed line indicates the performance of the Stabiλaser.*

variance estimator we use to characterize the stability of the system, and help determine how well we can measure the molecular transition frequency. This time we obtain the frequency data by locking our laser to the molecular transition and measuring its frequency against a reference laser. The best reference laser we have at 1542 nm is the NKT Koheras Basic E15, which is identical to the laser we are stabilizing to the molecular transition, and we can therefore not use it as a reference. Instead we building two identical setups using independent components and beat them against each other. The downsampled beatnote is around 15 kHz and detected on a 1 GHz photodiode before being measured on a CNT-90 frequency counter. The measured frequency data is shown on Figure 4.14 where a large linear drift is easily observable. From this data the overlapping Allan deviation is calculated and divided by $\sqrt{2}$ as we assume both setups contribute equally to the noise. The resulting Allan deviation is shown on Figure 4.15 plotted as a function of integration time τ. The figure indicates that we are initially dominated by white frequency noise up until the 500 ms point, where the Allan deviation turns around and starts rising with a slope of $\propto \tau^1$ as expected due to the linear frequency drift. We are able to achieve a stability of 25 Hz at 0.2 s, or fractional frequency stability of 1.3×10^{-13}@0.2 s.

Our setup is very similar to a commercially available product, namely the Stabiλaser from DFM[110] which is based on saturated absorption (See [111] for more details). This product uses the same acetylene gas, and an identical laser, and is therefore a good point of reference. The black dashed line in Figure 4.15 indicates the reported stability of the Stabiλaser. We see that our setup has superior performance at low frequency times but looses out at longer time scales because the Stabiλaser has no frequency drift up to 100 s. The

110. DFM, *Stabilaser Accessed on 2022/01*()
111. Talvard et al., "Enhancement of the Performance of a Fiber-Based Frequency Comb by Referencing to an Acetylene-Stabilized Fiber Laser"(2017)

Stabiλaser uses a lock-in amplifier to increase the signal to noise ratio, and is therefore limited in feedback bandwidth to the lock in frequency of $\approx 1\,\mathrm{kHz}$. In contrast our setup is limited by the AOM which has a bandwidth two orders of magnitude larger. This will allow us to achieve better stabilities at time scales smaller than 1 ms. As the our setup and the Stabiλaser use many identical components we believe that our observed frequency drift is not a fundamental limitation of the setup but rather an unknown drift in our system. Other groups have demonstrated longer stability times than us when using the NICEOHMS technique on acetylene[112], however with a focus on trace gas detection the results are not directly comparable. Smaller and more compact setups have also been demonstrated, and especially chip scale setups are of particular interest in combination with the Kerr frequency combs. However their performance is still quite limited at 7×10^{-9} at 1 s in fractional stability[113].

112. Zhao et al., "High-Resolution Trace Gas Detection by Sub-Doppler Noise-Immune Cavity-Enhanced Optical Heterodyne Molecular Spectrometry: Application to Detection of Acetylene in Human Breath" (2019)
113. Zektzer et al., "A Chip-Scale Optical Frequency Reference for the Telecommunication Band Based on Acetylene" (2020)

Chapter 5

Summary and outlook

In this work we have studied S_3N_4 based dissipative dark pulse Kerr combs in resonators with normal dispersion. We have seen how their generation relies on locally shifting the dispersion in order to phase match the FWM process. Here the shifting was done through mode interactions between two propagating frequency modes in the MRR which created an avoided mode crossing when the detuning between them was decreased. Due to the difference in optical path length for the two modes we were able to change the detuning using the integrated micro heater. While the exact thermal dynamics of the MRR are difficult to predict, we managed to measure the dispersion across a range of heating powers and in that way map out how the thermal dependence of the mode interactions. To aid in this we created a free space cavity calibration reference to replace to commonly used fibre loop cavities or fibre frequency combs. This provided a low cost calibration option which required little to no daily adjustment and was completely dispersion free by design. We showed that the long cavity with the small FSR was important for precisely mapping out the mode crossing shifts, however for just measuring the group velocity dispersion we could have used a ten times smaller cavity. Further work should be done using a smaller cavity and possibly the inclusion of higher order transversal modes to create a smaller, more compact setup.

Using the obtained dispersion results we were able to map out the dispersion as a function of heater power and integrate it into the PyLLE python package as a variable. This allowed us to simulate the generation of frequency combs with using the heater power to ramp the detuning of the pump and the dispersion. With this we were able to qualitatively simulate the dark pulse Kerr combs, however our simulations contradict other published results that claim the comb exists with the pump on the blue detuned side of the resonance. Our model should be compared more extensively to the established coupled mode theory in order to find the discrepancies. It is important to note that our method of modelling the connection between the dispersion, detuning, and the heater power neglects the internal thermal effects that arise due to absorption inside the MRR. We have observed that changing the optical power changes the heating voltage at which we see comb power being generated, due to the increased optical power changing the detuning of the resonance. In connection with our measured thermal shift value we should be able to measure how the optical power shifts the resonance and in that way include it in our simulation model. It could give us insight into the instabilities we observed in the generation and stabilization chapter and might reveal if they are connected to thermal effects.

We also presented a scheme for automatically generating and stabilizing the dark pulse Kerr combs using the integrated micro heaters. We investigated using the generated comb power as the stabilization signal and while we were able to successfully generate and stabilize mode locked optical frequency combs, we also observed several issues in this process. We showed that several different spectral shapes all generate the same comb power, and that these states have very different amplitude stabilities. This could potentially be an experimental issue as we only used the lower half of the comb spectrum to determine the comb power, and it should be explored if the effects persist when measuring the full comb spectrum. We also saw the existence of specific states in which the comb seemed to prefer to operate and we could force comb jumps between states by changing the stabilization setpoint. This further points towards the generated comb power not being a good stabilization parameter despite it working for bright solitons. Future work would include setting up a direct measurement of the effective detuning while the comb is running, as this will give us insight into the dynamics at play when the amplitudes vary or the comb states change. Initial work was done using the PDH method to measure the detuning but so far the work has been inconclusive. It should be investigated if the other avoided mode crossing points show better stability performances, even though they are less relevant for telecommunication experiments. Lastly our results point towards that while the less restricted state tunability of dark pulse combs, compared to their bright soliton counterparts, allow for easy generation, it also increases the stabilization requirements. While we did show that the amplitude instability happens both when using the heater feedback and when using pump frequency feedback, the micro heater approach could still be flawed as we know it couples the detuning to the dispersion. It should be investigated if the micro heater approach can be used to stabilize either bright solitons or coupled rings (photonic molecule), as the dispersion in both these systems is disconnected from the heater power.

Despite these stabilization issues we still managed to utilize the generated frequency comb as a light source for optical data communication as we ran the comb near-continuously for more than four days while gathering transmission data. The high output power and relatively flat structure of the comb spectrum lends itself naturally to dense WDM and SDM, and the instabilities can be compensated for by the existing DSP schemes already utilized. The ability to use a comb as a light source for 8251 individual data channels (16251 if you count the polarization separately) truly shows the potential for replacing the large amount of laser arrays used today when dense WDM and SDM is employed. This cuts down significantly on the number of components used, at the cost of a few more amplifiers.

Finally we demonstrated a frequency reference setup based on the NICEOHMS technique on $^{13}C_2H_2$. We built two identical setups and showed a superior signal to noise ratio compared to saturated absorption spectroscopy. Beating the two setups against each other revealed a minimum (in)stability of 25 Hz at 0.2 s integration time. Using AOMs for frequency feedback significantly increases our feedback bandwidth and allows us to stabilize the laser at shorter timescales than possible with systems which employ lock-in amplifiers. This is promising performance compared to the commercially available Stabiλaser product, but we also show a large frequency drift which limits the performance. We suspect this drift to be related to the RAM issues presented, and possibly connected to the temperature stability of the breadboard. We believe the stability could be improved if these problems are solved, and long term averaging could be performed. Once this has been achieved, the next task will be to characterize the systematic errors and uncertainties of the setup arising from temperature, pressure, and magnetic field effects on the transition frequency. Once these sources of uncertainty have been investigated a full error budget can be presented. It would then be interesting to investigate the possibility of absolutely referencing the Kerr frequency comb, and the local oscillator used in the transmission experiment, to see if data transmission can be improved with more stable lasers. An issue for potential future work is that the carbon-13 isotope of acetylene is becoming increasingly scarce as it is no longer available as a commercial product. It should therefore be investigated if a similar transition in the carbon-12 acetylene isotope could be used instead, even though it would not be officially recognized as a recommended frequency reference.

List of Figures

34. Pasquazi et al., "Micro-Combs: A Novel Generation of Optical Sources"(2018)
35. Helgason et al., "Superchannel Engineering of Microcombs for Optical Communications"(2019)
50. Ye et al., "High-Q Si 3 N 4 Microresonators Based on a Subtractive Processing for Kerr Nonlinear Optics"(2019)
54. Kippenberg et al., "Dissipative Kerr Solitons in Optical Microresonators"(2018)

74. Riley et al., *Handbook of Frequency Stability Analysis* (2008)

97. Sasaki et al., "Single-Mode 37-Core Fiber with a Cladding Diameter of 248 Um"(2017)
98. BIPM, *BIPM Frequency References Overview*()

105. Silander, *Cavity Enhanced Optical Sensing*(2015)

List of Tables

References

[1] BIPM. "Le Système International d'unités (SI)". Ninth. Bureau international des poids et mesures, 2019.

[2] H. Schnatz, B. Lipphardt, J. Helmcke, F. Riehle, and G. Zinner. "Phase Coherent Frequency Measurement of Visible Radiation". In: *IEE Conference Publication* 418 (1996), p. 244. DOI: 10.1049/cp:19960055.

[3] Th Udem, S. A. Diddams, K. R. Vogel, C. W. Oates, E. A. Curtis, W. D. Lee, W. M. Itano, R. E. Drullinger, J. C. Bergquist, and L. Hollberg. "Absolute Frequency Measurements of the Hg+ and Ca Optical Clock Transitions with a Femtosecond Laser". In: *Physical Review Letters* 86.22 (2001), pp. 4996–4999. DOI: 10.1103/PhysRevLett.86.4996.

[4] M. T. Murphy, Th Udem, R. Holzwarth, A. Sizmann, L. Pasquini, C. Araujo-Hauck, H. Dekker, S. D'Odorico, M. Fischer, T. W. Hänsch, and A. Manescau. "High-Precision Wavelength Calibration of Astronomical Spectrographs with Laser Frequency Combs". In: *Monthly Notices of the Royal Astronomical Society* 380.2 (2007), pp. 839–847. DOI: 10.1111/j.1365-2966.2007.12147.x.

[5] T. Wilken, C. Lovis, A. Manescau, T. Steinmetz, L. Pasquini, G. Lo Curto, T. W. Hansch, R. Holzwarth, and Th Udem. "High-Precision Calibration of Spectrographs". In: *Monthly Notices of the Royal Astronomical Society: Letters* 405.1 (2010), pp. 16–20. DOI: 10.1111/j.1745-3933.2010.00850.x.

[6] C.-H. Li, D. F. Phillips, A. G. Glenday, A. J. Benedick, G. Chang, L.-J. Chen, C. Cramer, G. Furesz, F. X. Kärtner, D. Sasselov, A. Szentgyorgyi, and R. L. Walsworth. "Astro-Comb Calibration of an Echelle

Spectrograph". In: *Ground-based and Airborne Instrumentation for Astronomy III* 7735.July 2010 (2010), 77354O. DOI: 10.1117/12.857534.

[7] Gabriel G. Ycas, Franklyn Quinlan, Scott A. Diddams, Steve Osterman, Suvrath Mahadevan, Stephen Redman, Ryan Terrien, Lawrence Ramsey, Chad F. Bender, Brandon Botzer, and Steinn Sigurdsson. "Demonstration of On-Sky Calibration of Astronomical Spectra Using a 25 GHz near-IR Laser Frequency Comb". In: *Optics Express* 20.6 (2012), p. 6631. DOI: 10.1364/oe.20.006631.

[8] Alexander G. Glenday, Chih-Hao Li, Nicholas Langellier, Guoqing Chang, Li-Jin Chen, Gabor Furesz, Alexander A. Zibrov, Franz Kärtner, David F. Phillips, Dimitar Sasselov, Andrew Szentgyorgyi, and Ronald L. Walsworth. "Operation of a Broadband Visible-Wavelength Astro-Comb with a High-Resolution Astrophysical Spectrograph". In: *Optica* 2.3 (2015), p. 250. DOI: 10.1364/optica.2.000250.

[9] Richard A. McCracken, Éric Depagne, Rudolf B. Kuhn, Nicolas Erasmus, Lisa A. Crause, and Derryck T. Reid. "Wavelength Calibration of a High Resolution Spectrograph with a Partially Stabilized 15-GHz Astrocomb from 550 to 890 Nm". In: *Optics Express* 25.6 (2017), p. 6450. DOI: 10.1364/oe.25.006450.

[10] S. Schiller. "Spectrometry with Frequency Combs". In: *Optics Letters* 27.9 (2002), p. 766. DOI: 10.1364/ol.27.000766.

[11] Fritz Keilmann, Christoph Gohle, and Ronald Holzwarth. "Time-Domain Mid-Infrared Frequency-Comb Spectrometer". In: *Optics Letters* 29.13 (2004), p. 1542. DOI: 10.1364/ol.29.001542.

[12] Ian Coddington, Nathan Newbury, and William Swann. "Dual-Comb Spectroscopy". In: *Optica* 3.4 (Apr. 2016), p. 414. DOI: 10.1364/OPTICA.3.000414.

[13] Kaoru Minoshima and Hirokazu Matsumoto. "High-Accuracy Measurement of 240-m Distance in an Optical Tunnel by Use of a Compact Femtosecond Laser". In: *Applied Optics* 39.30 (2000), p. 5512. DOI: 10.1364/ao.39.005512.

[14] Joohyung Lee, Young Jin Kim, Keunwoo Lee, Sanghyun Lee, and Seung Woo Kim. "Time-of-Flight Measurement with Femtosecond Light Pulses". In: *Nature Photonics* 4.10 (2010), pp. 716–720. DOI: 10.1038/nphoton.2010.175.

[15] Johann Riemensberger, Anton Lukashchuk, Maxim Karpov, Wenle Weng, Erwan Lucas, Junqiu Liu, and Tobias J. Kippenberg. "Massively Parallel Coherent Laser Ranging Using a Soliton Microcomb". In: *Nature* 581.7807 (2020), pp. 164–170. DOI: 10.1038/s41586-020-2239-3.

[16] T. M. Fortier, M. S. Kirchner, F. Quinlan, J. Taylor, J. C. Bergquist, T. Rosenband, N. Lemke, A. Ludlow, Y. Jiang, C. W. Oates, and S. A. Diddams. "Generation of Ultrastable Microwaves via Optical Frequency Division". In: *Nature Photonics* 5.7 (2011), pp. 425–429. DOI: 10.1038/nphoton.2011.121.

[17] Georg Rademacher, Benjamin J. Puttnam, Ruben S. Luís, Jun Sakaguchi, Werner Klaus, Tobias A. Eriksson, Yoshinari Awaji, Tetsuya Hayashi, Takuji Nagashima, Tetsuya Nakanishi, Toshiki Taru, Taketoshi Takahata, Tetsuya Kobayashi, Hideaki Furukawa, and Naoya Wada. "10.66 Peta-Bit/s Transmission over a 38-Core-Three-Mode Fiber". In: *Optical Fiber Communication Conference (OFC) 2020*. Washington, D.C.: OSA, 2020, Th3H.1. DOI: 10.1364/OFC.2020.Th3H.1.

[18] Pablo Marin-Palomo, Juned N. Kemal, Maxim Karpov, Arne Kordts, Joerg Pfeifle, Martin H.P. Pfeiffer, Philipp Trocha, Stefan Wolf, Victor Brasch, Miles H. Anderson, Ralf Rosenberger, Kovendhan Vijayan, Wolfgang Freude, Tobias J. Kippenberg, and Christian Koos. "Microresonator-Based Solitons for Massively Parallel Coherent Optical Communications". In: *Nature* 546.7657 (2017), pp. 274–279. DOI: 10.1038/nature22387.

[19] Hao Hu, Francesco Da Ros, Minhao Pu, Feihong Ye, Kasper Ingerslev, Edson Porto da Silva, Md Nooruzzaman, Yoshimichi Amma, Yusuke Sasaki, Takayuki Mizuno, Yutaka Miyamoto, Luisa Ottaviano, Elizaveta Semenova, Pengyu Guan, Darko Zibar, Michael Galili, Kresten Yvind, Toshio Morioka, and Leif K. Oxenløwe. "Single-Source Chip-Based Frequency Comb Enabling Extreme Parallel Data Transmission". In: *Nature Photonics* 12.8 (Aug. 2018), pp. 469–473. DOI: 10.1038/s41566-018-0205-5.

[20] Mikael Mazur, Jochen Schroder, Magnus Karlsson, and Peter A. Andrekson. "Joint Superchannel Digital Signal Processing for Effective Inter-Channel Interference Cancellation". In: *Journal of Lightwave Technology* 38.20 (2020), pp. 5676–5684. DOI: 10.1109/jlt.2020.3001716.

[21] S H Cho, Y Chen, H A Haus, J G Fujimoto, E P Ippen, U Morgner, F X Kärtner, V Scheuer, G Angelow, and T Tschudi. "Sub-Two-Cycle Pulses from a Kerr-lens Mode-Locked Ti : Sapphire Laser". In: *Optics Letters* 24.6 (1999), pp. 411–413.

[22] D. H. Sutter, G. Steinmeyer, L. Gallmann, N. Matuschek, F. Morier-Genoud, U. Keller, V. Scheuer, G. Angelow, and T. Tschudi. "Semiconductor Saturable-Absorber Mirror–Assisted Kerr-lens Mode-Locked Ti:Sapphire Laser Producing Pulses in the Two-Cycle Regime". In: *Optics Letters* 24.9 (1999), p. 631. DOI: 10.1364/ol.24.000631.

[23] H. R. Telle, G. Steinmeyer, A. E. Dunlop, J. Stenger, D. H. Sutter, and U. Keller. "Carrier-Envelope Offset Phase Control: A Novel Concept for Absolute Optical Frequency Measurement and Ultrashort Pulse Generation". In: *Applied Physics B: Lasers and Optics* 69.4 (1999), pp. 327–332. DOI: 10.1007/s003400050813.

[24] Jinendra K. Ranka, Robert S. Windeler, and Andrew J. Stentz. "Visible Continuum Generation in Air–Silica Microstructure Optical Fibers with Anomalous Dispersion at 800 Nm". In: *Optics Letters* 25.1 (2000), p. 25. DOI: 10.1364/ol.25.000025.

[25] T. A. Birks, W. J. Wadsworth, and P. St J. Russell. "Supercontinuum Generation in Tapered Fibers". In: *Optics Letters* 25.19 (Oct. 2000), p. 1415. DOI: 10.1364/OL.25.001415.

[26] T. M. Fortier, A. Bartels, and S. A. Diddams. "Octave-Spanning Ti:Sapphire Laser with a Repetition Rate >1 GHz for Optical Frequency Measurements and Comparisons". In: *Optics Letters* 31.7 (2006), p. 1011. DOI: 10.1364/ol.31.001011.

[27] P. Del'Haye, A. Schliesser, O. Arcizet, T. Wilken, R. Holzwarth, and T. J. Kippenberg. "Optical Frequency Comb Generation from a Monolithic Microresonator". In: *Nature* 450.7173 (2007), pp. 1214–1217. DOI: 10.1038/nature06401.

[28] Holly Leopardi, Josue Davila-Rodriguez, Franklyn Quinlan, Judith Olson, Jeff A. Sherman, Scott A. Diddams, and Tara M. Fortier. "Single-Branch Er:Fiber Frequency Comb for Precision Optical Metrology with 10-18 Fractional Instability". In: *Optica* 4.8 (2017), p. 879. DOI: 10.1364/optica.4.000879.

[29] Katja Beha, Daniel Cole, Pascal Del'Haye, Aurélien Coillet, Scott Diddams, and Scott Papp. "Electronic Synthesis of Light". In: *Optica* 4.4 (2017), p. 406. DOI: 10.1364/OPTICA.4.000406.s001.

[30] D. K. Armani, T. J. Kippenberg, S. M. Spillane, and K. J. Vahala. "Ultra-High-Q Toroid Microcavity on a Chip". In: *Nature* 421.6926 (2003), pp. 925–928. DOI: 10.1038/nature01371.

[31] Jacob S. Levy, Alexander Gondarenko, Mark A. Foster, Amy C. Turner-Foster, Alexander L. Gaeta, and Michal Lipson. "CMOS-compatible Multiple-Wavelength Oscillator for on-Chip Optical Interconnects". In: *Nature Photonics* 4.1 (2010), pp. 37–40. DOI: 10.1038/nphoton.2009.259.

[32] L. Razzari, D. Duchesne, M. Ferrera, R. Morandotti, S. Chu, B. E. Little, and D. J. Moss. "CMOS-compatible Integrated Optical Hyper-Parametric Oscillator". In: *Nature Photonics* 4.1 (2010), pp. 41–45. DOI: 10.1038/nphoton.2009.236.

[33] Matthew W. Puckett, Kaikai Liu, Nitesh Chauhan, Qiancheng Zhao, Naijun Jin, Haotian Cheng, Jianfeng Wu, Ryan O. Behunin, Peter T. Rakich, Karl D. Nelson, and Daniel J. Blumenthal. "422 Million Intrinsic Quality Factor Planar Integrated All-Waveguide Resonator with Sub-MHz Linewidth". In: *Nature Communications* 12.1 (2021), pp. 1–8. DOI: 10.1038/s41467-021-21205-4.

[34] Alessia Pasquazi, Marco Peccianti, Luca Razzari, David J. Moss, Stéphane Coen, Miro Erkintalo, Yanne K. Chembo, Tobias Hansson, Stefan Wabnitz, Pascal Del'Haye, Xiaoxiao Xue, Andrew M. Weiner, and Roberto Morandotti. "Micro-Combs: A Novel Generation of Optical Sources". In: *Physics Reports* 729 (2018), pp. 1–81. DOI: 10.1016/j.physrep.2017.08.004.

[35] Óskar B. Helgason, Attila Fülöp, Jochen Schröder, Peter A. Andrekson, Andrew M. Weiner, and Victor Torres-Company. "Superchannel Engineering of Microcombs for Optical Communications". In: *Journal of the Optical Society of America B* 36.8 (2019), p. 2013. DOI: 10.1364/josab.36.002013.

[36] A. B. Matsko, A. A. Savchenkov, and L. Maleki. "Normal Group-Velocity Dispersion Kerr Frequency Comb". In: *Optics Letters* 37.1 (2012), p. 43. DOI: 10.1364/ol.37.000043.

[37] Wei Liang, Anatoliy A. Savchenkov, Vladimir S. Ilchenko, Danny Eliyahu, David Seidel, Andrey B. Matsko, and Lute Maleki. "Generation of a Coherent Near-Infrared Kerr Frequency Comb in a Monolithic Microresonator with Normal GVD". In: *Optics Letters* 39.10 (2014), p. 2920. DOI: 10.1364/ol.39.002920.

[38] Yang Liu, Yi Xuan, Xiaoxiao Xue, Pei-Hsun Wang, Andrew J. Metcalf, Steve Chen, Minghao Qi, and Andrew M. Weiner. "Investigation of Mode Interaction in Optical Microresonators for Kerr Frequency Comb Generation". In: *CLEO: 2014*. Vol. 1. Washington, D.C.: OSA, 2014, FW1D.2. DOI: 10.1364/CLEO_QELS.2014.FW1D.2.

[39] Pedro Parra-Rivas, Damià Gomila, Edgar Knobloch, Stéphane Coen, and Lendert Gelens. "Origin and Stability of Dark Pulse Kerr Combs in Normal Dispersion Resonators". In: *Optics Letters* 41.11 (June 2016), p. 2402. DOI: 10.1364/OL.41.002402.

[40] Elham Nazemosadat, Attila Fülöp, Óskar B. Helgason, Pei Hsun Wang, Yi Xuan, Dan E. Leaird, Minghao Qi, Enrique Silvestre, Andrew M. Weiner, and Victor Torres-Company. "Switching Dynamics of Dark-Pulse Kerr Frequency Comb States in Optical Microresonators". In: *Physical Review A* 103.1 (2021), pp. 1–9. DOI: 10.1103/PhysRevA.103.013513.

[41] Óskar B. Helgason, Francisco R. Arteaga-Sierra, Zhichao Ye, Krishna Twayana, Peter A. Andrekson, Magnus Karlsson, Jochen Schröder, and Victor Torres-Company. "Dissipative Solitons in Photonic Molecules". In: *Nature Photonics* 15.April (2021). DOI: 10.1038/s41566-020-00757-9.

[42] T. Herr, V. Brasch, J. D. Jost, C. Y. Wang, N. M. Kondratiev, M. L. Gorodetsky, and T. J. Kippenberg. "Temporal Solitons in Optical Microresonators". In: *Nature Photonics* 8.2 (2014), pp. 145–152. DOI: 10.1038/nphoton.2013.343.

[43] Xu Yi, Qi-Fan Yang, Ki Youl Yang, and Kerry Vahala. "Active Capture and Stabilization of Temporal Solitons in Microresonators". In: *Optics Letters* 41.9 (2016), p. 2037. DOI: 10.1364/ol.41.002037.

[44] H. Guo, M. Karpov, E. Lucas, A. Kordts, M. H.P. Pfeiffer, V. Brasch, G. Lihachev, V. E. Lobanov, M. L. Gorodetsky, and T. J. Kippenberg. "Universal Dynamics and Deterministic Switching of Dissipative Kerr Solitons in Optical Microresonators". In: *Nature Physics* 13.1 (2017), pp. 94–102. DOI: 10.1038/nphys3893.

[45] Boqiang Shen, Lin Chang, Junqiu Liu, Heming Wang, Qi Fan Yang, Chao Xiang, Rui Ning Wang, Jijun He, Tianyi Liu, Weiqiang Xie, Joel Guo, David Kinghorn, Lue Wu, Qing Xin Ji, Tobias J. Kippenberg, Kerry Vahala, and John E. Bowers. "Integrated Turnkey Soliton Microcombs". In: *Nature* 582.7812 (2020), pp. 365–369. DOI: 10.1038/s41586-020-2358-x.

[46] Shuai Wan, Rui Niu, Zheng-Yu Wang, Jin-Lan Peng, Ming Li, Jin Li, Guang-Can Guo, Chang-Ling Zou, and Chun-Hua Dong. "Frequency Stabilization and Tuning of Breathing Soliton in SiN Microresonators". In: (2020), pp. 1–7.

[47] R. Soref and J. Larenzo. "All-Silicon Active and Passive Guided-Wave Components for Lambda = 1.3 and 1.6 Um". In: *IEEE Journal of Quantum Electronics* 22.6 (June 1986), pp. 873–879. DOI: 10.1109/JQE.1986.1073057.

[48] David Thomson, Aaron Zilkie, John E. Bowers, Tin Komljenovic, Graham T. Reed, Laurent Vivien, Delphine Marris-Morini, Eric Cassan, Léopold Virot, Jean-Marc Fédéli, Jean-Michel Hartmann, Jens H. Schmid, Dan-Xia Xu, Frédéric Boeuf, Peter O'Brien, Goran Z. Mashanovich, and M. Nedeljkovic. "Roadmap on Silicon Photonics". In: *Journal of Optics* 18.7 (July 2016), p. 073003. DOI: 10.1088/2040-8978/18/7/073003.

[49] Junqiu Liu, Guanhao Huang, Rui Ning Wang, Jijun He, Arslan S. Raja, Tianyi Liu, Nils J. Engelsen, and Tobias J Kippenberg. "High-Yield, Wafer-Scale Fabrication of Ultralow-Loss, Dispersion-Engineered Silicon Nitride Photonic Circuits". In: *Nature Communications* 12.1 (Dec. 2021), p. 2236. DOI: 10.1038/s41467-021-21973-z.

[50] Zhichao Ye, Krishna Twayana, Peter A. Andrekson, and Victor Torres-Company. "High-Q Si 3 N 4 Microresonators Based on a Subtractive Processing for Kerr Nonlinear Optics". In: *Optics Express* 27.24 (Nov. 2019), p. 35719. DOI: 10.1364/OE.27.035719.

[51] Amir Arbabi and Lynford L Goddard. "Measurements of the Refractive Indices and Thermo-Optic Coefficients of Si_3N_4 and SiO_x Using Microring Resonances." In: *Optics letters* 38.19 (2013), pp. 3878–3881.

[52] Robert W. Boyd. "Nonlinear Optics - Third Edition". Ed. by Robert W. Boyd. Academic Press, 2008.

[53] Govind P. Agrawal. "Nonlinear Fiber Optics". Ed. by Govind P. Agrawal, Ivan P Kaminow, and Paul L Kelley. Academic Press, 2001.

[54] Tobias J. Kippenberg, Alexander L. Gaeta, Michal Lipson, and Michael L. Gorodetsky. "Dissipative Kerr Solitons in Optical Microresonators". In: *Science* 361.6402 (Aug. 2018), eaan8083. DOI: 10.1126/science.aan8083.

[55] Kensuke Ikeda. "Multiple-Valued Stationary State and Its Instability of the Transmitted Light by a Ring Cavity System". In: *Optics Communications* 30.2 (1979), pp. 257–261. DOI: 10.1016/0030-4018(79)90090-7.

[56] L A Lugiato, F Prati, M L Gorodetsky, and T. J. Kippenberg. "From the Lugiato–Lefever Equation to Microresonator-Based Soliton Kerr Frequency Combs". In: *Philosophical Transactions of the Royal Society A: Mathematical, Physical and Engineering Sciences* 376.2135 (Dec. 2018), p. 20180113. DOI: 10.1098/rsta.2018.0113.

[57] Paul E. Barclay, Kartik Srinivasan, and Oskar Painter. "Nonlinear Response of Silicon Photonic Crystal Micresonators Excited via an Integrated Waveguide and Fiber Taper". In: *Optics Express* 13.3 (2005), p. 801. DOI: 10.1364/OPEX.13.000801.

[58] Su-peng Yu, Travis C Briles, Gregory T Moille, Xiyuan Lu, Scott A Diddams, Kartik Srinivasan, and Scott B Papp. "Tuning Kerr-Soliton Frequency Combs to Atomic Resonances". In: *Physical Review Applied* 11.4 (Apr. 2019), p. 044017. DOI: 10.1103/PhysRevApplied.11.044017.

[59] Caroline Munk Nielsen. "Behaviour of Picosecond and Femtosecond Pulses in SiO 2 / Si 3 N 4 Microring Resonator Filters". PhD thesis. UCPH, 2020.

[60] Yi Zheng, Minhao Pu, Ailun Yi, Ayman N. Kamel, Martin. R. Henriksen, Asbjørn A. Jørgensen, Xin Ou, and Haiyan Ou. "Fabrication of High-Q, High-Confinement 4H-SiC Microring Resonators by Surface Roughness Reduction". In: *Conference on Lasers and Electro-Optics*. Vol. Part F129-. Washington, D.C.: OSA, 2019, SM2O.7. DOI: 10.1364/CLEO_SI.2019.SM2O.7.

[61] A. A. Savchenkov, A. B. Matsko, W. Liang, V. S. Ilchenko, D. Seidel, and L. Maleki. "Kerr Frequency Comb Generation in Overmoded Resonators". In: *Optics Express* 20.24 (2012), p. 27290. DOI: 10.1364/oe.20.027290.

[62] Xiaoxiao Xue, Yi Xuan, Yang Liu, Pei Hsun Wang, Steven Chen, Jian Wang, Dan E. Leaird, Minghao Qi, and Andrew M. Weiner. "Mode-Locked Dark Pulse Kerr Combs in Normal-Dispersion Microresonators". In: *Nature Photonics* 9.9 (2015), pp. 594–600. DOI: 10.1038/nphoton.2015.137.

[63] Su-Peng Yu, Erwan Lucas, Jizhao Zang, and Scott B. Papp. "A Continuum of Bright and Dark-Pulse States in a Photonic-Crystal Resonator". In: *Nature Communications* 13.1 (Dec. 2022), p. 3134. DOI: 10.1038/s41467-022-30774-x.

[64] Gregory Moille, Qing Li, Xiyuan Lu, and Kartik Srinivasan. "Pylle: A Fast and User Friendly Lugiato-Lefever Equation Solver". In: *Journal of Research of the National Institute of Standards and Technology* 124.124012 (2019). DOI: 10.6028/jres.124.012.

[65] Zhichao Ye. "Ultralow-Loss Silicon Nitride Waveguides for Nonlinear Optics". PhD thesis. Sweden: Chalmers University of Technology, 2021.

[66] Stéphane Coen and Miro Erkintalo. "Universal Scaling Laws of Kerr Frequency Combs". In: *Optics Letters* 38.11 (2013), p. 1790. DOI: 10.1364/ol.38.001790.

[67] T. Herr, V. Brasch, J. D. Jost, I. Mirgorodskiy, G. Lihachev, M. L. Gorodetsky, and T. J. Kippenberg. "Mode Spectrum and Temporal Soliton Formation in Optical Microresonators". In: *Physical Review Letters* 113.12 (2014), pp. 1–6. DOI: 10.1103/PhysRevLett.113.123901.

[68] Xu Yi, Qi-Fan Yang, Ki Youl Yang, Myoung-Gyun Suh, and Kerry Vahala. "Soliton Frequency Comb at Microwave Rates in a High-Q Silica Microresonator". In: *Optica* 2.12 (2015), p. 1078. DOI: 10.1364/optica.2.001078.

[69] Chaitanya Joshi, Jae K. Jang, Kevin Luke, Xingchen Ji, Steven A. Miller, Alexander Klenner, Yoshitomo Okawachi, Michal Lipson, and Alexander L. Gaeta. "Thermally Controlled Comb Generation and Soliton Modelocking in Microresonators". In: *Optics Letters* 41.11 (2016), p. 2565. DOI: 10.1364/ol.41.002565.

[70] Óskar Bjarki Helgason. "Dissipative Kerr Solitons in Normal Dispersion Microresonators". PhD thesis. Sweden: Chalmers University of Technology, 2020.

[71] IdPhotonics. "Mainframe Series CoBriteMX Lasers Accessed on 2021/04".

[72] Leonhard Neuhaus, Samuel Deléglise, Jonas Neergard-Nielsen, Xueshi Guo, Jerome Degallaix, Pierre Clade, Matthew Winchester, Remi Metzdorff, Kevin Makles, and Clement Chardin. "PyRPL". 2016.

[73] Pendulum. "CNT-90 Datasheet Accessed on 2021/04".

[74] W J Riley and David A Howe. "Handbook of Frequency Stability Analysis". 1. Feb. 2008.

[75] David W. Allan. "Should the Classical Variance Be Used as a Basic Measure in Standards Metrology?" In: *IEEE Transactions on Instrumentation and Measurement* IM-36.2 (June 1987), pp. 646–654. DOI: 10.1109/TIM.1987.6312761.

[76] NKT. "Koheras Basik Accessed on 2021/08". In: 13490308 (2014), pp. 1–4.

[77] N K T Photonics. "Analysis of Laser Frequency Stability Using Beat-Note Measurement". In: (2013), pp. 1–5.

[78] Cisco Annual and Internet Report. *White Paper Cisco Public*. Tech. rep. 2018.

[79] "SamsungSmartFridge". https://www.samsung.com/us/explore/family-hub-refrigerator/overview/.

[80] "Amazon.Com: Brita Medium 8 Cup Infinity Smart Water Pitcher and Filter - BPA Free - Black: Kitchen and Dining". https://www.amazon.com/Brita-Medium-Infinity-Pitcher-Filter/dp/B018GGK38S/ref=cm_cr_arp_d_bdcrb_top?ie=UTF8.

[81] "Roost Smart Sensors — Roost Home Telematics". https://getroost.com/sensors/.

[82] "LavvieBot S". https://www.lavviebot.com/en/home.html.

[83] Nicola Jones. "How to Stop Data Centres from Gobbling up the World's Electricity". In: *Nature* 561.7722 (2018), pp. 163–166. DOI: 10.1038/d41586-018-06610-y.

[84] Masaki Terayama, Seiji Okamoto, Keisuke Kasai, Masato Yoshida, and Masataka Nakazawa. "4096 QAM (72 Gbit/s) Single-Carrier Coherent Optical Transmission with a Potential SE of 15.8 Bit/s/Hz in All-Raman Amplified 160 Km Fiber Link". In: *2018 Optical Fiber Communications Conference and Exposition, OFC 2018 - Proceedings* (2018), pp. 1–3.

[85] Mengyue Xu, Mingbo He, Hongguang Zhang, Jian Jian, Ying Pan, Xiaoyue Liu, Lifeng Chen, Xiangyu Meng, Hui Chen, Zhaohui Li, Xi Xiao, Shaohua Yu, Siyuan Yu, and Xinlun Cai. "High-Performance Coherent Optical Modulators Based on Thin-Film Lithium Niobate Platform". In: *Nature Communications* 11.1 (2020), pp. 1–7. DOI: 10.1038/s41467-020-17806-0.

[86] Hiroshi Yamazaki, Munehiko Nagatani, Hitoshi Wakita, Yoshihiro Ogiso, Masanori Nakamura, Minoru Ida, Hideyuki Nosaka, Toshikazu Hashimoto, and Yutaka Miyamoto. “IMDD Transmission at Net Data Rate of 333 Gb/s Using over-100-GHz-bandwidth Analog Multiplexer and Mach-zehnder Modulator”. In: *Journal of Lightwave Technology* 37.8 (2019), pp. 1772–1778. DOI: 10.1109/JLT.2019.2898675.

[87] Munehiko Nagatani, Hitoshi Wakita, Hiroshi Yamazaki, Yoshihiro Ogiso, Miwa Mutoh, Minoru Ida, Fukutaro Hamaoka, Masanori Nakamura, Takayuki Kobayashi, Yutaka Miyamoto, and Hideyuki Nosaka. “A Beyond-1-Tb/s Coherent Optical Transmitter Front-End Based on 110-GHz-Bandwidth 2:1 Analog Multiplexer in 250-Nm InP DHBT”. In: *IEEE Journal of Solid-State Circuits* 55.9 (2020), pp. 2301–2315. DOI: 10.1109/JSSC.2020.2989579.

[88] Christian Schmidt, Hiroshi Yamazaki, Gregory Raybon, Peter Schvan, Erwan Pincemin, S. J.Ben Yoo, Daniel J. Blumenthal, Takayuki Mizuno, and Robert Elschner. “Data Converter Interleaving: Current Trends and Future Perspectives”. In: *IEEE Communications Magazine* 58.5 (2020), pp. 19–25. DOI: 10.1109/MCOM.001.1900683.

[89] B J Puttnam, R. S. Luis, W Klaus, J Sakaguchi, J.-M. Delgado Mendinueta, Y Awaji, N. Wada, Yoshiaki Tamura, Tetsuya Hayashi, Masaaki Hirano, and J. Marciante. “2.15 Pb/s Transmission Using a 22 Core Homogeneous Single-Mode Multi-Core Fiber and Wideband Optical Comb”. In: *2015 European Conference on Optical Communication (ECOC)*. 1. IEEE, Sept. 2015, pp. 1–3. DOI: 10.1109/ECOC.2015.7341685.

[90] Joerg Pfeifle, Victor Brasch, Matthias Lauermann, Yimin Yu, Daniel Wegner, Tobias Herr, Klaus Hartinger, Philipp Schindler, Jingshi Li, David Hillerkuss, Rene Schmogrow, Claudius Weimann, Ronald Holzwarth, Wolfgang Freude, Juerg Leuthold, Tobias J Kippenberg, and Christian Koos. “Coherent Terabit Communications with Microresonator Kerr Frequency Combs”. In: *Nature Photonics* 8.5 (May 2014), pp. 375–380. DOI: 10.1038/nphoton.2014.57.

[91] Attila Fülöp, Mikael Mazur, Abel Lorences-Riesgo, Óskar B. Helgason, Pei Hsun Wang, Yi Xuan, Dan E. Leaird, Minghao Qi, Peter A. Andrekson, Andrew M. Weiner, and Victor Torres-Company. “High-Order Coherent Communications Using Mode-Locked Dark-Pulse Kerr Combs from Microresonators”. In: *Nature Communications* 9.1 (2018), pp. 1–8. DOI: 10.1038/s41467-018-04046-6.

[92] Bill Corcoran, Mengxi Tan, Xingyuan Xu, Andreas Boes, Jiayang Wu, Thach G Nguyen, Sai T Chu, Brent E Little, Roberto Morandotti, Arnan Mitchell, and David J Moss. “Ultra-Dense Optical Data Transmission over Standard Fibre with a Single Chip Source”. In: *Nature Communications* 11.1 (Dec. 2020), p. 2568. DOI: 10.1038/s41467-020-16265-x.

[93] Claude E. Shannon. “Cominunication Theory in the Presence of Noise”. In: *Proceedings of the IRE* 37.1 (1949), pp. 10–21. DOI: 10.1109/JRPROC.1949.232969.

[94] Changjing Bao, Lin Zhang, Andrey Matsko, Yan Yan, Zhe Zhao, Guodong Xie, Anuradha M. Agarwal, Lionel C. Kimerling, Jurgen Michel, Lute Maleki, and Alan E. Willner. “Nonlinear Conversion Efficiency in Kerr Frequency Comb Generation”. In: *Optics Letters* 39.21 (Nov. 2014), p. 6126. DOI: 10.1364/OL.39.006126.

[95] Peter J. Winzer. “Chapter 8 - Transmission System Capacity Scaling through Space-Division Multiplexing: A Techno-Economic Perspective”. In: *Optical Fiber Telecommunications VII*. Ed. by Alan Willner. Academic Press, 2019, pp. 337–369. DOI: 10.1016/B978-0-12-816502-7.00009-9.

[96] Edson P. da Silva, Frederik Klejs, Mads Lillieholm, Shajeel Iqbal, Metodi P. Yankov, Julio C. M. Diniz, Toshio Morioka, Leif K. Oxenlowe, and Michael Galili. “Experimental Characterization of 10x8 GBd DP-1024QAM Transmission with 8-Bit DACs and Intradyne Detection”. In: *2018 European Conference on Optical Communication (ECOC)*. 1. IEEE, Sept. 2018, pp. 1–3. DOI: 10.1109/ECOC.2018.8535205.

[97] Y. Sasaki, K. Takenaga, K. Aikawa, Y. Miyamoto, and T. Morioka. “Single-Mode 37-Core Fiber with a Cladding Diameter of 248 Um”. In: *Optical Fiber Communication Conference*. Washington, D.C.: OSA, 2017, Th1H.2. DOI: 10.1364/OFC.2017.Th1H.2.

[98] BIPM. “BIPM Frequency References Overview”. https://www.bipm.org/en/publications/mises-en-pratique/standard-frequencies-info.

[99] Fritz Riehle. “Frequency Standards”. Weinheim, FRG: Wiley, Sept. 2003. DOI: 10.1002/3527605991.

[100] BIPM. “Recommende Values of Standard Frequencies for Applications Including the Practical Realization of the Metre and Secondary Representation of the Second - Acetylene (1.54 Um)”. 2007/ Oktober.

[101] R. W. P. Drever, J. L. Hall, F. V. Kowalski, J. Hough, G. M. Ford, A. J. Munley, and H. Ward. “Laser Phase and Frequency Stabilization Using an Optical Resonator”. In: *Applied Physics B Photophysics and Laser Chemistry* 31.2 (June 1983), pp. 97–105. DOI: 10.1007/BF00702605.

[102] Daniel Adam Steck. “Quantum and Atom Optics Textbook”. http://steck.us/academic.html%5Cnhttp 2007. DOI: 10.1007/978-3-540-28574-8.

[103] Gary C. Bjorklund. “Frequency-Modulation Spectroscopy: A New Method for Measuring Weak Absorptions and Dispersions”. In: *Optics Letters* 5.1 (Jan. 1980), p. 15. DOI: 10.1364/OL.5.000015.

[104] Long-Sheng Ma, Jun Ye, Pierre Dubé, and John L. Hall. “Ultrasensitive Frequency-Modulation Spectroscopy Enhanced by a High-Finesse Optical Cavity: Theory and Application to Overtone Transitions of C_2H_2 and C_2HD”. In: *Journal of the Optical Society of America B* 16.12 (Dec. 1999), p. 2255. DOI: 10.1364/JOSAB.16.002255.

[105] Isak Silander. “Cavity Enhanced Optical Sensing”. 2015.

[106] Edward A. Whittaker, Manfred Gehrtz, and Gary C. Bjorklund. “Residual Amplitude Modulation in Laser Electro-Optic Phase Modulation”. In: *Journal of the Optical Society of America B* 2.8 (Aug. 1985), p. 1320. DOI: 10.1364/JOSAB.2.001320.

[107] Aleksandra Foltynowicz, Isak Silander, and Ove Axner. "Reduction of Background Signals in Fiber-Based NICE-OHMS". In: *Journal of the Optical Society of America B* 28.11 (Nov. 2011), p. 2797. DOI: 10.1364/JOSAB.28.002797.

[108] N. C. Wong and J. L. Hall. "Servo Control of Amplitude Modulation in Frequency-Modulation Spectroscopy: Demonstration of Shot-Noise-Limited Detection". In: *Journal of the Optical Society of America B* 2.9 (Sept. 1985), p. 1527. DOI: 10.1364/JOSAB.2.001527.

[109] Patrick Ehlers, Alexandra C. Johansson, Isak Silander, Aleksandra Foltynowicz, and Ove Axner. "Use of Etalon-Immune Distances to Reduce the Influence of Background Signals in Frequency-Modulation Spectroscopy and Noise-Immune Cavity-Enhanced Optical Heterodyne Molecular Spectroscopy". In: *Journal of the Optical Society of America B* 31.12 (2014), p. 2938. DOI: 10.1364/josab.31.002938.

[110] DFM. "Stabilaser Accessed on 2022/01". https://stabilaser.dk/wp-content/uploads/2021/02/Datashe 1542e_UK_2021-01-28.pdf.

[111] Thomas Talvard, Philip G. Westergaard, Michael V. DePalatis, Nicolai F. Mortensen, Michael Drewsen, Bjarke Gøth, and Jan Hald. "Enhancement of the Performance of a Fiber-Based Frequency Comb by Referencing to an Acetylene-Stabilized Fiber Laser". In: *Optics Express* 25.3 (Feb. 2017), p. 2259. DOI: 10.1364/OE.25.002259.

[112] Gang Zhao, Thomas Hausmaninger, Florian M. Schmidt, Weiguang Ma, and Ove Axner. "High-Resolution Trace Gas Detection by Sub-Doppler Noise-Immune Cavity-Enhanced Optical Heterodyne Molecular Spectrometry: Application to Detection of Acetylene in Human Breath". In: *Optics Express* 27.13 (2019), p. 17940. DOI: 10.1364/oe.27.017940.

[113] Roy Zektzer, Matthew T. Hummon, Liron Stern, Yoel Sebbag, Yefim Barash, Noa Mazurski, John Kitching, and Uriel Levy. "A Chip-Scale Optical Frequency Reference for the Telecommunication Band Based on Acetylene". In: *Laser & Photonics Reviews* 14.6 (June 2020), p. 1900414. DOI: 10.1002/lpor.201900414.